AD-A047 322   NAVAL POSTGRADUATE SCHOOL MONTEREY CALIF   F/G 4/2
A NUMERICAL STUDY OF BAROTROPIC INSTABILITY OF A ZONALLY VARYIN--ETC(U)
JUN 77 J B TUPAZ

UNCLASSIFIED   NL

1 OF 2

ADA047 322

NAVAL POSTGRADUATE SCHOOL
Monterey, California

THESIS

A Numerical Study of Barotropic
Instability of a Zonally
Varying Easterly Jet

by

Jesus Bonifacio Tupaz

June 1977

Thesis Advisors: C-P Chang
                              R. T. Williams

Approved for public release; distribution unlimited.

REPORT DOCUMENTATION PAGE		READ INSTRUCTIONS BEFORE COMPLETING FORM
1. REPORT NUMBER	2. GOVT ACCESSION NO.	3. RECIPIENT'S CATALOG NUMBER
4. TITLE (and Subtitle) A Numerical Study of Barotropic Instability of a Zonally Varying Easterly Jet		5. TYPE OF REPORT & PERIOD COVERED Ph.D's Thesis June 1977
		6. PERFORMING ORG. REPORT NUMBER
7. AUTHOR(s) Jesus Bonifacio Tupaz		8. CONTRACT OR GRANT NUMBER(s)
9. PERFORMING ORGANIZATION NAME AND ADDRESS Naval Postgraduate School Monterey, CA 93940		10. PROGRAM ELEMENT, PROJECT, TASK AREA & WORK UNIT NUMBERS
11. CONTROLLING OFFICE NAME AND ADDRESS Naval Postgraduate School Monterey, CA 93940		12. REPORT DATE June 1977
		13. NUMBER OF PAGES 107
14. MONITORING AGENCY NAME & ADDRESS(if different from Controlling Office) Naval Postgraduate School Monterey, CA 93940		15. SECURITY CLASS. (of this report) UNCLASSIFIED
		15a. DECLASSIFICATION/DOWNGRADING SCHEDULE

16. DISTRIBUTION STATEMENT (of this Report)

Approved for public release; distribution unlimited.

17. DISTRIBUTION STATEMENT (of the abstract entered in Block 20, if different from Report)

19. KEY WORDS (Continue on reverse side if necessary and identify by block number)

barotropic instability
tropical easterly jet
monsoon
spatially-varying mean flow

20. ABSTRACT (Continue on reverse side if necessary and identify by block number)

The structure and behavior of barotropically unstable and stable wave disturbances in the vicinity of a zonally varying easterly jet are studied numerically with a linearized barotropic vorticity equation on a β-plane. The easterly jet is approximated by a Bickley jet with a slow zonal variation. The numerical results are also compared with a simple mechanistic analytical

DD FORM 1473 EDITION OF 1 NOV 65 IS OBSOLETE
1 JAN 73
(Page 1)   S/N 0102-014-6601 |

20. Abstract (continued)

model using the local phase speed and growth rate concepts. The results are grossly similar in several respects to that expected from the parallel flow theory of barotropic instability, however, the resultant structure of the waves causes a spatial growth rate greater than predicted by the local growth rates computed with a parallel flow model. In the stable region, the structure leads to strong dynamic damping. When a uniform advective velocity is added to a variable mean flow, the differences between the behavior of the computed waves and that implied by the parallel flow theory are somewhat reduced. The waves remove kinetic energy from the mean flow and most of this energy is removed on the downwind side of the jet. The computed structure and behavior of the waves have a number of features that resemble those observed in the vicinity of the upper troposphere easterly jet during the summer monsoon.

A Numerical Study of Barotropic Instability
of a Zonally Varying Easterly Jet

by

Jesus Bonifacio Tupaz
Commander, United States Navy
B.S., United States Naval Academy, 1960
M.S., Naval Postgraduate School, 1967

Submitted in partial fulfillment of the
requirements for the degree of

DOCTOR OF PHILOSOPHY

from the

NAVAL POSTGRADUATE SCHOOL
June 1977

Author _____

Approved by:

_____   _____
C. Comstock   R. L. Elsberry
Professor of Mathematics   Assoc. Professor of Meteorology

_____   _____
F. D. Faulkner   G. J. Haltiner
Distinguished Professor of   Distinguished Professor of
Mathematics   Meteorology

_____
T. M. Houlihan
Assoc. Professor of Mechanical
Engineering

_____   _____
C.-P. Chang   R. T. Williams
Assoc. Professor of Meteorology Professor of Meteorology
Thesis Advisor   Thesis Advisor

Approved by _____
                        Chairman, Department of Meteorology

Approved by _____
                                            Academic Dean

3

ABSTRACT

The structure and behavior of barotropically unstable
and stable wave disturbances in the vicinity of a zonally
varying easterly jet are studied numerically with a
linearized barotropic vorticity equation on a β-plane. The
easterly jet is approximated by a Bickley jet with a slow
zonal variation. The numerical results are also compared
with a simple mechanistic analytical model using the local
phase speed and growth rate concepts. The results are
grossly similar in several respects to that expected from
the parallel flow theory of barotropic instability, however,
the resultant structure of the waves causes a spatial growth
rate greater than predicted by the local growth rates
computed with a parallel flow model. In the stable region,
the structure leads to strong dynamic damping. When a
uniform advective velocity is added to a variable mean flow,
the differences between the behavior of the computed waves
and that implied by the parallel flow theory are somewhat
reduced. The waves remove kinetic energy from the mean
flow and most of this energy is removed on the downwind side
of the jet. The computed structure and behavior of the waves
have a number of features that resemble those observed in
the vicinity of the upper troposphere easterly jet during
the summer monsoon.

TABLE OF CONTENTS

5

LIST OF FIGURES

LIST OF SYMBOLS

t	Time
x,y	Eastward and northward coordinates, respectively
u	Velocity component in the x-direction
v	Velocity component in the y-direction
ψ	Streamfunction field
ζ	Vorticity field
$(\overline{})$	Mean field operator as a function of x and y
$(\,')$	Disturbance field operator as a function of x, y, and t
β	North-south gradient of earth's vorticity
Q	Forcing function representing non-barotropic effects
D_f	Coefficient of frictional damping
c	Local disturbance phase velocity of parallel flow model
c^*	Local disturbance phase velocity of complete numerical model
$\hat{c}$	Doppler-shifted phase velocity
U_o	Constant zonal advective velocity
k	Disturbance wavenumber
L	Disturbance wavelength
$\tilde{L}$	Wavelength of mean fields' cosine zonal variation
x_o	Initial longitude for measuring wave amplitude envelope
ω	Disturbance frequency
$\hat{\omega}$	Doppler-shifted frequency

D	Half-width of the channel
d	Characteristic length scale of jet
$\bar{d}$	Half-width of jet
Δ	Finite difference operator
∇^2	Laplacian operator
J	Jacobian operator
n	Temporal growth rate from parallel flow model
m	Spatial growth rate from parallel flow model
m*	Spatial growth rate from complete numerical model
θ	Phase tilt of parallel flow model
θ*	Phase tilt of complete numerical model
$\langle\psi'\rangle$	Wave packet envelope from complete numerical model
$F(x)$	Wave packet envelope from simple analytical model
$\langle(\ )\rangle$	Double integration over y-domain and over one time period
$\bar{\rho}$	Mean density
p	Pressure field
k'	Disturbance kinetic energy

ACKNOWLEDGMENT

The author expresses his sincerest appreciation to Professors C-P Chang and R. T. Williams for thier very patient and helpful guidance and suggestions throughout the course of this research.

Sincere appreciation is also extended to Professor F. D. Faulkner for his help in modifying the Poisson equation Direct Solver, subroutine POISDD, and to Professors C. Comstock and R. L. Elsberry for reading the thesis and making helpful comments.

A very special appreciation is extended to all the W. R. Church Computer Center personnel who provided out-standing computing support.

A very warm thank you is extended to the author's wife, Maria, for without her patience, devotion, encouragement and unyielding support throughout this entire effort, this research would not have been accomplished.

I. INTRODUCTION

In the Northern Hemisphere summer, a moderately strong easterly jet exists south of the Tibetan high near the 200 mb level (Krishnamurti, 1971a, 1971b). Synoptic-scale moving disturbances occur at the level of the jet, and it appears that these disturbances arise from barotropic instability of the mean flow. The jet contains regions of large vorticity gradients where the necessary condition for barotropic instability is sometimes locally satisfied. If the observed disturbances were the result of barotropic instability, they would extract energy from the mean zonal flow and the planetary-scale waves, since the latter combine with the zonal flow to give the large vorticity gradients south of the Tibetan high. In fact, Kanamitsu et al. (1972) have shown that wavenumbers 6-8 in the wind spectrum in the region between 15S and 15N receive energy through barotropic interaction with the zonal and wavenumber 1 flow. Furthermore, Krishnamurti (1971a) studied the wavenumber spectra of the meridional wind component for selected tropical latitudes and he found a peak in the spectra near wavenumbers 6-8 at latitudes near the easterly jet.

Colton (1973) studied barotropic interactions between quasi-stationary long waves and transient synoptic waves using a semi-spectral numerical model. His long waves were forced with a specified divergence field following the

12

diagnostic model of Holton and Colton (1972). Results from a long term integration of his model reproduced several features of the upper tropospheric general circulation. In particular, his model simulated the disturbances observed by Krishnamurti (1971a, 1971b) in the vicinity of the easterly jet. His model showed that wave disturbances entering upstream of the easterly jet regime grow and increase their speed and wavelength as they approach the longitude of the jet velocity maximum, achieve their maximum amplitude a considerable distance downstream of the jet maximum, and eventually decay as the disturbances move out of the easterly jet regime. Furthermore, the high and low pressure centers of these transient wave disturbances occur on the wings of the central axis of the jet stream. Colton concluded that the transient disturbances are due to scale interactions involving short-term barotropic instability.

In both Krishnamurti's observational and Colton's numerical studies, the zonal variation of the jet apparently has significant effects on the dynamic behavior of the transient disturbances. This study is an attempt to under-stand better such effects. This is a linear study, therefore, the results can only be suggestive of the complicated nonlinear behavior of the real atmosphere. However, since the ampli-tudes of synoptic waves are generally of smaller magnitude in the tropics than in middle and higher latitudes, a linear

13

stability approach should be a reasonable approximation to the real atmosphere.

This study is an extension of the linear barotropic instability theory developed over the years by various investigators. The extension of this study is the zonal variation of the basic flow. Rayleigh (1890, 1913) developed the concept of hydrodynamic instability and Kuo (1949) extended this concept to a rotating atmosphere by including the beta term. Since then, many investigators have studied the stability of barotropic zonal flows. Kuo (1949, 1951), Lipps (1962), Yanai and Nitta (1968) investigated barotropic instability of parallel symmetric westerly jet flows. Nitta and Yanai (1969), Yamasaki and Wada (1972), and Kuo (1973) extended this theory to parallel symmetric easterly jet flows. Lipps (1965, 1970) and Kuo (1973) further extended the concept to parallel asymmetric barotropic zonal flows. In general, when the necessary criterion for linear barotropic instability is satisfied, normal mode solutions for barotropic unstable waves have certain properties: 1) they exist within a range of intermediate wavelengths, 2) they have a latitudinal tilt opposite to the shear of the barotropic zonal wind and this tilt creates momentum fluxes which redistribute the kinetic energy from the mean zonal flow to the disturbance, 3) their phase speeds in a westerly jet are less then the speed of the maximum westerly wind, and 4) their phase speed in an

easterly jet may be greater than the maximum easterly wind (Pedlosky, 1964; Yamasaki and Wada, 1972). In this case, however, the growth rates are generally very small.

Nitta and Yanai (1969) modified the concept that unstable solutions exist only within an intermediate range of wavelengths. For an easterly sinusoidal jet flow, they found a distinct short wave cut-off but no apparent long wave cut-off for instability. Yamasaki and Wada (1972) modified this by showing that the long wave cut-off is dependent on the strength and sharpness of this sinusoidal easterly jet. For very strong and sharp velocity profiles, the long wave cut-off approaches infinity. For relatively weak but still unstable profiles, a finite long wave cut-off exists for this jet. Kuo (1973) referred to this long wave cut-off region as the modified Rossby regime in his numerical study for an easterly Bickley jet.

All these stability studies have used parallel barotropic flows, i.e., there is no zonal variation in the basic flow. Lorenz (1972), however, investigated primarily by analytical means the barotropic instability of a flow pattern which varies with longitude. The basic flow is a neutral Rossby wave superposed on a uniform westerly flow. Essentially, this flow depicts the progression of large scale waves embedded in a westerly current. Zonal flows of mid-latitudes are generally considered to be barotropically stable, but Lorenz showed that a uniform zonal flow together

with superposed neutral Rossby waves may be unstable with respect to further perturbations. Lorenz found that the growth rate of the perturbations is comparable to the growth rate of the errors of large numerical atmospheric models. Based on this, Lorenz suggested that barotropic instability may be partly responsible for the unpredictability of the real atmosphere.

In addition to the regular or normal mode eigensolutions, there are "singular" or "continuum" mode solutions which have been discussed by Rayleigh (1913), Case (1960), Pedlosky (1964), and Yanai and Nitta (1968). These "singular" solutions correspond to continuous eigenvalues of phase velocity (c) which are equal to the basic flow, $U(y)$, somewhere in the zonal current. Since these "singular" solutions are continuous, there is an infinite number of solutions. Case showed that these continuum modes are needed to form a complete set of solutions. He also showed that the disturbance formed by the sum of the continuum modes has a y-structure tilt in the same sense as the basic flow shear and that it usually decays as $1/t$ or faster, where t represents time.

It is clear that in the real atmosphere, "mean flows" vary both in space and time. They are neither purely barotropic nor purely baroclinic, and in including both effects in a linear stability study is a very difficult task. Most of the investigators have examined the dynamic

instability problem by studying each effect separately. This study, however, focuses only on barotropic instability. We hope that a better understanding of the kind of upper tropospheric waves studied by Krishnamurti (1971a, 1971b) and Colton (1973) near the easterly jet can be achieved by studying the behavior of barotropic waves in a region of a variable mean easterly wind. We are especially interested in the situation where the waves move into and out of barotropically unstable regions. Therefore, the objective of this work is to determine the dynamic stability behavior, the structure and the energetics of barotropic waves propagating in a zonally varying mean wind.

With a very simple analytical model, Pedlosky (1976) studied the finite amplitude dynamics in a zonally varying baroclinic current. The mean flow of his model changes abruptly from a weakly unstable regime with a constant growth rate to a stable regime downstream. He found that disturbances may propagate into stable regions substantially undiminished, retaining a considerable memory of its history in a locally unstable region.

The mean flow in our barotropic study, however, has a full downstream variation such that the stability of the mean flow ranges from locally strong instability to locally strong stability.

Our approach is as follows: firstly, we develop a numerical model based on the linear non-divergent barotropic vorticity equation on a beta-plane incorporating the dynamics of transient barotropic waves in a region of variable mean wind. The mea   wind is an easterly hyperbolic secant-squarred (Bick   d the mean meridional wind is derived in such a way that the mean flow is non-divergent. Secondly, using this numerical model, we conduct selected case studies to determine fundamental dynamic stability and energetic properties of these barotropic waves. Thirdly, we compare the results obtained from the numerical model with the parallel flow theory. This is done by constructing a simple mechanistic analytical model which incorporates the local stability concept of the parallel flow theory. This comparison gives us further insights on the effect of the variable mean wind.

The domain of the numerical model consists of an open channel with rigid walls at the north and south boundaries. The basic flow is a slowly varying easterly Bickley jet. A periodic forcing is applied on the inflow or eastern boundary such that periodic perturbations are generated from this boundary into the channel flow which represents waves moving into the region from the east. The western boundary condition allows the waves to move out of the channel. As the waves move through the region, they grow or decay in relation to the local stability properties of the mean flow, whereas at each point the fields vary periodically.

18

II. NUMERICAL MODEL

A. GENERAL FORMULATION

The governing equations are the barotropic vorticity equation using a beta (β) plane approximation:

$$\frac{\partial \zeta}{\partial t} + u\frac{\partial \zeta}{\partial x} + v\frac{\partial \zeta}{\partial y} + \beta v = Q - D_f \zeta \qquad (2.1)$$

and the non-divergent continuity equation

$$\frac{\partial u}{\partial x} + \frac{\partial v}{\partial y} = 0 \; , \qquad (2.2)$$

where

$$\zeta \equiv \frac{\partial v}{\partial x} - \frac{\partial u}{\partial y} \; . \qquad (2.3)$$

Here β is the north-south gradient of the earth's vorticity and is given by its value at 10° latitude. Q is a forcing function representing non-barotropic effects which is required to maintain the vorticity field, D_f is a frictional coefficient. Since the flow is two-dimensional and non-divergent, a streamfunction (ψ) is defined such that

$$u = -\frac{\partial \psi}{\partial y} \; , \quad v = \frac{\partial \psi}{\partial x} \; , \qquad (2.4)$$

thus

$$\zeta = \nabla^2 \psi \; . \qquad (2.5)$$

Here u and v are the velocities of the flow in the x and y direction, respectively. Equation (2.1) now becomes

$$\frac{\partial}{\partial t}\nabla^2 \psi - \frac{\partial \psi}{\partial y}\frac{\partial \nabla^2 \psi}{\partial x} + \frac{\partial \psi}{\partial x}\frac{\partial \nabla^2 \psi}{\partial y} + \beta\frac{\partial \psi}{\partial x} = Q - D_f \nabla^2 \psi \qquad (2.6)$$

19

The governing equations are linearized by separating quantities into the following form:

$$\psi(x,y,t) = \bar{\psi}(x,y) + \psi'(x,y,t) \ . \qquad (2.7)$$

Here the bars are the basic state variables and the primes are the perturbation quantities. The mean streamfunction $\bar{\psi}(x,y)$ satisfies the mean vorticity equation when a non-barotropic source term is added. The basic state equation is therefore

$$- \frac{\partial \bar{\psi}}{\partial y} \frac{\partial \nabla^2 \bar{\psi}}{\partial x} + \frac{\partial \bar{\psi}}{\partial x} \frac{\partial \nabla^2 \bar{\psi}}{\partial y} + \beta \frac{\partial \bar{\psi}}{\partial x} = \bar{Q} - D_f \nabla^2 \bar{\psi} \ , \qquad (2.8)$$

which is non-linear. $\bar{Q}$ is needed to maintain the basic vorticity field in steady state. The resultant linearized perturbation equation is:

$$\frac{\partial}{\partial t} \nabla^2 \psi' - \frac{\partial \bar{\psi}}{\partial y} \frac{\partial \nabla^2 \psi'}{\partial x} + \frac{\partial \bar{\psi}}{\partial x} \frac{\partial \nabla^2 \psi'}{\partial y} - \frac{\partial \psi'}{\partial y} \frac{\partial \nabla^2 \bar{\psi}}{\partial x}$$

$$+ \frac{\partial \psi'}{\partial x} \frac{\partial \nabla^2 \bar{\psi}}{\partial y} + \beta \frac{\partial \psi'}{\partial x} = - D_f \nabla^2 \psi' \ . \qquad (2.9)$$

The advective terms in (2.9) can be written in Jacobian form such that

$$\nabla^2 \frac{\partial \psi'}{\partial t} = - J(\bar{\psi}, \nabla^2 \psi') - J(\psi', \nabla^2 \bar{\psi}) - \beta \frac{\partial \psi'}{\partial x} - D_f \nabla^2 \psi' \ , \qquad (2.10)$$

where (2.10) is a Poisson equation with the tendency of the perturbation stream-function as the dependent variable. The right side of (2.10) is the forcing or non-homogeneous part

20

of the Poisson problem for $\partial \psi'/\partial t$. The north-south boundaries
are rigid walls where

$$\psi' = 0 , \tag{2.11}$$

and

$$\frac{\partial \zeta'}{\partial y} = 0 . \tag{2.12}$$

The inflow or eastern boundary conditions are specified such
that

$$\psi'(0,y,t) = A(y) \sin(\omega t) + \beta(y) \cos(\omega t), \tag{2.13}$$

and

$$\frac{\partial \psi'}{\partial t} (0,y,t) = A(y)\omega\cos(\omega t) - \beta(y)\omega\sin(\omega t), \tag{2.14}$$

where ω is the specified frequency of the forcing. $A(y)$
and $B(y)$ are the y-structure coefficients of the forcing
which are described in Chapter IV. The purpose of this
forcing is to introduce waves into the region from the east.
The other condition on the inflow boundary is

$$\zeta'(0,y,t) = \nabla^2 \psi' = - k^2 \psi' + \frac{\partial^2 \psi'}{\partial y^2} . \tag{2.15}$$

This expression follows because it is expected that ψ' will
have a spatial variation of the form e^{ikx}. The determination
of k is discussed later. This boundary forcing is expected
to lead to periodic wave disturbances throughout the domain
after a certain time period of numerical integration. It
turns out that the outflow boundary conditions are crucial

21

for attaining this periodic state, because the wave disturb-
ances must be able to propagate freely out of this boundary.
Therefore, a Sommerfeld radiation condition (Pearson, 1974)
for both the tendency and the vorticity is used to approxi-
mate this mechanism on the outflow boundary:

$$\frac{\partial}{\partial t}\left(\frac{\partial \psi'}{\partial t}\right) = -c_{r_0}\frac{\partial}{\partial x}\left(\frac{\partial \psi'}{\partial t}\right), \quad \text{and} \qquad (2.16)$$

$$\frac{\partial \zeta'}{\partial t} = -c_{r_0}\frac{\partial \zeta'}{\partial x}. \qquad (2.17)$$

Here c_{r_0} is a specified constant phase velocity. Pearson
(1974) showed that the Sommerfeld radiation condition is a
consistent boundary condition for numerical models of initial
value systems admitting dispersive waves. The fundamental
problem with most outflow boundary conditions is the reflec-
tion of incident waves from a boundary back into the interior
region. This is usually disastrous for numerical models
admitting dispersive waves. Pearson showed that, if c_{r_0} is
chosen judiciously, the longwaves move smoothly through the
boundary. For short wavelengths, however, an area with a
large coefficient of viscosity near the boundary is often
required to help control the reflection problem. According
to Pearson, the amount of damping is proportional to the
wavenumber. A Matsuno finite difference scheme is used in
our numerical model. This scheme has a tendency to damp the
short waves thus we need only to use a relatively small
coefficient of friction to control wave reflection at the

22

outflow boundary. A friction coefficient of $D_f = .15 \times 10^{-5}$ sec^{-1} is used which is equivalent to an e-folding decay time of approximately 7.7 days.

B. ZONALLY VARYING BASIC FLOW

The basic velocity field is an easterly Bickley jet defined by

$$\bar{u}(x,y) = - U(x) \, sech^2(\frac{y}{d(x)}) - U_o = - \frac{\partial \bar{\psi}}{\partial y} \; . \qquad (2.18)$$

Here $d(x)$ is a characteristic length scale of the jet and is related to the half width $\tilde{d}(x)$ (Kuo, 1973) by

$$\tilde{d}(x) = - 1.76 \; d(x) \; . \qquad (2.19)$$

$U(x)$ is the velocity of the jet at $y=0$ and U_o is a constant velocity. The basic flow streamfunction $(\bar{\psi})$ is specified to be constant at both the southern $(y=-D)$ and northern $(y=D)$ boundaries as follows:

$$\left. \begin{array}{l} \bar{\psi}(-D) = C_1 \\ \bar{\psi}(D) = C_2 \end{array} \right\} \quad , \quad \text{where} \qquad (2.20)$$

$$(2.21)$$

$$\bar{\psi}(x,y) = U(x) \int_{-D}^{y} sech^2(\frac{y}{d(x)}) dy + U_o \int_{-D}^{y} dy + \bar{\psi}(-D),$$

and

$$\bar{\psi}(D) = U(x) \int_{-D}^{D} sech^2(\frac{y}{d(x)}) dy + U_o \int_{-D}^{D} dy$$

$$+ \bar{\psi}(-D) = C_2 . \qquad (2.22)$$

For a symmetric jet profile about y=0, $C_1 = C_2$. Equations
(2.21) and (2.22) are conveniently simplified:

$$\bar{\psi}(x,y) = U(x)d(x) \left\{ \tanh\left(\frac{y}{d(x)}\right) + \tanh\left(\frac{D}{d(x)}\right) \right\}$$

$$+ U_0 y + U_0 D + \bar{\psi}(-D), \qquad (2.23)$$

and

$$\bar{\psi}(D) = 2U(x)d(x) \tanh\left(\frac{D}{d(x)}\right) + 2U_0 D + \bar{\psi}(-D) . \qquad (2.24)$$

From (2.23), the jet velocity at y=0 is given by:

$$U(x) = \left[\frac{\bar{\psi}(D) - 2U_0 D - \bar{\psi}(-D)}{2d(x)} \right] \coth\left(\frac{D}{d(x)}\right) . \qquad (2.25)$$

Therefore, if d(x) varies slowly in x, then, so does the
basic flow. The x-variation for the characteristic length
scale is given by

$$d = \begin{cases} 850 \text{ km} + 350 \text{ km} \left\{ \cos\left[2\pi \frac{(x-\tilde{x}_0)}{\tilde{L}} \right] \right\}, & x \geq \tilde{x}_0 \\ 1200 \text{ km}, & x \leq \tilde{x}_0 \end{cases} . \qquad (2.26)$$

Here $\tilde{x}_0$ is the longitude where the x-variation of the cosine
function starts and $\tilde{L}$ is the wavelength of this variation.

Figures 1-3 show the basic fields of streamfunction
$\bar{\psi}(x,y)$, zonal velocity $\bar{u}(x,y)$ and vorticity $\bar{\xi}(x,y)$,
respectively. Here $\tilde{L}$ is set to 43,000 km. The domain is
40,125 km long and 4,000 km wide (D = 2,000 km). At y=0,
the basic zonal velocity is -15.51 m sec^{-1} at the inflow
boundary (x = 14,625 km) increasing slowly to a maximum value

24
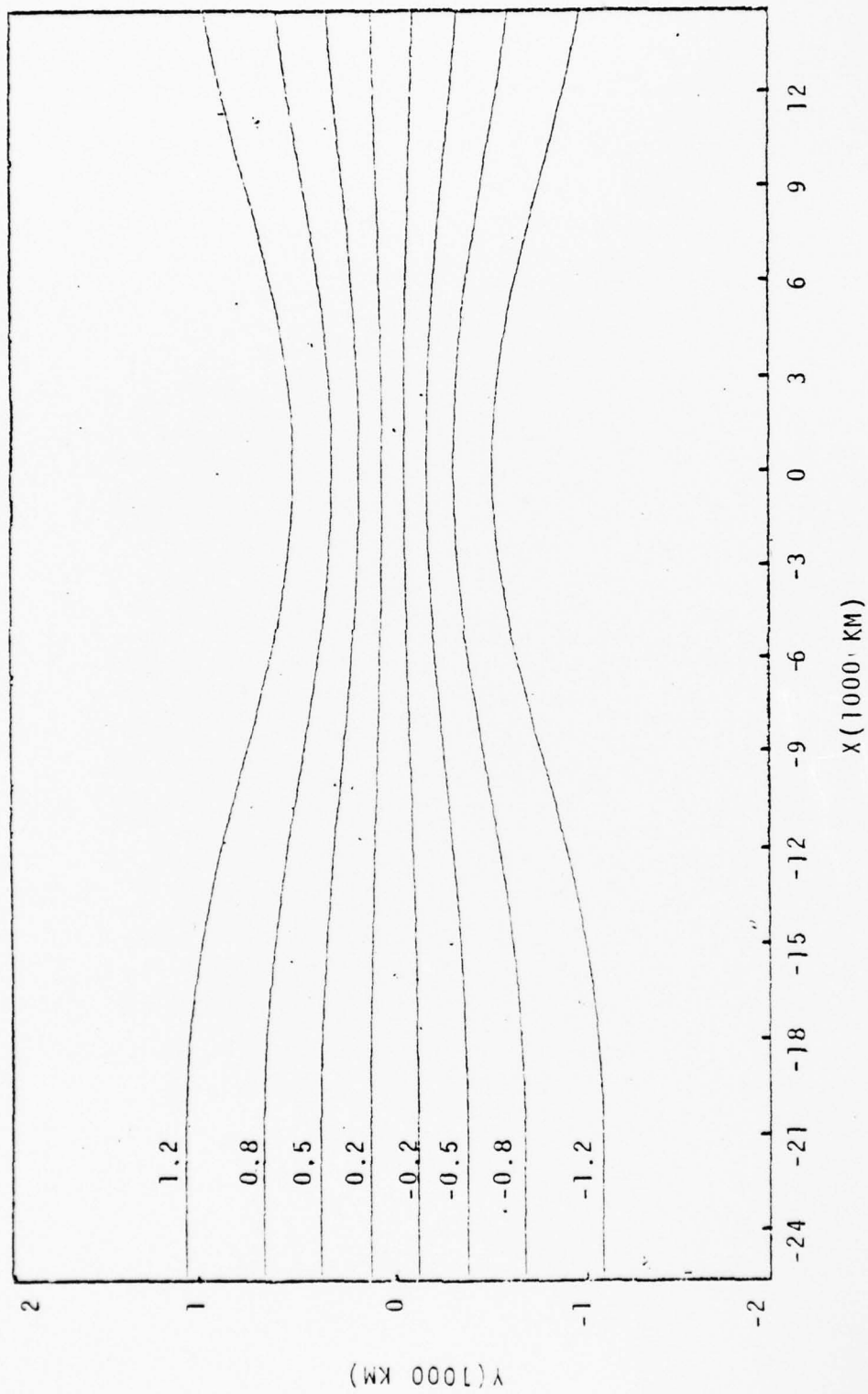
Fig. 1. Experiment I. The $\bar{\psi}(x,y)$ field ($\times 10^7 \, m^2 \, sec^{-1}$).
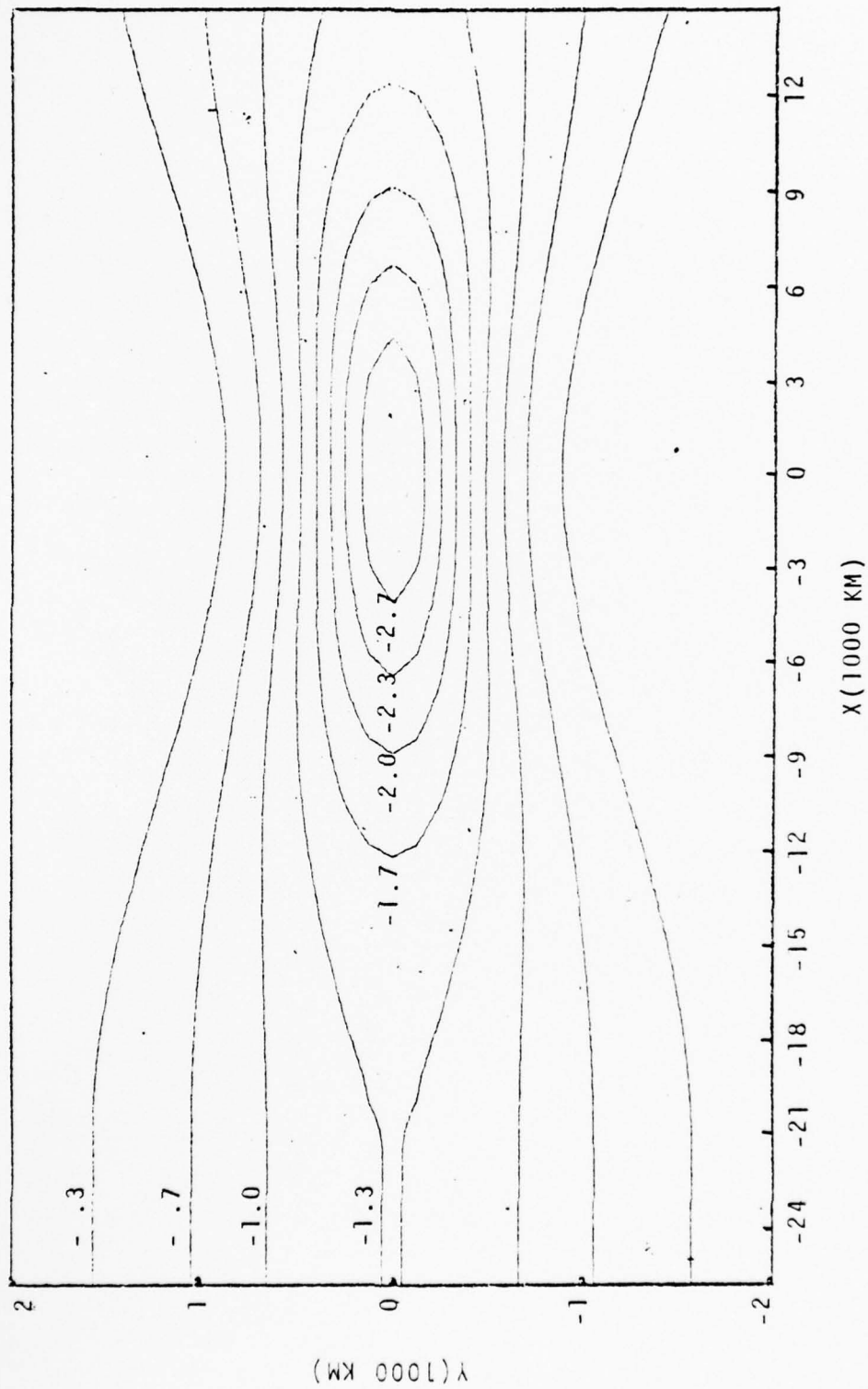
Fig. 2. Experiment I. The $\bar{u}(x,y)$ field ($\times 10 \text{ m sec}^{-1}$).
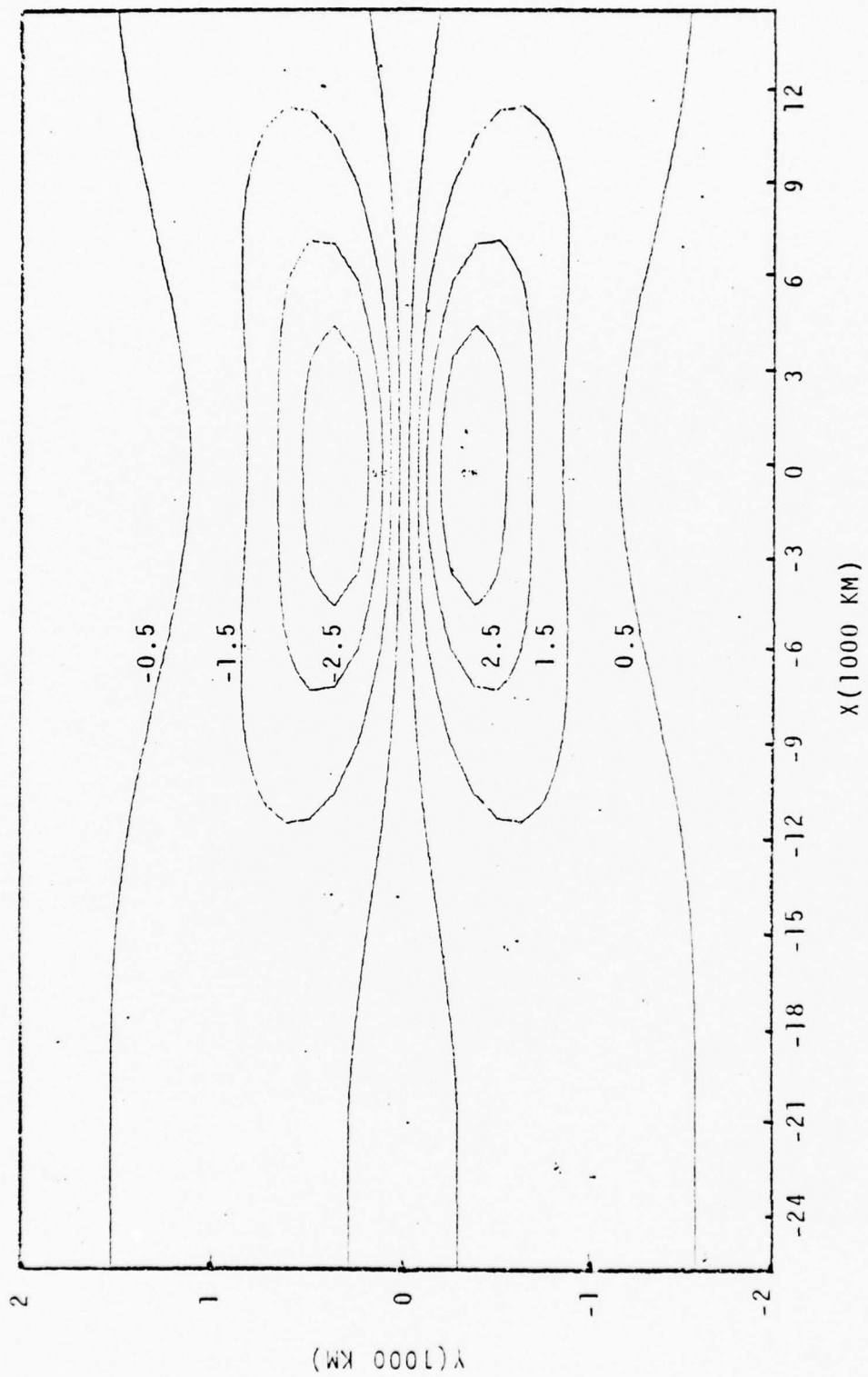
Fig. 3. Experiment I. The $\bar{\zeta}(x,y)$ field ($\times 10^{-5}$ sec^{-1}).

of -30 m sec^{-1} at x=0. From this longitude the central velocity slowly decreases downstream to a minimum value of -13.4 m sec^{-1} at x = -21,375 km. Between this longitude and the outflow boundary (x = -25,500 km), the basic flow is parallel. From Eq. (2.26), we note that the characteristic length scale, d(x), varies between 500 km at $\bar{u}(x,o)_{max}$ and 1200 km at $\bar{u}(x,o)_{min}$.

III. LOCAL STABILITY OF BASIC FLOW

The local growth rate of the variable mean flow of the numerical model is first determined by a parallel flow (i.e., no x-variation) numerical model of Williams et al. (1971) in order to gain some insight on the stability characteristics of the mean flow. This model is hereafter referenced as the parallel flow model. By setting $\partial \bar{\psi}/\partial x = 0$ in (2.9) of the numerical model, the governing equation of this model is

$$\left[\frac{\partial}{\partial t} + \bar{u}\frac{\partial}{\partial x} + D_f\right] \nabla^2 \psi' + \left[\beta - \frac{\partial^2 \bar{u}}{\partial y^2}\right] \frac{\partial \psi'}{\partial x} = 0 \ . \qquad (3.1)$$

The symbols of (3.1) have the same meaning as the numerical model of Chapter II, except that the basic flow is given by

$$\bar{u}(y) = - U \ \text{sech}^2\left(\frac{y}{d}\right) \ , \qquad (3.2)$$

where U is a specified constant that scales the magnitude of the central velocity of the Bickley jet (y=0). The characteristic length d is also a specified constant. Assuming that all perturbation quantities are periodic in x, Eq. (3.1) is finite Fourier transformed in x with wavenumber k, and is solved as an initial value problem. This approach gives the phase speed, growth rate, and the wave structure of the most unstable mode. It is convenient to write ψ' in the following form:

$$\psi'(x,y,t) = A(y,t) \ \cos(kx) + B(y,t) \ \sin(kx). \qquad (3.3)$$

Equation (3.3) is substituted into (3.1), and the coefficients of coskx and sinkx are separately set equal to zero. The coskx term gives:

$$\left[\frac{\partial}{\partial y^2} - k^2\right]\frac{\partial A}{\partial t} = -k\left[\bar{u}\left\{\frac{\partial^2}{\partial y^2} - k^2\right\} + \left\{\beta - \frac{\partial^2 \bar{u}}{\partial y^2}\right\}\right]B$$
$$- D_f\left[\frac{\partial^2}{\partial y^2} - k^2\right]A, \qquad (3.4)$$

and the sinkx term gives:

$$\left[\frac{\partial}{\partial y^2} - k^2\right]\frac{\partial B}{\partial t} = k\left[\bar{u}\left\{\frac{\partial^2}{\partial y^2} - k^2\right\} + \left\{B - \frac{\partial^2 \bar{u}}{\partial y^2}\right\}\right]A$$
$$- D_f\left[\frac{\partial^2}{\partial y^2} - k^2\right]B. \qquad (3.5)$$

The boundary conditions are

$$\psi'(x,D,t) = \psi'(x,-D,t) = 0. \qquad (3.6)$$

Equations (3.4) and (3.5) are written in finite difference form such that the second derivative with respect to y of a typical variable A is approximated as

$$\left[\frac{\partial^2 A}{\partial y^2}\right]_j = \left[\frac{A_{j+1} - 2A_j + A_{j-1}}{\Delta y^2}\right], \qquad (3.7)$$

where j is the y-grid index and Δy is the distance between grid points. The model has 32 grid intervals and Δy is set equal to 125 km (the width of the channel is 4000 km). This y-grid structure is the same one used in the complete numerical model. Centered time differences are used for all quantities except those involving friction. The time step

(Δt) is set to 1 hour. The friction terms are evaluated at the previous time step in order to insure linear computational stability (Haltiner, 1971). The integration begins with a forward time step. The boundary conditions (Eq. 3.6) become

$$A = B = 0 \text{ at } y = \pm D. \tag{3.8}$$

Equations (3.4) and (3.5) are solved for the tendencies by the exact method of Richtmyer (1967). These equations can be solved numerically as a function of β, D_f, $\bar{u}(y)$, and k for any initial conditions. These equations are integrated until their solution becomes exponential in behavior. The basic flow $\bar{u}(y)$ is specified for a number of selected longitudes of the variable mean flow of Fig. 2. The wavenumber k is also specified for each integration.

In general, these equations have a set of discrete normal mode solutions as well as a continuous spectrum of solutions (Case, 1960, Pedlosky, 1964 and Yanai and Nitta, 1968). Only the normal mode solutions can give significant growth and the most unstable mode will dominate after a sufficient period of time.

This parallel flow model is numerically integrated to 150 days. The initial disturbance amplitude has a north-south structure with no tilt. The eigensolution obtained includes wave structure of the most unstable mode, and its growth rate and phase speed. By selectively testing different wavelengths, the most unstable wavelength is determined.

Figures 4-7 illustrate the eigensolutions of the most unstable discrete mode for the selected jet profiles. Since the jet flow and the wave disturbance are both symmetric about y=0, only the lower half of the y domain is shown. It is interesting to note that the eigensolution amplitude has three maxima, one at y=0 and one on each wing (only lower wing is shown) of the jet approximately 600-800 km from y=0. It is apparent that when the jet is relatively sharp (i.e., d ≤ 700 km), the central maximum predominates. When the jet is relatively smooth and broad (i.e., d ≥ 800 km), the maximum on the wings predominates. Figure 8 shows the growth rate (n) corresponding to the most unstable wavelengths (L) as a function of x based on the parallel flow model. In a local stability sense, the most unstable wavelengths range between 3650 km at x=0 where the jet has its maximum velocity and 4600 km near the inflow and outflow regions of the jet regime. We observe that locally the greatest instability based on both tilt and growth rate is indicated where the jet achieves its maximum central velocity ($\bar{u}$ = -30 m sec^{-1}). This parallel flow model can only give the most unstable discrete mode; it can not depict any dynamic damping. This is reflected in Fig. 7(b) which corresponds to x = -22,500 km, outside the unstable region. Here the solution exhibits essentially no tilt and the growth rate asymptotically approaches the linear frictional damping rate. This is further discussed in Chapters VI and VII.

32
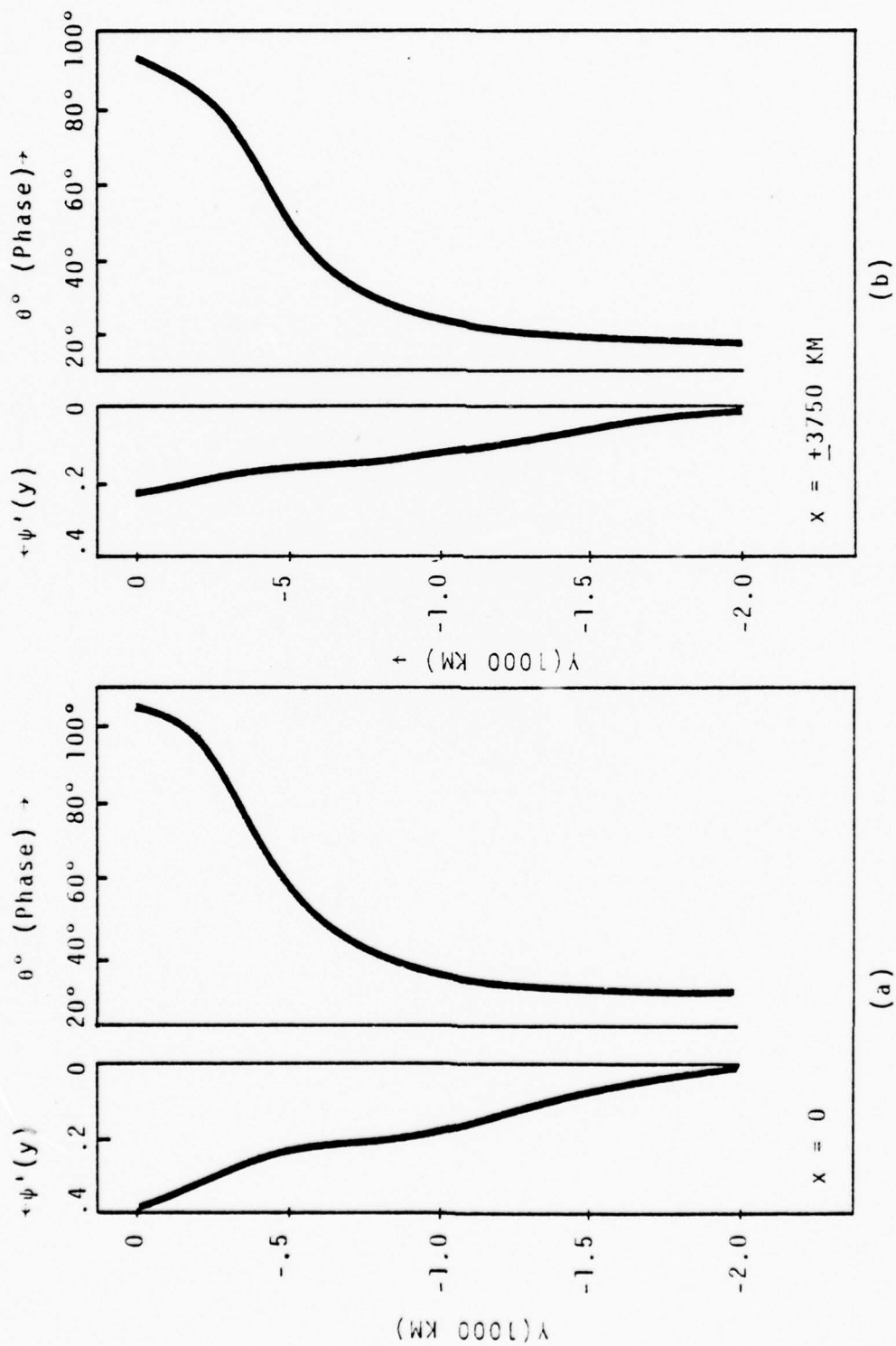
Fig. 4. Parallel flow model: wave structure of the most unstable mode for longitudes (a) x = 0, and x = ±3750 km.

33
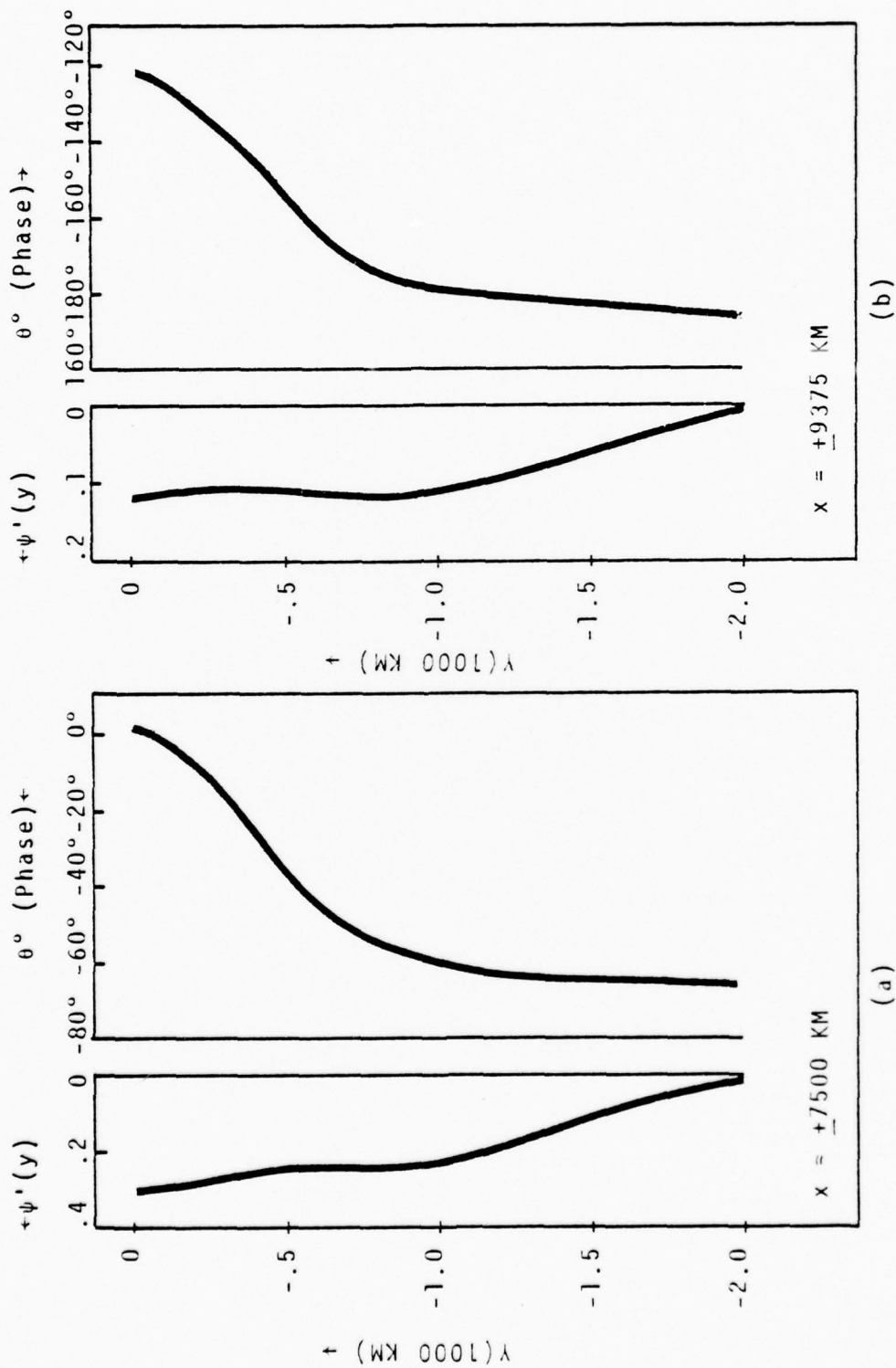
Fig. 5. Parallel flow model wave structure of the most unstable mode
for longitudes: (a) x = ±7500 km, and (b) x = ±9375 km.

34
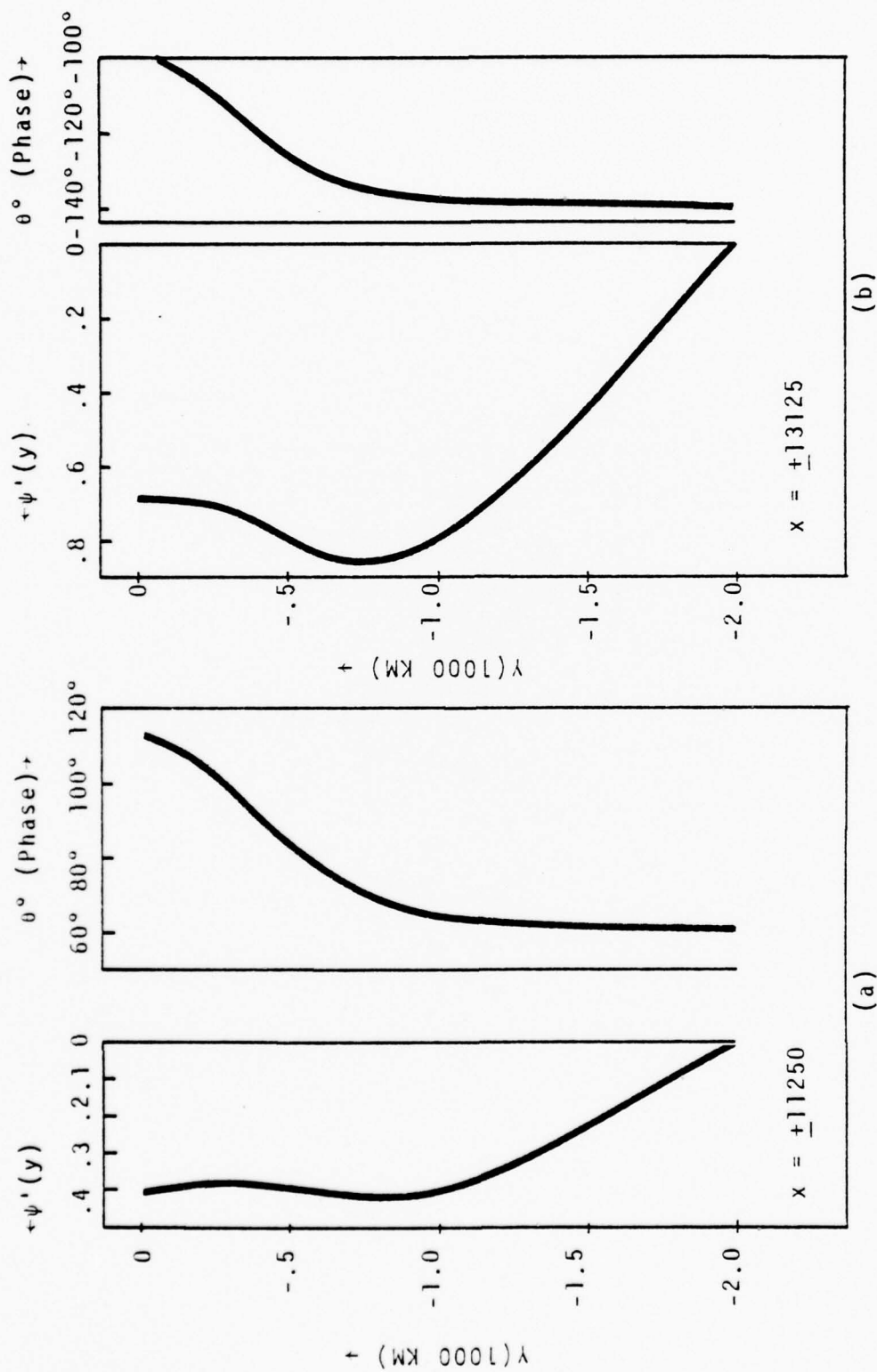
Fig. 6. Parallel flow model wave structure of the most unstable mode for longitudes (a) x = ±11250 km, and (b) x = ±13125 km.

35
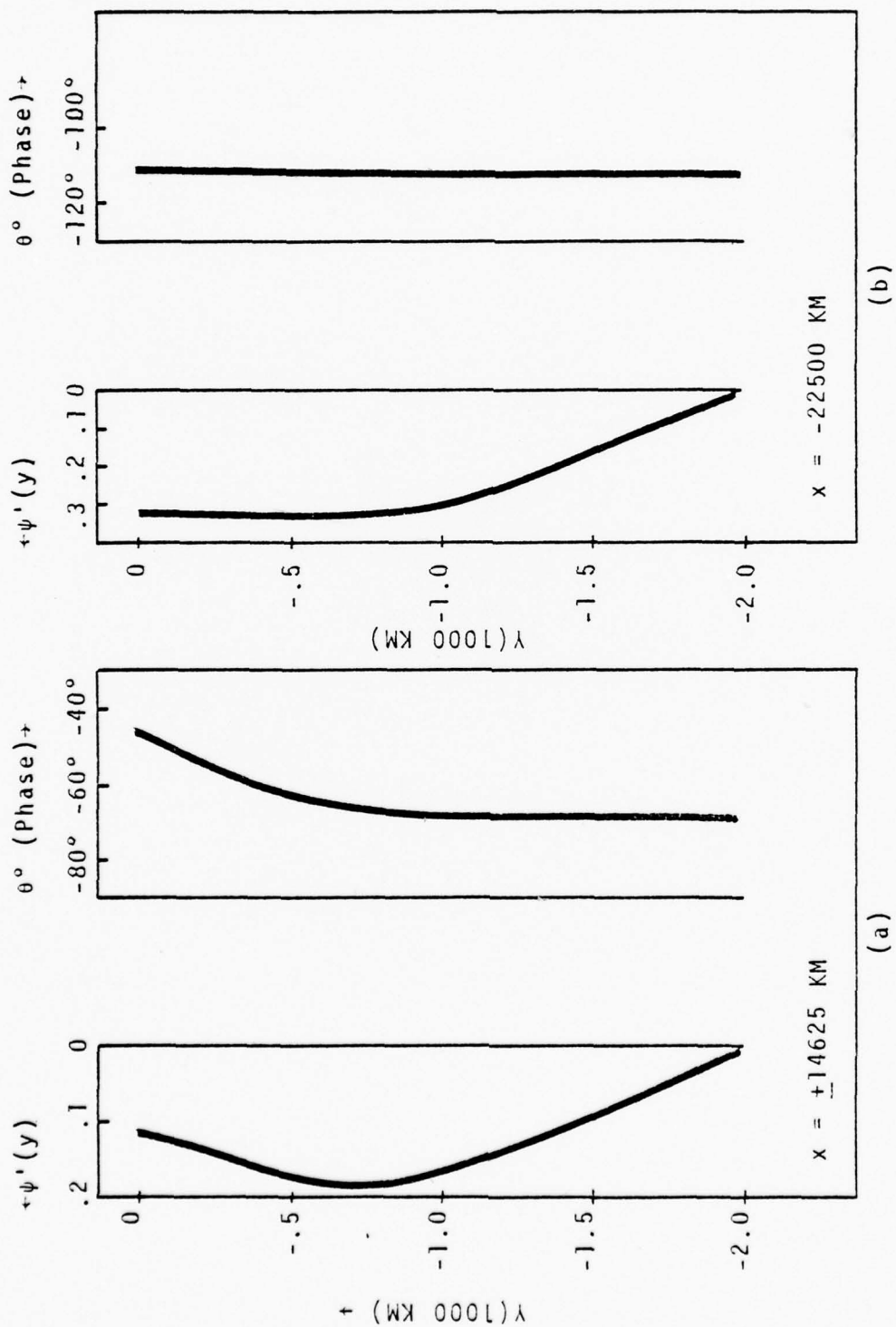
Fig. 7. Parallel flow model wave structure of the most unstable mode for longitudes (a) $x = \pm 14625$ km, and (b) $x = -22500$ km.

36
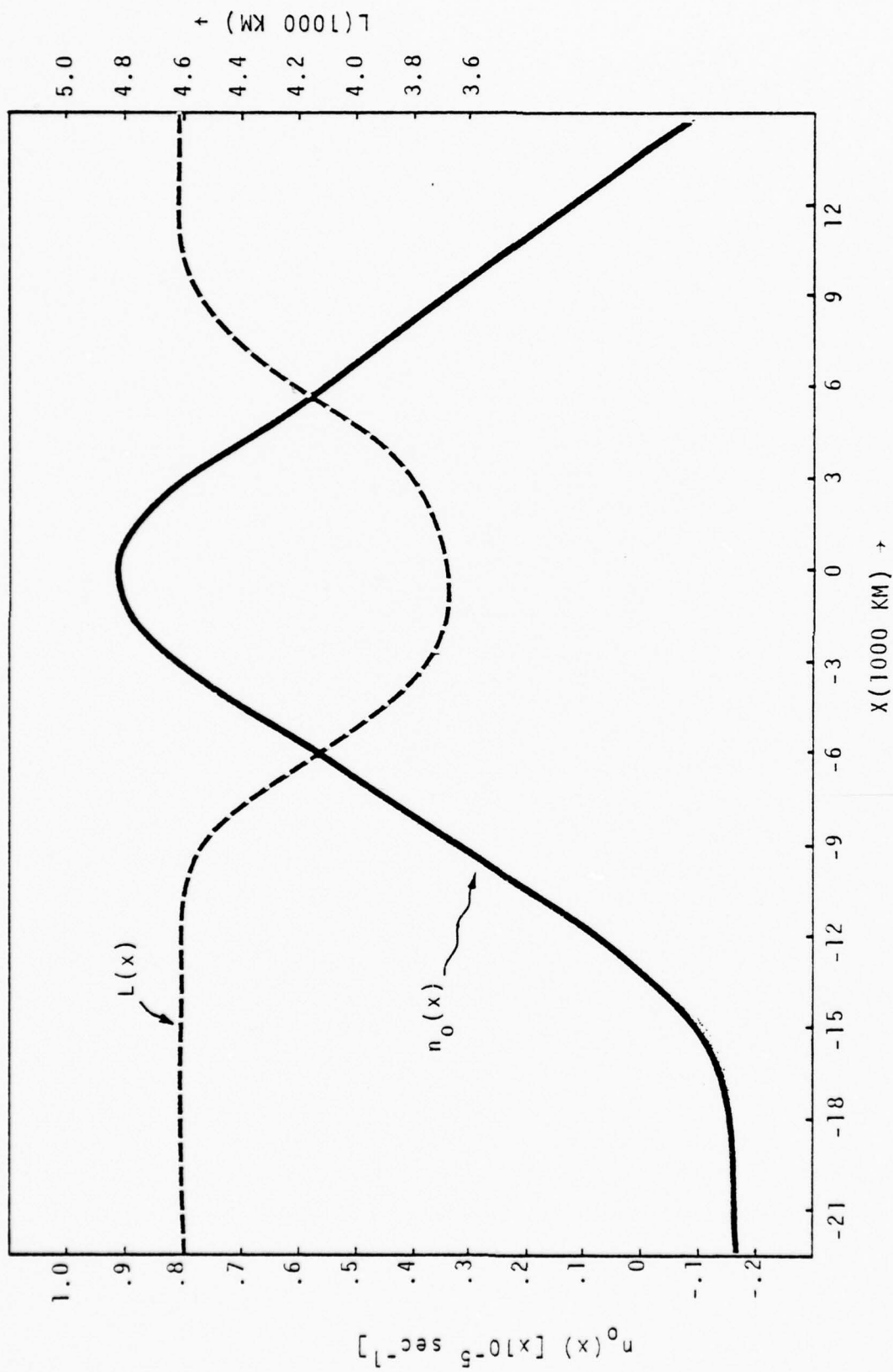
Fig. 8. (a) The most unstable wavelength L(x), and (b) corresponding local growth rate $n_0(x)$, based on the parallel flow model.

37

These results are consistent with those calculated by Kuo (1973) in a numerical study of a parallel Bickley jet and, in a local stability sense, may be viewed as a first approximation of the behavior of moving waves within a zonally-varying mean wind.

IV. FINITE DIFFERENCE EQUATIONS

The governing Eq. (2.9) of the complete numerical model
is written with the advective terms in Jacobian form:

$$\nabla^2 \frac{\partial \psi'}{\partial t} = - J(\bar{\psi}, \nabla^2 \psi') - J(\psi', \nabla^2 \bar{\psi}) - \beta \frac{\partial \psi'}{\partial x} - D_f \nabla^2 \psi' \ , \qquad (4.1)$$

where

$$J(a,b) = \frac{\partial a}{\partial x} \frac{\partial b}{\partial y} - \frac{\partial a}{\partial y} \frac{\partial b}{\partial x} \qquad (4.2)$$

for any two scalar quantities a and b. The Arakawa (1966)
finite difference approximation for the Jacobian is used.
This scheme conserves both the mean square vorticity and the
mean kinetic energy.

We define the tendency of the disturbance streamfunction
by

$$T_{i,j}^t \equiv \left[\frac{\partial \psi'}{\partial t} \right]_{i,j}^t \ , \qquad (4.3)$$

where superscript t is the current time, and subscripts i
and j refer to the x and y grid points, respectively. In the
following finite difference equations, Δt is the time step
and is set equal to one hour. Δx and Δy are the x and y
grid point intervals, respectively. Equation (4.1) is written
using the Matsuno or Euler-backward finite difference scheme:

$$\nabla^2 T_{i,j}^t = - J_{i,j}^t [\bar{\psi}, \nabla^2 \psi'] - J_{i,j}^t [\psi', \nabla^2 \bar{\psi}]$$

$$\qquad (4.4)$$

$$- \beta \left[\frac{\psi'^t_{i+1,j} - \psi'^t_{i-1,j}}{2 \Delta x} \right] - D_f \nabla^2 \psi'^{t-\Delta t}_{i,j} \ ,$$

39

$$\psi_{i,j}^{\prime\,*} = \psi_{i,j}^{\prime\,t} + T_{i,j}^{t}\Delta t, \tag{4.5}$$

$$\nabla^2 T_{i,j}^{*} = -\mathbb{J}_{i,j}^{*}[\bar{\psi}, \nabla^2 \psi^{\prime}] - \mathbb{J}_{i,j}^{*}[\psi^{\prime}, \nabla^2 \bar{\psi}]$$

$$- \beta\left[\frac{\psi_{i+1,j}^{\prime\,*} - \psi_{i-1,j}^{\prime\,*}}{2\Delta x}\right] - D_f \nabla^2 \psi_{i,j}^{\prime\,t-\Delta t} \tag{4.6}$$

$$\psi_{i,j}^{\prime\,t+\Delta t} = \psi_{i,j}^{\prime\,t} + T_{i,j}^{*}\Delta t . \tag{4.7}$$

The finite difference form for the Laplacian of the tendency is given by: (4.8)

$$\nabla^2 T_{i,j}^{t} \equiv \frac{T_{i+1,j}^{t} - 2T_{i,j}^{t} + T_{i,j+1}^{t}}{\Delta x^2} + \frac{T_{i,j+1}^{t} - 2T_{i,j}^{t} + T_{i,j-1}^{t}}{\Delta y^2},$$

and for the Jacobian terms, it is given by:

$$\underset{i,j}{\overset{①}{\mathbb{J}}}^{t} = \frac{1}{4\Delta x \Delta y}\left[(\bar{\psi}_{i+1,j} - \bar{\psi}_{i-1,j})(\zeta_{i,j+1}^{\prime\,t} - \zeta_{i,j-1}^{t}) + \right.$$

$$\left. - (\bar{\psi}_{i,j+1} - \bar{\psi}_{i,j-1})(\zeta_{i+1,j}^{\prime\,t} - \zeta_{i-1,j}^{\prime\,t})\right], \tag{4.9}$$

$$\underset{i,j}{\overset{②}{\mathbb{J}}}^{t} = \frac{1}{4\Delta x \Delta y}\left[\bar{\psi}_{i+1,j}(\zeta_{i+1,j+1}^{\prime\,t} - \zeta_{i+1,j-1}^{\prime\,t}) + \right. \tag{4.10}$$

$$- \bar{\psi}_{i-1,j}(\zeta_{i-1,j+1}^{\prime\,t} - \zeta_{i-1,j-1}^{t}) +$$

$$- \bar{\psi}_{i,j+1}(\zeta_{i+1,j+1}^{\prime\,t} - \zeta_{i-1,j+1}^{t}) +$$

$$+ \bar{\psi}_{i,j-1}(\zeta_{i+1,j-1}^{\prime\,t} - \zeta_{i-1,j-1}^{\prime\,t})\right],$$

40

and

$$\overset{\text{\textcircled{3}}}{J}{}_{i,j}^{t} = \frac{1}{4\Delta x \Delta y} \left[\zeta'^{t}_{i,j+1} (\bar\psi_{i+1,j+1} - \bar\psi_{i-1,j+1}) + \right. \tag{4.11}$$

$$- \zeta'^{t}_{i,j-1} (\bar\psi_{i+1,j-1} - \bar\psi_{i-1,j-1}) +$$

$$- \zeta'^{t}_{i+1,j} (\bar\psi_{i+1,j+1} - \bar\psi_{i+1,j-1}) +$$

$$\left. + \zeta'^{t}_{i-1,j} (\bar\psi_{i-1,j+1} - \bar\psi_{i-1,j-1}) \right] ,$$

where

$$\overset{}{J}{}_{i,j}^{t} [\bar\psi, \nabla^2 \psi'] = \frac{\overset{\text{\textcircled{1}}}{J}{}_{i,j}^{t} + \overset{\text{\textcircled{2}}}{J}{}_{i,j}^{t} + \overset{\text{\textcircled{3}}}{J}{}_{i,j}^{t}}{3} . \tag{4.12}$$

$$\overset{}{J}{}_{i,j}^{t} [\psi', \nabla^2 \bar\psi] \text{ is expanded in the same manner as for}$$

$$\overset{}{J}{}_{i,j}^{t} [\bar\psi, \nabla^2 \psi'] .$$

The Poisson Eq. (4.1) is solved for the tendency with a direct method developed by Sweet (1971). This direct method solves a finite difference approximation to Poisson's equation on a rectangular domain with Dirichlet boundary conditions. The finite difference form of the boundary conditions are as follows:

a) Northern (j=J) and southern (j=0) boundaries:

$$\psi'^{t}_{i,j} = 0 : i=0,I \text{ for } j=0 \text{ and } j=J, \tag{4.13}$$

$$\zeta'^{t}_{i,0} = \zeta'^{t}_{i,1} : i=0,I, \tag{4.14}$$

41

$$\zeta_{i,J}^{'t} = \zeta_{i,J-1}^{'t} : \quad i=0,I. \tag{4.15}$$

b)   Inflow or eastern boundary (i=I, j=0, j)

$$\psi_{I,j}^{'t} = \tilde{A}_j \sin(\omega \ell \Delta t) + \tilde{B}_j \cos(\omega \ell \Delta t), \tag{4.16}$$

$$T_{I,j}^t = \tilde{A}_j \omega \cos(\omega \ell \Delta t) - \tilde{B}_j \omega \sin(\omega \ell \Delta t), \tag{4.17}$$

and

$$\zeta_{I,j}^t = -k_{I,j}^2 \psi_{I,j}^{'t} + \frac{\psi_{I,j+1}^{'t} - 2\psi_{I,j}^{'t} + \psi_{I,j-1}^{'t}}{\Delta y^2} \tag{4.18}$$

where ω is the specified frequency and $k_{I,j}$ is a specified wavenumber structure. Time is discretized by:

$$t \equiv \ell \Delta t, \quad \text{where} \quad \ell = 0,1,2,3,4 \ldots \tag{4.19}$$

$\tilde{A}_j$ and $\tilde{B}_j$ are the y-structure coefficients of the forcing (4.14). These coefficients were determined from the eigen-solution of the parallel flow model. The velocity profile for determining A_j and B_j of the inflow boundary condition was selected from the inflow region of the numerical model. This profile is described in Chapter V.

c)   Outflow or western boundary (i=0, j=0, J)

$$T_{0,j}^t = \frac{T_{0,j}^{t-\Delta t}}{1+c_{r_o} \Delta t/\Delta x} + \frac{T_{1,j}^t}{1+\Delta x/(c_{r_o} \Delta t)}, \tag{4.20}$$

$$\zeta_{0,j}^{'t} = \frac{\zeta_{0,j}^{'t-\Delta t}}{1+c_{r_o} \Delta t/\Delta x} + \frac{\zeta_{1,j}^{'t}}{1+\Delta x/(c_{r_o} \Delta t)}, \tag{4.21}$$

42

$$\psi'_{0,j}^{t} = \psi'_{0,j}^{t-\Delta t} + T^*_{0,j} \Delta t. \qquad (4.22)$$

The tendency $T_{0,j}^{t}$ (4.20) and $\varsigma'_{0,j}^{t}$ (4.21) were derived from the analytical Sommerfeld radiation condition (2.16) and (2.17), respectively. Since (2.16) is not in the usual form of the Dirichlet boundary condition, the direct Poisson equation solver, POISDD, had to be modified. Details of this modification are given in the Appendix.

V. EXPERIMENT I

The investigation of the numerical model of the variable mean wind comprises two experiments. Experiment I is the principal one and will be discussed in detail in this chapter. In Experiment II a constant velocity is added to the mean flow and its results will be discussed in Chapter VII.

The forecast equation is integrated in time from an initial state of $\psi ' = 0$. Tne periodic forcing on the eastern boundary causes the interior streamfunction to grow and the integration is continued until the time variation is periodic everywhere with the forcing frequency. By day 70, the model has achieved the fully periodic state and the wave packet envelope has become quasi-stationary. The forcing frequency is varied until the value which gives a maximum perturbation amplitude is found.

The following values are used in Experiment I:

$2D = 4000$ km, $x_R - x_L = 40125$ km, $\bar{u}(0,0) = -30$ m sec^{-1},

$U_o = 0$, $\tilde{L} = 43000$ km, $\Delta x = 375$ km, $\Delta y = 125$ km.

For these parameters the maximum response occurs for a forcing period of 3.25 days. It requires several complete integrations to refine the inflow and outflow boundary conditions for the specified forcing period. Wavenumber (k) for the inflow vorticity boundary condition (4.13) was determined by observing the predominant wavelengths near the inflow region. The radiation phase velocity (c_{r_o}) in the

44

outflow boundary condition (4.15) was similarly determined by observing the predominant wavelengths near the outflow region. Since the domain is periodic, the phase velocity is approximated by the simple relation:

$$c_{r_0} = \frac{\omega}{k_0} . \qquad (5.1)$$

Here ω is the local frequency which, in the fully periodic state, is equal to the forcing frequency, and k_0 is the wave-number measured near the outflow region. Thus, for Experiment I, a phase velocity (c_{r_0}) of -13 m sec^{-1} is used for the outflow Sommerfeld radiation boundary condition.

A.   RESULTS

The solution for the Case I experiment becomes fully periodic after 70 days. The ψ' field at t=70 days is shown in Fig. 9. An entire train of barotropic waves actually exists throughout the length of the channel, but the waves upstream of x = -4,500 km and in the outflow region are not shown in Fig. 9 because of their relatively small amplitude. The maximum wave amplitude occurs at x = -12,750 km and is 2 and 4 orders of magnitude larger than at the jet maximum (x=0) and the inflow boundary (x = 14,625 km), respectively. Figure 10 shows the lower half of phase angle tilt $\theta*(x,y)$ of the wave disturbance y-structure for various values of longitude x. We note that the waves upstream of approximately x = -20,000 km tilt opposite to the mean wind shear, which is necessary for barotropic instability. In fact the tilt near

45

Fig. 9. Experiment I. The ψ' field at t = 70 days.

X(1000 KM) →

Y(1000 KM) →
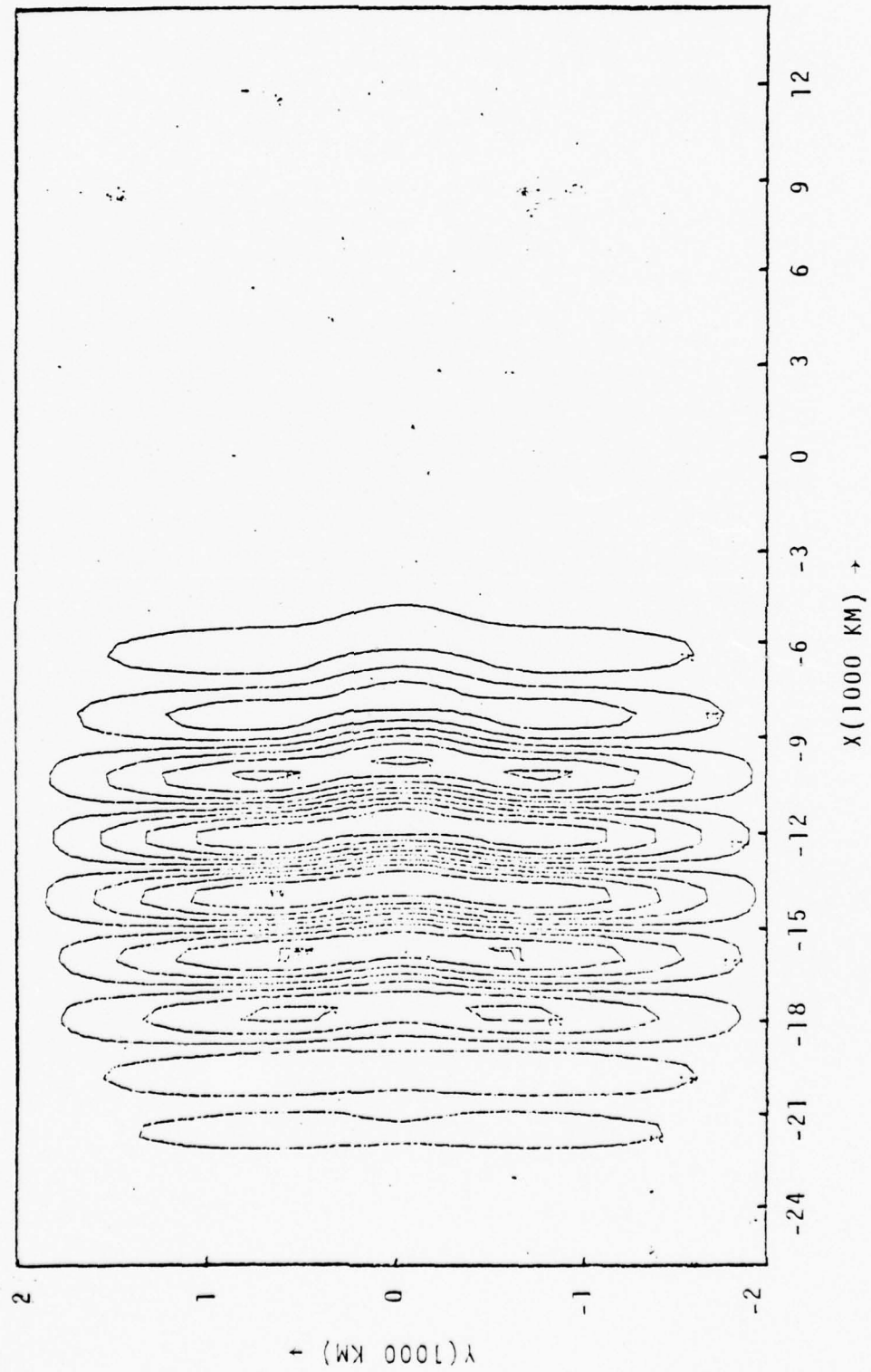
Phase Angle θ (degrees) →
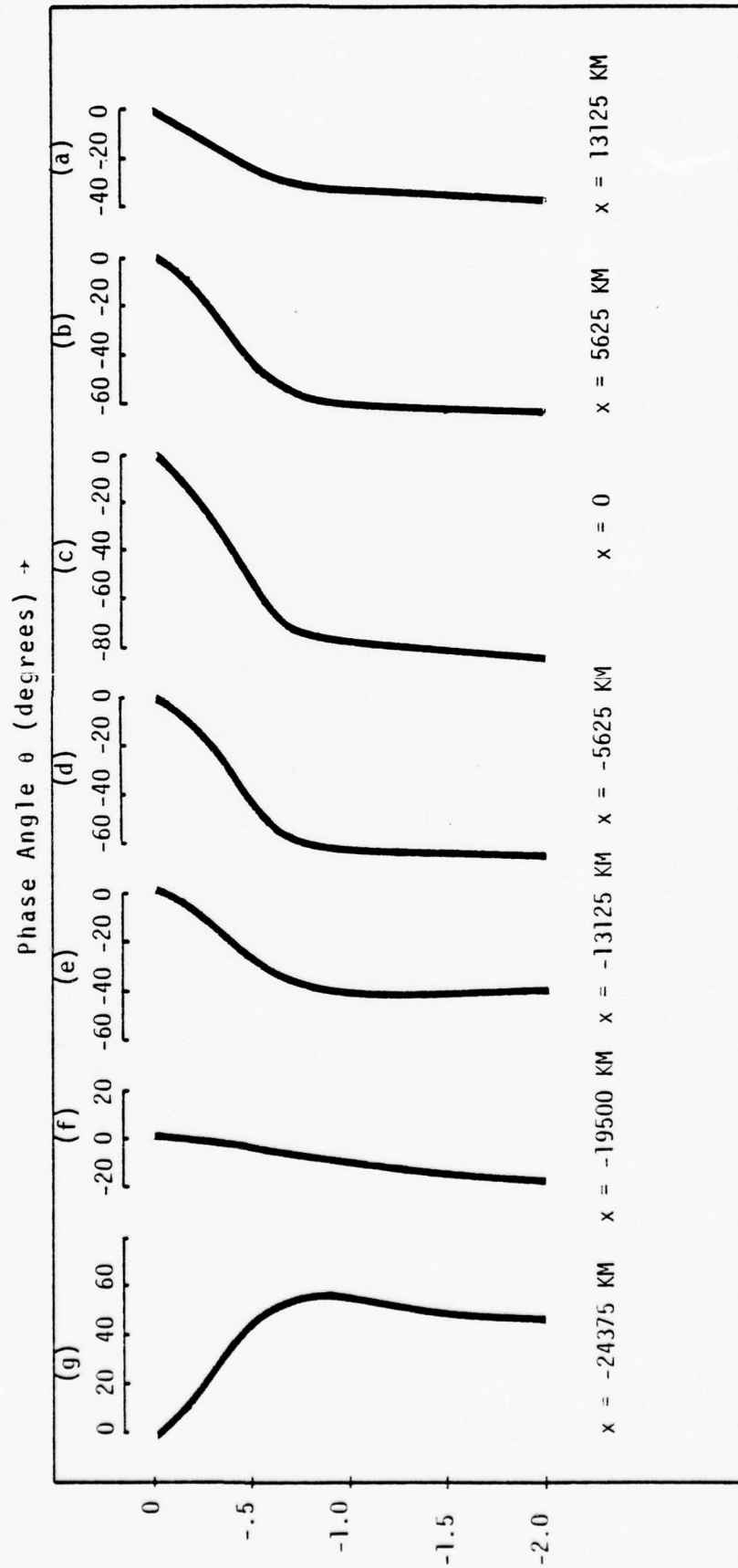
Fig. 10. Experiment I. The phase angle tilt θ*(x,y) for longitudes (a) x = 13125 km (b) x = 5625 km, (c) x = 0, (d) x = - 5625 km, (e) x = -13125 km, (f) x = -19500 km, and (g) x = -24375 km.

47

the inflow boundary shows relatively weak instability and
this tilt slowly increases, reaching a maximum at x=0 where
the jet velocity is maximum. Further downstream, the tilt
slowly decreases and eventually reverses near x = -20,000 km.
This behavior is consistent with the growth rates for the
most unstable wavelengths shown in Fig. 8 which were computed
using the parallel flow model. Near the outflow boundary,
however, the tilt is reversed. This indicates dynamic
stability or a flow of energy from the disturbance back to
the mean flow. Therefore, we observe that the tilt of the
wave disturbance qualitatively adjusts to the local stability
of the mean flow (see Figs. 4-7). We recall that the parallel
flow model can only solve for the most unstable discrete mode,
thus, dynamic damping is not indicated in Fig. 7(b) for the
outflow region.

Figure 11 shows the envelope of the wave packet,
evaluated at y = -750 km, where the disturbance amplitude is
large. This envelope $<\psi'(x)>$ is obtained by recording the
maximum and minimum ψ' values that occur at each longitude
over a period of ten days after the solution becomes fully
periodic. If a larger time interval were chosen, the envelope
would not change. Note that the maximum amplitude occurs in
the area where the local growth rate becomes zero (see Fig. 8).
The smoothness of the fields in Figs. 9 and 11 indicate that
the radiation outflow boundary condition is working properly.

X(1000 KM) →
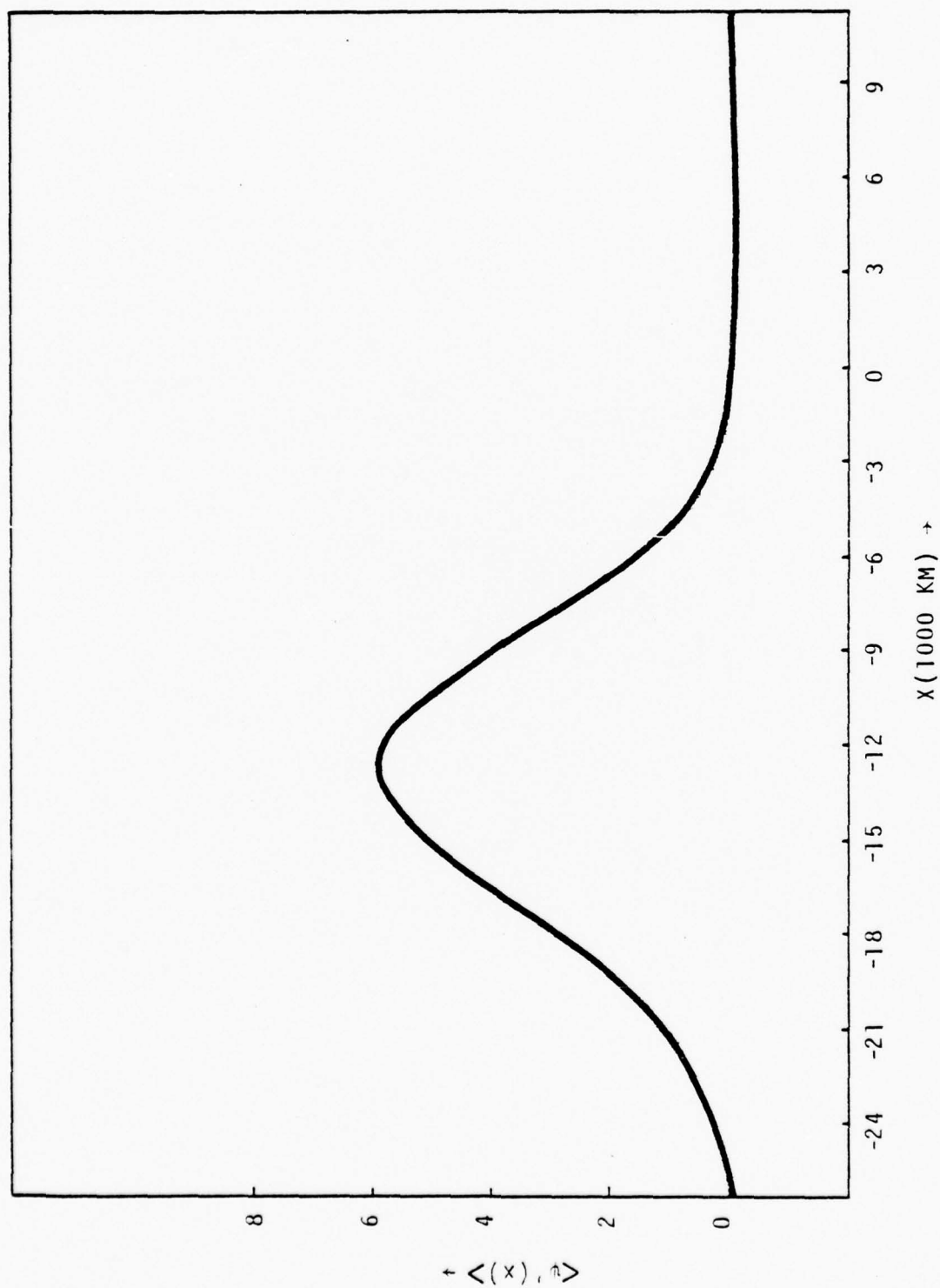
Fig. 11. Experiment I. Wave packet envelope, $\langle \psi'(x) \rangle$ for the complete numerical model.

← $\langle \psi'(x) \rangle$ ←

The ψ' fields for days 83 through 86 are shown in Figs. 12 through 15, respectively, to illustrate a time sequence of the ψ' barotropic wave train. A periodicity of 3.25 days can be determined by examining the time series at each grid point (not shown). We also note from this sequence that there are three maxima of ψ' in the wave structure. One maximum is at y=0 and another is on each wing of the jet near $y = \pm750$ km. The maximum on the wing clearly predominates. Figure 16 shows the variation of wavelength, $L(x)$, for y=0 and $y = \pm750$ km corresponding to the latitudes of the observed three maxima of ψ'. The disturbance wavelength is about 4100 km initially near the inflow boundary. The wavelength near $y = \pm750$ km is larger upstream and smaller downstream of x=0 than at y=0. At $y = \pm750$ km, the maximum wavelength of 5060 km occurs approximately 950 km upstream of x=0 while the minimum wavelength of 3600 km occurs near the outflow boundary. At y=0, the maximum wavelength of 4900 km occurs about 950 km downstream of x=0 while the minimum wavelength of about 4000 km occurs near x = -13,500 km with the wavelength increasing slowly further downstream to the outflow boundary. The range of the wavelength is between approximately 3600 km and 5000 km, which is nearly the same range of values obtained for the most unstable wavelengths using the parallel flow model in Chapter III. Figure 17 shows the disturbance phase speeds, $c_r*(x)$, for latitudes y=0 and $y = \pm750$ km where $c_r*(x)$ is obtained from

50
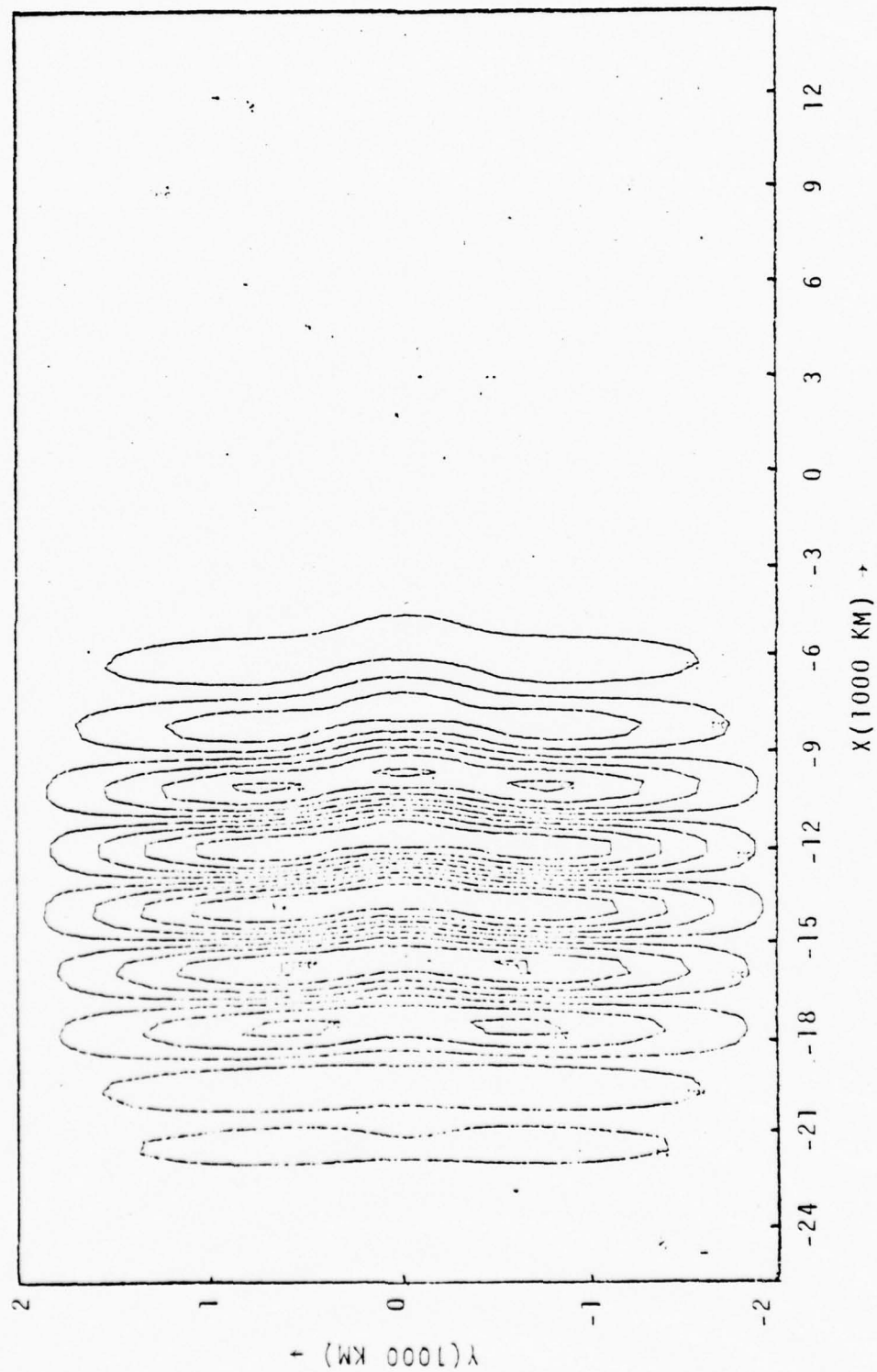
Fig. 12. Experiment I. The ψ' field at t = 83 days.

X(1000 KM) →

Y(1000 KM) →
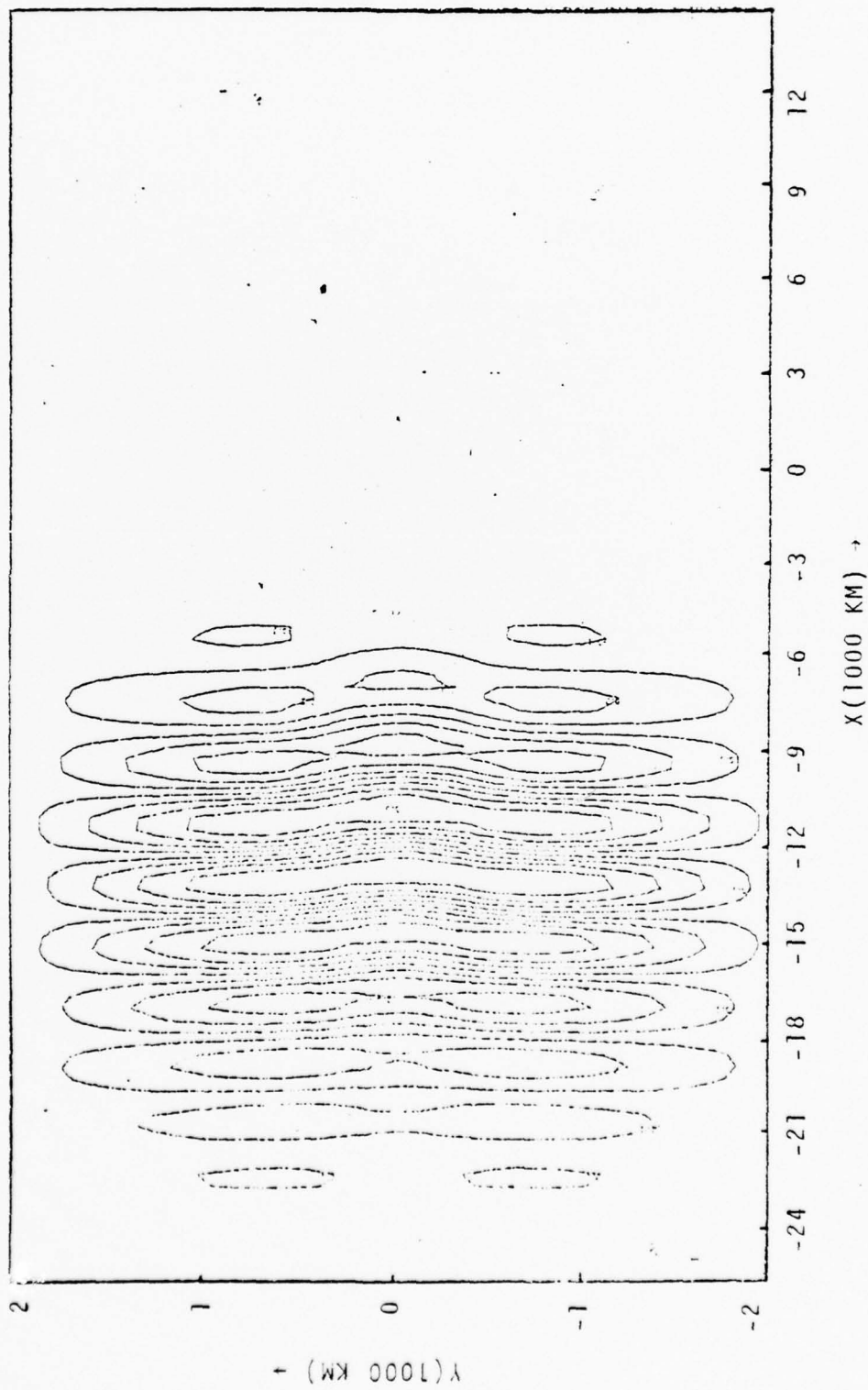
Fig. 13. Experiment I. The ψ' field at t = 84 days'.

X(1000 KM) →

Y(1000 KM) →
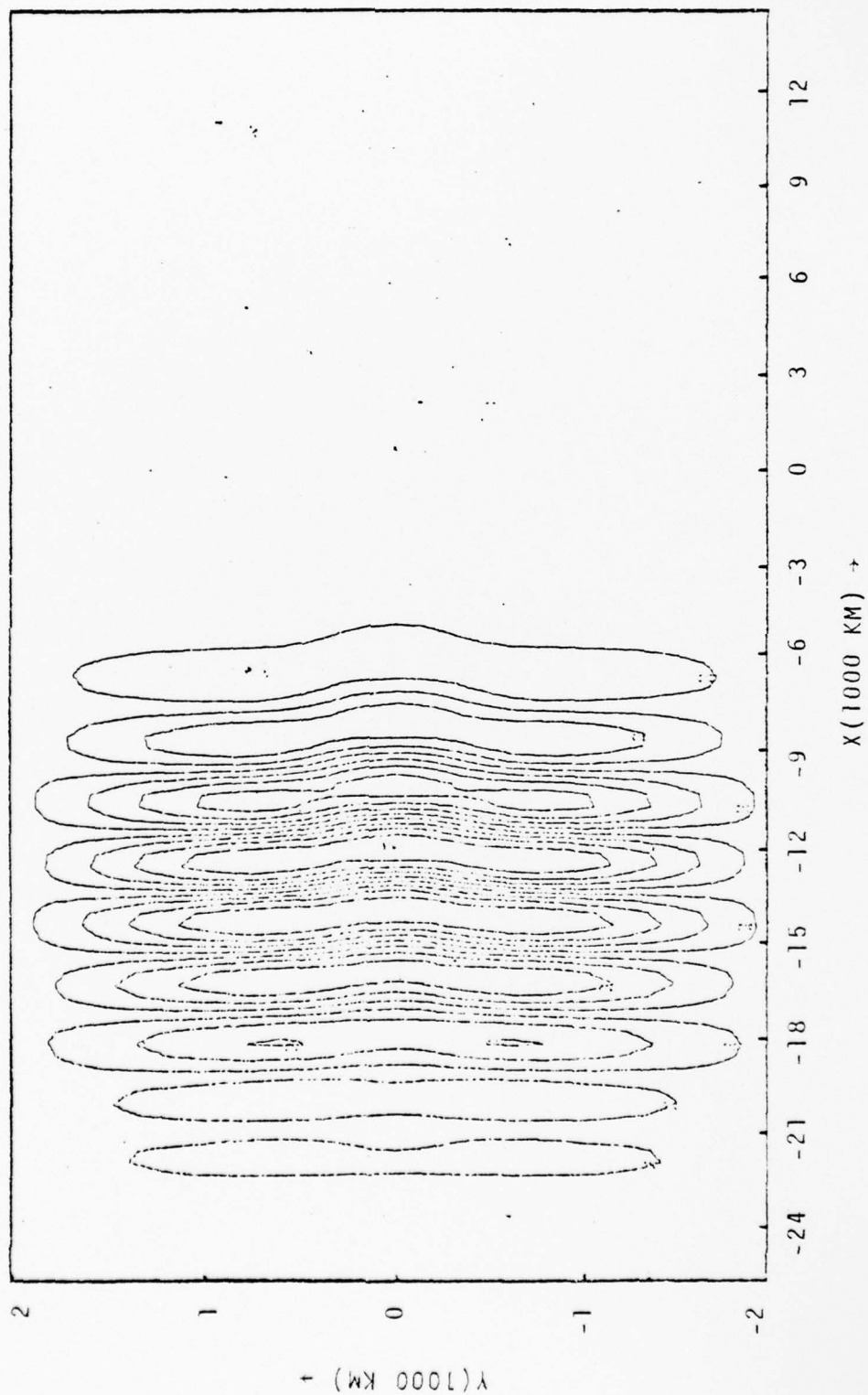
Fig. 14. Experiment I. The ψ' field at t = 85 days.

53

X(1000 KM) →
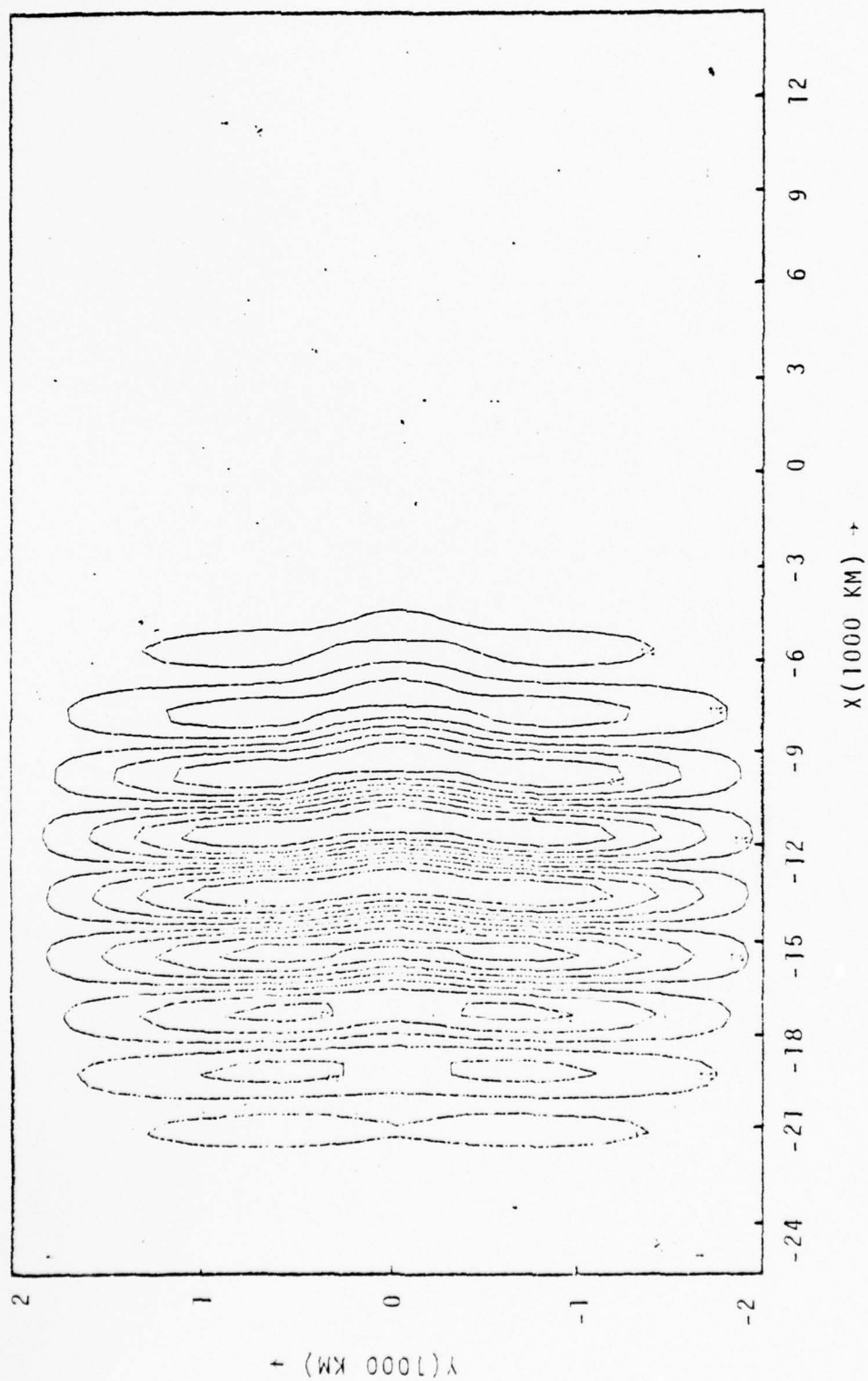
Fig. 15. Experiment I. The ψ' field at t = 86 days.

Y(1000 KM) →

54
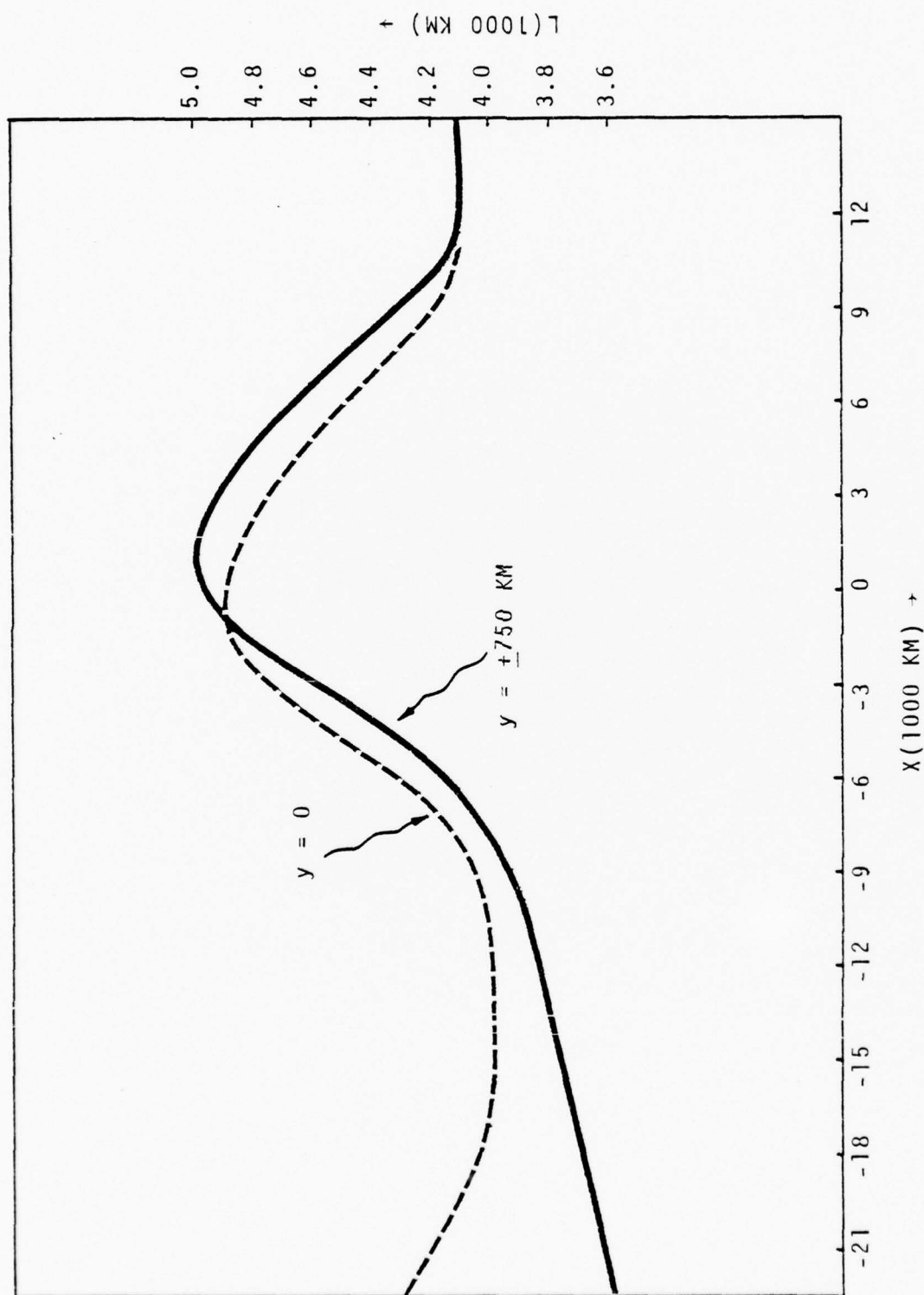
Fig. 16. Experiment I. Wavelengths L(x), from the complete numerical model for latitudes (a) y=0, and (b) y = -750 km.
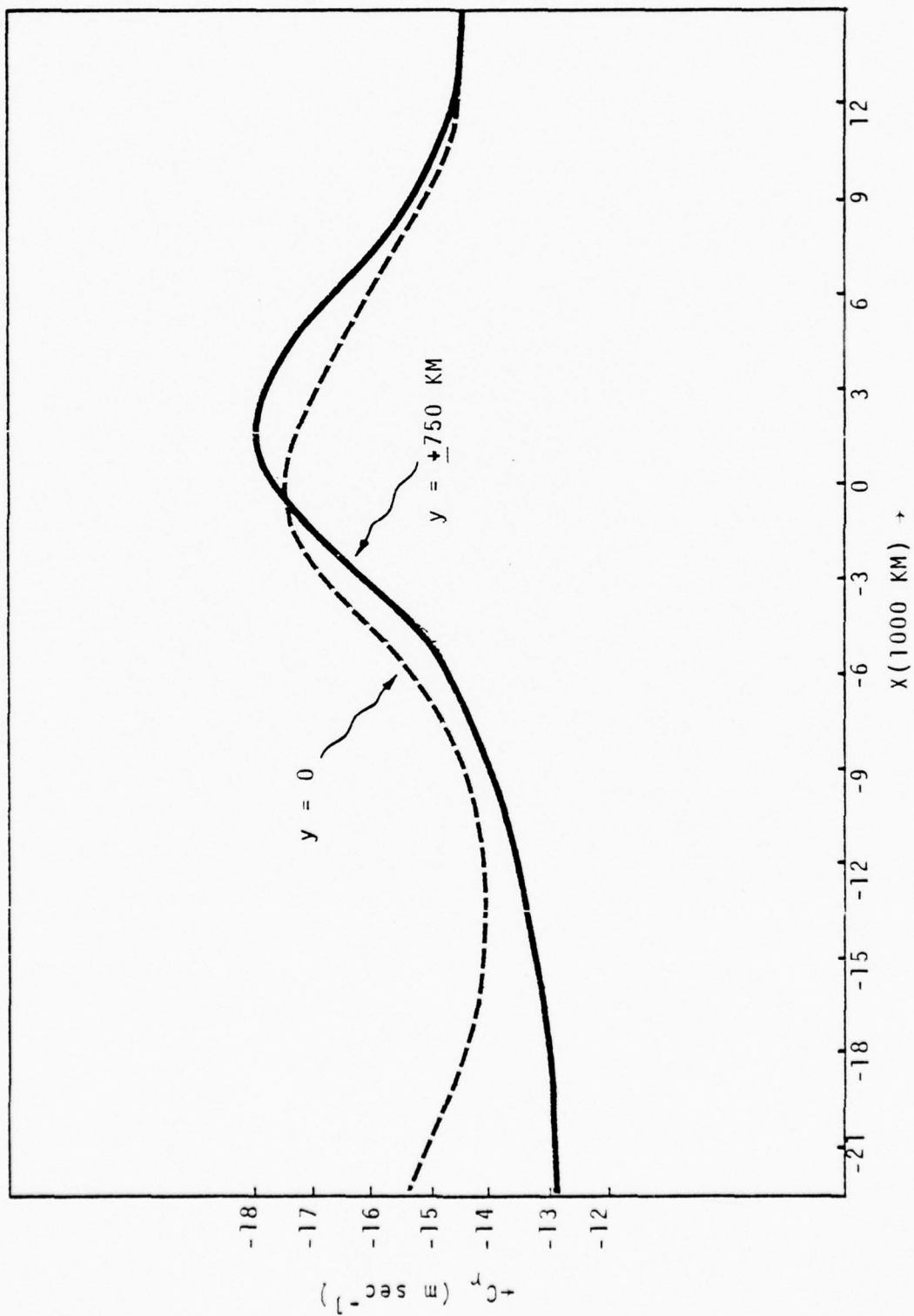
Fig. 17. Experiment I. Phase velocities $c_r{}^*(x)$, from the complete numerical model for latitudes (a) $y = 0$, and (b) $y = -750$ km.

$$c_r^*(x) = \frac{L(x)\omega}{2\pi} \ .$$

(5.2)

Since the entire domain is periodic with the forcing frequency, $c_r^*(x)$ has the same basic behavior as $L(x)$ [Fig. 16] for the corresponding latitudes. Namely, upstream of x=0 the disturbance phase velocity is faster on the wings of the jet than at y=0, and downstream of x=0 it is slower. This behavior of both $L(x)$ and $c_r^*(x)$ illustrates the tilt behavior of the waves as they move into and out of the baro-tropically unstable region of the variable mean wind. More results are presented in the next chapter.

The parallel flow model is also employed to determine a reasonably good forcing function that would generate periodic wave disturbances from the eastern boundary. This is accomplished as follows:

Equation (2.14) defines the analytical form of the periodic forcing which is applied as an inflow boundary condition in the complete numerical model, i.e.,

$$\frac{\partial \psi'}{\partial t} (0,y,t) = A(y)\omega\cos(\omega t) - B(y)\omega\sin(\omega t) \ .$$

Equation (4.17) describes the finite difference approximation to this forcing. The coefficients $A(y)$ and $B(y)$ of (2.14) are obtained from the eigensolution determined using the parallel flow model for the following Bickley jet profile:

$$\bar{u}(y=0) \ = \ -16 \ m \ sec^{-1}$$
$$d \ = \ 962 \ km \ .$$
$$L \ = \ 4,600 \ km$$

57

This profile is representative of the mean flow near the inflow region. Figure 18 shows the y-structure of these coefficients.

Two other forcing functions, which are independently constructed from the parallel flow model, are also tested. These functions are:

$$\frac{\partial \psi'}{\partial t}(0,y,t) = -\omega \cos(\frac{\pi\, y}{D}) \sin(\omega t), \qquad (5.3)$$

and

$$\frac{\partial \psi'}{\partial t}(0,y,t) = -\omega \{\cos(\frac{\pi\, y}{D})\}^{8} \sin(\omega t), \qquad (5.4)$$

where D is the half width of the channel (D = 2000 km).

The behavior of the wave disturbances for all three forcing functions are essentially the same except in the vicinity of the inflow boundary. The parallel flow solutions for the most unstable wavelength show a weak decay rate in the inflow region (see Fig. 8). This is because the linear friction decay rate is slightly larger than the weak local growth rate. We found that this weak decay behavior near the inflow boundary is achieved in the numerical model using forcing function (2.14). Use of the other two forcing functions, (5.3) and (5.4), realizes a weak secondary $<\psi'>_{max}$ near the inflow boundary. Therefore, we found through use of the parallel flow model that the first forcing function provided the better inflow boundary condition than the other two, although no substantial difference occurs even if the other forcing functions are used.
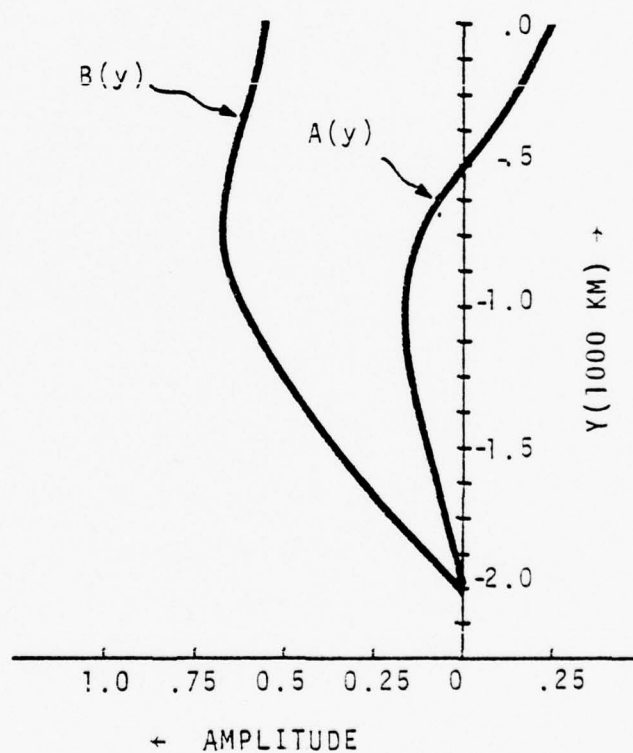
Fig. 18. The coefficients A(y) and B(y) of the eastern boundary forcing function used in the complete numerical model.

B. ENERGETICS

To understand the dynamics of barotropic instability, it is helpful to derive the disturbance kinetic energy equation. A finite difference approximation form of this equation is used to compute the energy budget of the waves. The linearized momentum equations are:

$$\frac{\partial u'}{\partial t} + u'\frac{\partial u'}{\partial x} + u'\frac{\partial \bar{u}}{\partial x} + \bar{v}\frac{\partial u'}{\partial y} + v'\frac{\partial \bar{u}}{\partial y} +$$

$$- \beta y v' = -\frac{1}{\rho}\frac{\partial p'}{\partial x} - D_f u', \qquad (5.5)$$

and

$$\frac{\partial v'}{\partial t} + \bar{u}\frac{\partial v'}{\partial x} + u'\frac{\partial \bar{v}}{\partial x} + \bar{v}\frac{\partial v'}{\partial y} + v'\frac{\partial \bar{v}}{\partial y} +$$

$$\beta y u' = -\frac{1}{\rho}\frac{\partial p'}{\partial y} - D_f v'. \qquad (5.6)$$

After multiplying (5.5) by u' and (5.6) by v' and adding the resultant equations, we obtain the disturbance kinetic energy equation:

$$\frac{\partial k'}{\partial t} + \bar{u}\frac{\partial k'}{\partial x} + \bar{v}\frac{\partial k'}{\partial y} = -u'^2\frac{\partial \bar{u}}{\partial x} - u'v'\frac{\partial \bar{u}}{\partial y} - u'v'\frac{\partial \bar{v}}{\partial x} +$$

$$- v'^2\frac{\partial \bar{v}}{\partial y} - \frac{1}{\rho}\frac{\partial(u'p')}{\partial x} - \frac{1}{\rho}\frac{\partial(v'p')}{\partial y} - 2D_f k', \qquad (5.7)$$

where

$$k' \equiv \frac{u'^2}{2} + \frac{v'^2}{2} . \qquad (5.8)$$

The disturbance fields are considered to have a time dependence of the form $\sin[\omega \bar{t} + \theta(x,y)]$. Thus, when (5.7) is averaged over one period and over one latitudinal domain ($-D \leq y \leq D$), the following energy balance equation is obtained:

60

$$\left\langle \underset{1}{-\bar{u}\frac{\partial k'}{\partial x}} - \underset{2}{u'^2\frac{\partial \bar{u}}{\partial x}} - \underset{3}{u'v'\frac{\partial \bar{u}}{\partial y}} - \underset{4}{u'v'\frac{\partial v}{\partial x}} - \underset{5}{v'^2\frac{\partial \bar{v}}{\partial y}} + \right.$$

$$\left. \underset{6}{-\frac{1}{\rho}\frac{\partial(u'p')}{\partial x}} - \underset{7}{2D_f k'} \right\rangle = 0.$$

(5.9)

Term 1 is the advection of k' by the mean flow ($\bar{u}$). Terms 2, 3, 4 and 5 are the barotropic exchange terms with the mean flow. Term 6 represents the work done by the pressure field. Term 7 is the dissipation term and represents an energy sink. With the exception of term 6, all the terms in (5.9) are determinable from the $\bar{\psi}$ and ψ' fields. Thus, the pressure work term is determined as a residual in Eq. (5.9). The energy equation is evaluated after the complete numerical model achieves the fully periodic state.

Figure 19 shows the energy balance as function of longitude. Clearly, the maximum value of each of the terms in the energy equation occurs downstream of $x=0$. Curve (a) represents the Reynold's stress term, $\langle(-u'v'\partial\bar{u}/\partial y)\rangle$, where the maximum value occurs approximately at $x = -10,975$ km. Curve (b) represents the advection term, $\langle(-\bar{u}\partial k'/\partial x)\rangle$, of k' by the zonal current. Curve (c) represents the linear dissipation term $\langle(2D_f k')\rangle$. We observe that the largest dissipation takes place near the maximum amplitude of the wave packet envelope, $\langle\psi'(x)\rangle_{max}$. Curve (d) represents the pressure work term, $\left\langle\left(\frac{1}{\rho}\frac{\partial(u'p')}{\partial x}\right)\right\rangle$. It also has a maximum near $\langle\psi'(x)\rangle_{max}$. The remaining barotropic terms are not

61
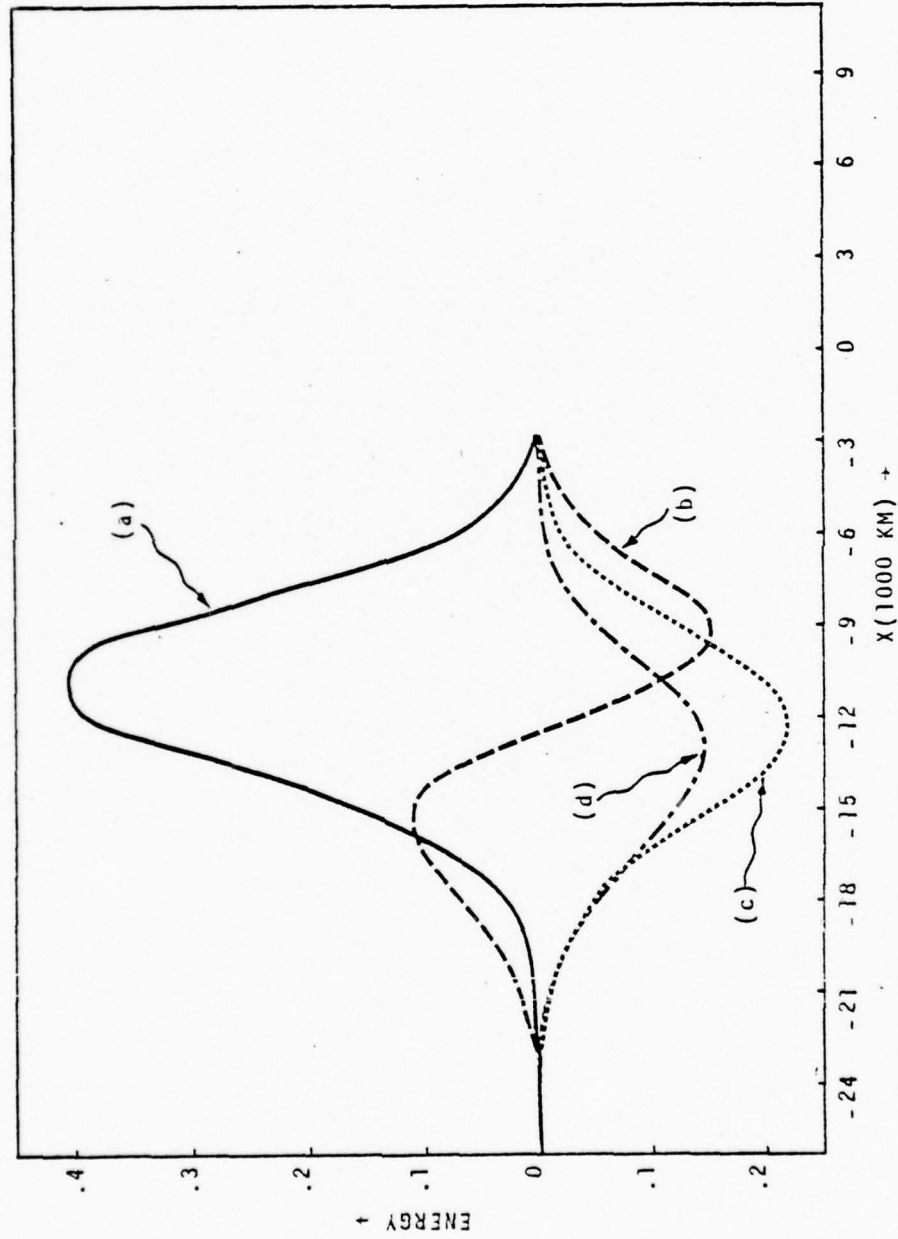
Fig. 19. Experiment I. Disturbance energy balance as a function of longitude x: (a) Reynold's stress term $\langle(u'v'\partial\bar{u}/\partial y)\rangle$; (b) energy transport term, $\langle(-\bar{u}\partial k'/\partial x)\rangle$; (c) dissipation term $\langle(2D_f k')\rangle$; and (d) pressure work term $\langle(\frac{1}{\bar{\rho}}\frac{\partial}{\partial x}(u'p')\rangle$.

included in Fig. 18 because they are 2 to 3 orders of
magnitude smaller than $<(-u'v'\partial\bar{u}/\partial y)>$.

Recall that for Experiment I, $<\psi'(x)>_{max}$ occurs approxi-
mately at x = -12,750 km. We observe that the advection of
k' by $\bar{u}$ plays a dominant role in the energy balance. Once
the fully periodic state is achieved, the generation of
disturbance energy by barotropic instability essentially
occurs in the region between the $<\psi'>_{max}$ (x = -12750 km) and
the jet maximum (x=0). It is in this region that the
strongest positive correlations occur between u'v' and
$-\partial\bar{u}/\partial y$ in the Reynold's term. This is consistent with the
observed behavior of the waves (see Figs. 10 and 11) since
this strong correlation of u'v' is dependent on maximum
amplitude of ψ' squarred and the maximum tilt of the wave
structure with the shear of the mean flow $-\partial\bar{u}/\partial y$. It is
also from this source region that $\bar{u}$ transports a large part
of this generated k' downstream to a point centered near
x = -15,000 km.

Strongest dissipation of k' occurs in the region centered
near $<\psi'(x)>_{max}$. It is in this region that the strongest
spatial gradients of ψ' occur. The largest values of pressure
work also occur in this region where the pressure work term
is computed as a residual. We note that its location of
occurrence is consistent with the large amplitudes and spatial
gradients of ψ' of the region. We also note that $<(-\bar{u}\partial k'/\partial x)>$

63

vanishes at $\langle\psi'(x)\rangle_{max}$ since k' is maximum at this longitude. The disturbance energy balance which is shown in Fig. 19 graphically illustrates the basic energetics involved in supporting the large amplitudes and spatial gradients of ψ' a considerable distance downstream of the jet maximum. Clearly, the Reynold's stress term, $\langle(u'v'\partial\bar{u}/\partial y)\rangle$, is the only dominant source for disturbance kinetic energy.

VI. SIMPLE MECHANISTIC ANALYTICAL MODEL

A. FORMULATION

In this chapter we develop a simple mechanistic analyti-
cal model which uses the locally determined parallel flow
solutions. The results of this simple model can be compared
with those of the complete numerical model to obtain some
measure of the adjustment of the transient barotropic waves
to the local stability of the variable mean wind.

The following equation allows for propagation and growth
or decay:

$$\frac{\partial \psi'}{\partial t} + c_r(x) \frac{\partial \psi'}{\partial x} = n(x)\psi' , \qquad (6.1)$$

where ψ' represents the disturbance streamfunction. $c_r(x)$
is the local phase velocity and $n(x)$ is the local growth rate.
We observe that if c_r and n are independent of x, then
Eq. (6.1) is exact, and, in general, should give a reasonable
approximation to the downstream variation of ψ'.

Let us consider the case where ψ' has a solution of the
form:

$$\psi' = F'(x)e^{iwt}, \qquad (6.2)$$

where ω is a specified frequency. After substituting (6.2)
into (6.1), we obtain

$$i\omega F' + c_r(x) \frac{dF'}{dx} = n(x)F'. \qquad (6.3)$$

Rearranging (6.3), we get

$$\frac{1}{F'} \frac{dF'}{dx} = \frac{n(x) - i\omega}{c_r(x)} ,$$ (6.4)

which has a solution of the form of

$$\ell n \left[\frac{F'}{F'_0}\right] = \int_{x_0}^{x} \frac{n(x) - i\omega}{c_r(x)} dx, \quad \text{or}$$ (6.5)

(6.6)

$$F'(x) = F'_0 \exp\left\{-i \int_{x_0}^{x} \frac{\omega}{c_r(x)} dx\right\} \exp\left\{\int_{x_0}^{x} \frac{n(x)}{c_r(x)} dx\right\} .$$

Some fundamental insight can be gleaned from (6.6). Here the amplitude of ψ' must be specified at some initial point, x_0, which could be the inflow point. The local wavenumber is ω/c_r and the spatial growth rate is n/c_r. These are the real and imaginary parts of the wavenumber, if we were to write $\psi' = A \exp(ikx - i\omega t)$.

In this simple analytical model, we are interested in the growth and decay of the wave packet. If the oscillatory behavior of Eq. (6.6) is dropped, the following equation expresses the envelope of the wave packet:

$$F(x) = F'_0 \exp\left\{\int_{x_0}^{x} \frac{n(x)}{c_r(x)} dx\right\} .$$ (6.7

Equation (6.7) gives the exponential growth/decay behavior of a wave disturbance as it travels within its wave packet envelope. This behavior is determined by the integral effects of the local stability properties of the mean flow.

66

B.   APPLICATIONS

Figure 20 compares the envelope for $\psi'(x)$ from the complete numerical solution (Fig. 11) with the $F(x)$ given by Eq. (6.7) for two values of x_0. In this figure the amplitude is plotted against upstream distance from the initial point x_0. The analytical model uses the locally determined parallel flow growth rates (n) and phase speeds (c_r) based on the wavelengths measured from the complete numerical solutions. Therefore, Eq. (6.7) is applied at latitude $y = \pm 750$ km where the wavelengths are measured. The curve for $F(x)$ can be shifted up or down by changing x_0, but its shape does not change. In Figure 20 all the curves have a maximum amplitude at $x = -12,750$ km where the local growth rate is zero; however, the simple model has a lower maximum growth rate and slower damping rates than the complete numerical model.

The lower portion of Fig. 21 contains the wavelength measured from the numerical solution at $y = -750$ km. In the upper portion of the diagram are the phase velocities, c_r from the parallel flow model and $c_r{}^*$ from the complete numerical model for the same latitude. Here c_r is computed with the use of the wavelength shown. The two phase speeds have similar behavior although $c_r{}^*$ is shifted slightly upstream and has larger variations. We also note that $c_r{}^*$ is generally smaller than c_r except for the region -1500 km $< x < 6750$ km.
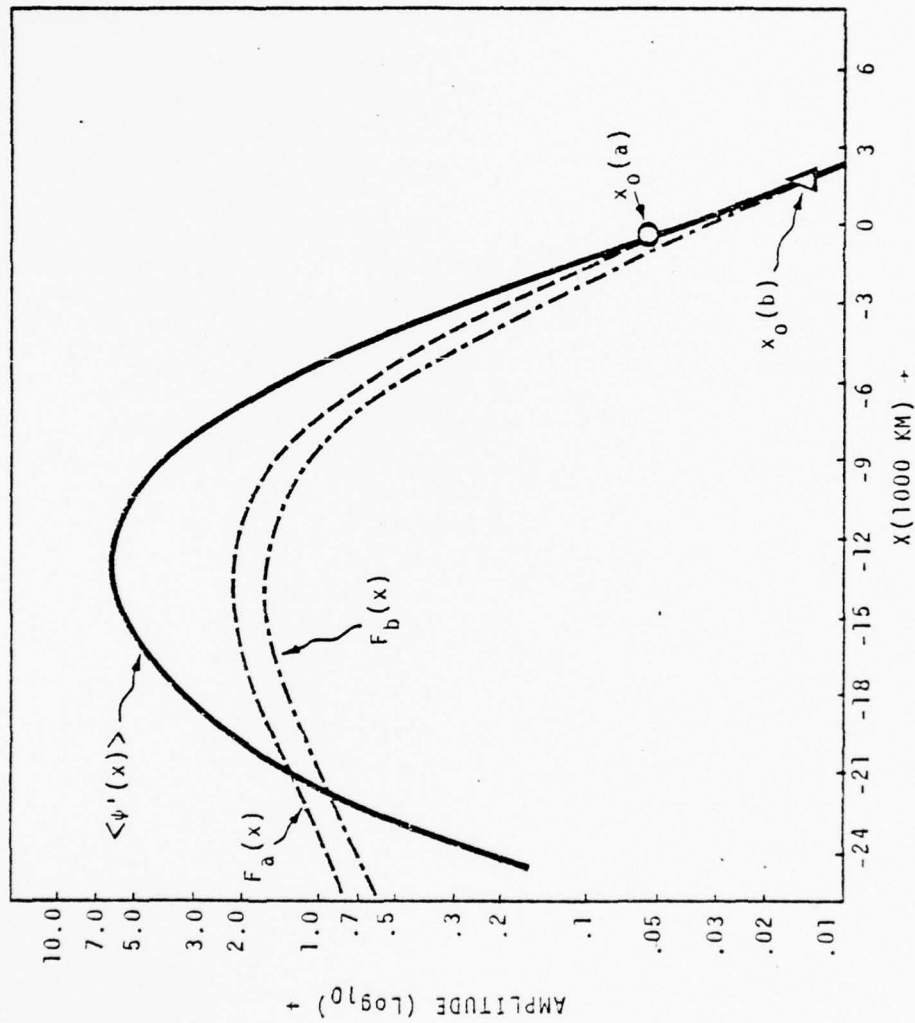
Fig. 20. Experiment 1. The wave packet envelopes. $F_a(x)$ is from the analytical model for initial point (a) $x_0 = 375$ km, $F_b(x)$ is from the analytical model for initial point (b) $x_0 = 1875$ km, and $\langle \psi'(x) \rangle$ is from the complete numerical model.

LATITUDE: y = ±750 KM

$c_r^{\star}(x)$

$c_r(x)$

$L(x)$

X(1000 KM) →

$-c_r$ (m sec^{-1})
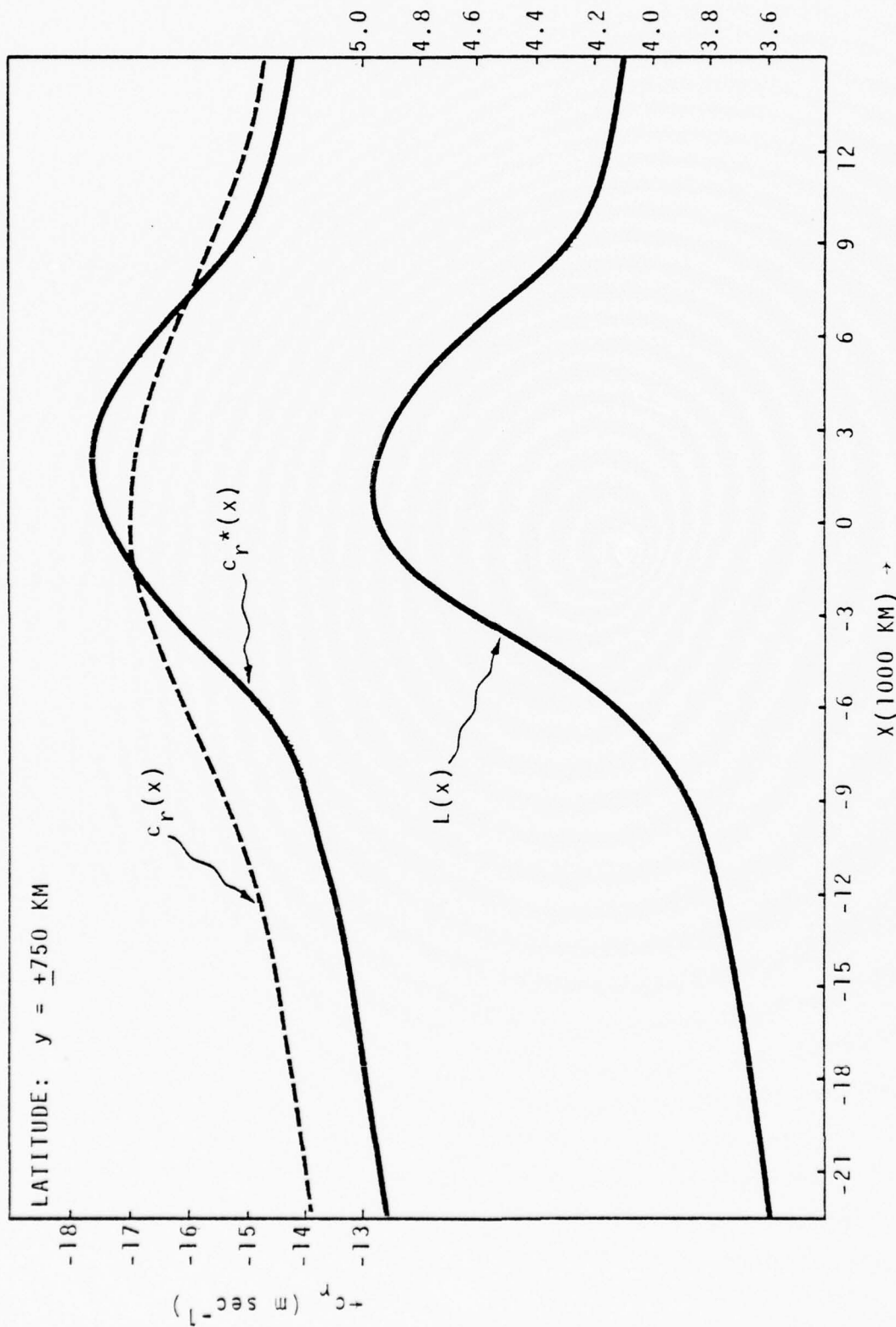
Fig. 21. Experiment I. Latitude y = -750 km (a) Phase velocities, $c_r(x)$ from parallel flow model, and $c_r^{\star}(x)$ from complete numerical model. (b) Wavelength $L(x)$.

Similarly, Fig. 22 contains the wavelengths and phase speeds for latitude y=0. Again, the two phase speeds have similar behavior, but at this latitude c_r* is shifted slightly downstream and the differences between phase speeds is generally less than at y = -750 km. Again we note that c_r* is generally smaller than c_r except for the region: -2250 km $\leq$ x $\leq$ 2250 km. This indicates that both the wavelength L(x) and the phase velocity $c_r*(x)$ between latitudes y=0 and y = -750 km are maximum where the mean flow is strongest.

Figure 23 contains the spatial growth rates, m and m*, from the parallel flow model and from the complete numerical model, respectively. For the parallel flow model, we obtain

$$m = - n/c_r .$$ (6.8)

The value of m* is computed directly from the envelope. We note in Fig. 23 that m* has a larger maximum than m and the maximum is shifted slightly downstream from the jet maximum. Both curves pass through 0 at x = -12,750 km which is the maximum for both wave packet envelopes.   However, m* shows a much larger damping in the outflow region which can also be seen in Fig. 20. In fact the parallel flow solution damps at the rate given by the frictional coefficient divided by the phase speed. This is expected in the baro-tropically stable outflow region when using the parallel flow model because this model can only give the eigen-solution of the most unstable discrete mode.
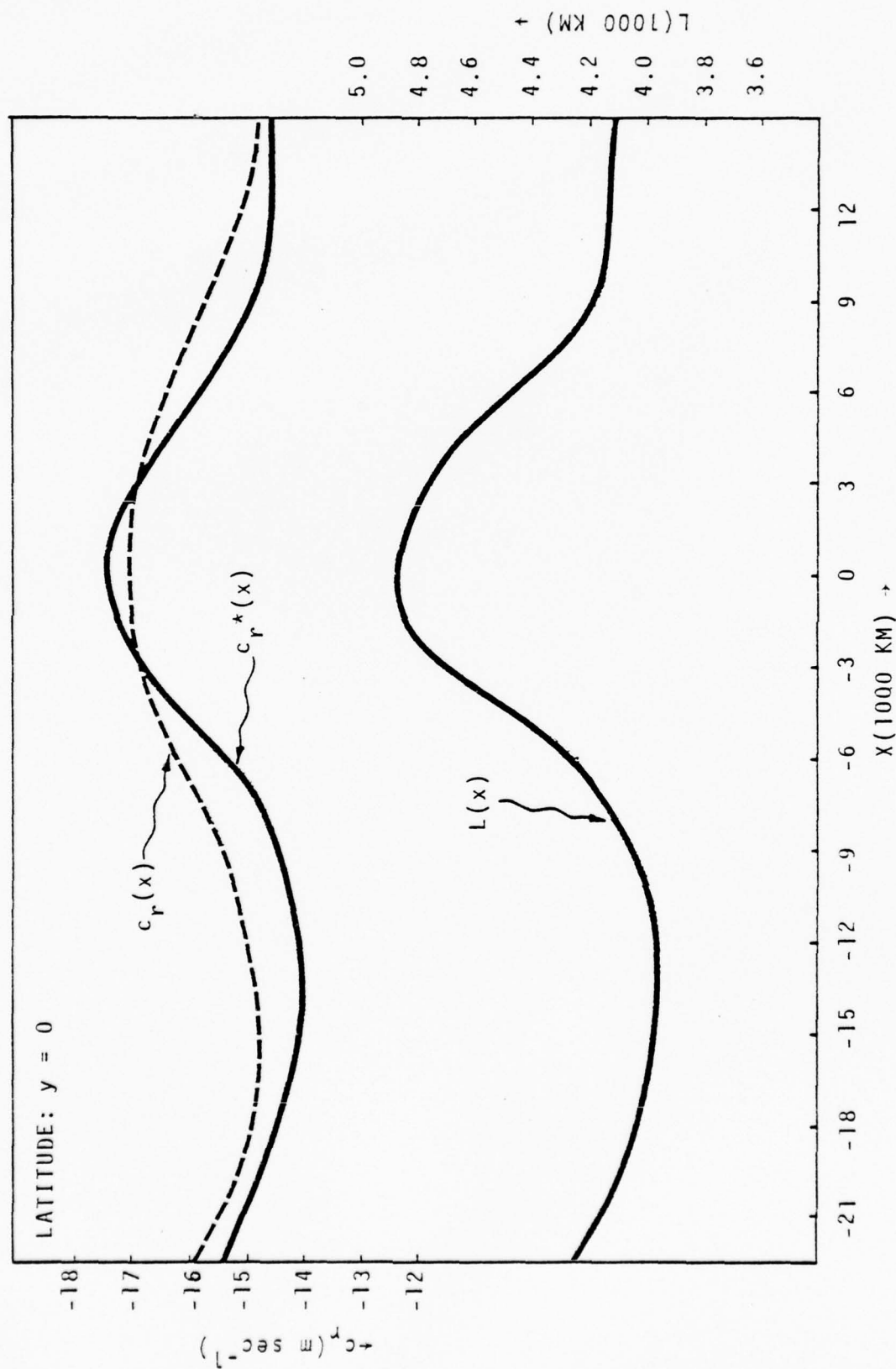
Fig. 22. Experiment I. Latitude y = 0. (a) phase velocities, $c_r(x)$ from parallel flow model, and $c_r^*(x)$ from complete numerical model. (b) Wavelength L(x).
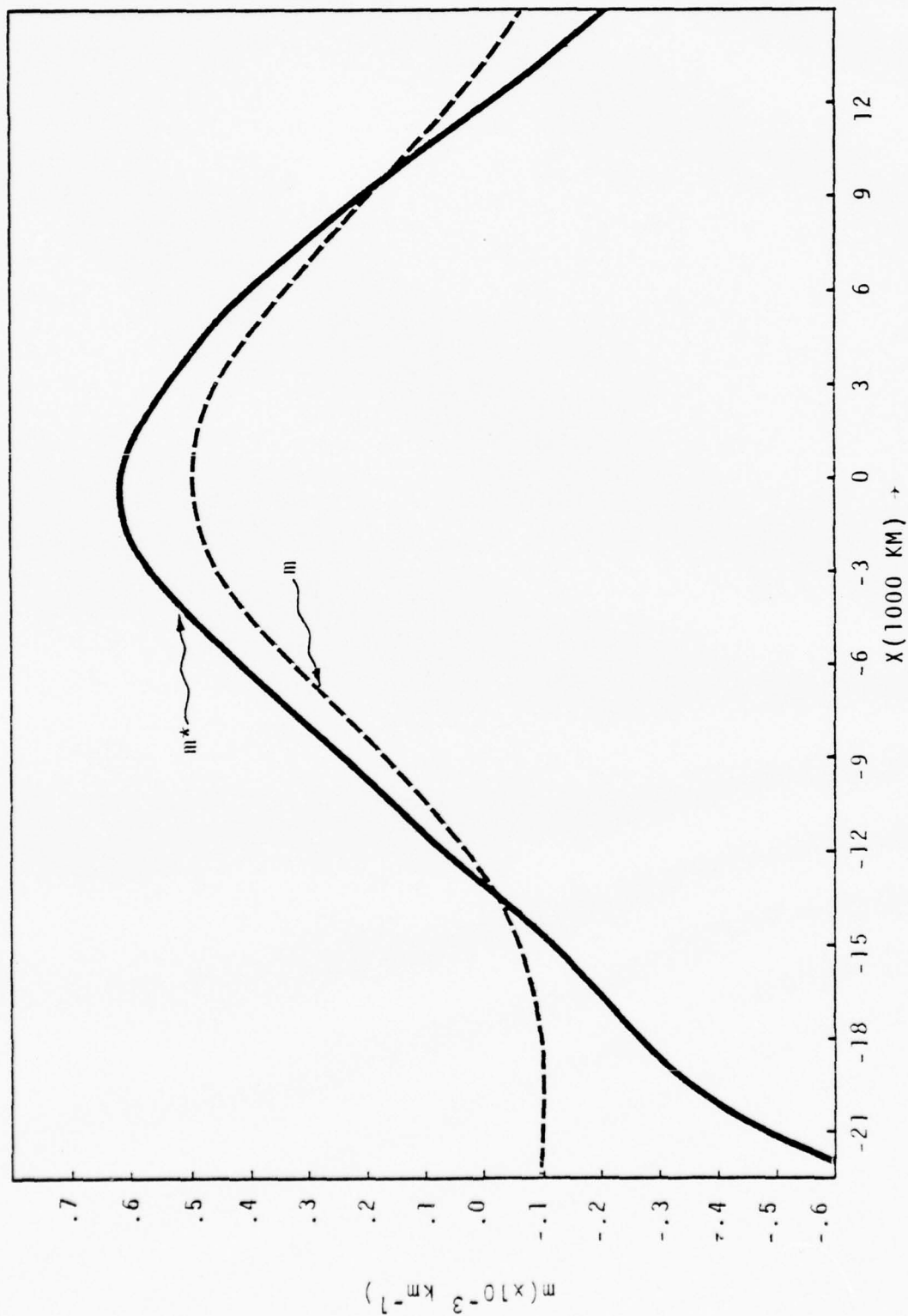
Fig. 23. Experiment I. Spatial growth rates, $m(x)$ from the parallel flow model, and $m^*(x)$ from the complete numerical model.

The solutions observed in the numerical model (see
Fig. 10) toward the outflow boundary tilt in the same sense
as the mean wind shear which gives dynamic damping. This
tilt behavior is also indicated by the divergence of phase
speed in the outflow region between $y=0$ and $y = -750$ km
(see Figs. 21 and 22). This dynamic damping appears to
be due to continuous spectrum solutions (Case, 1960; Yanai
and Nitta, 1968) which are not included in the normal mode
solutions that are employed in the simple integral
[Eq. (6.6)]. In fact we observe that, in the outflow region,
the dynamic damping is $1/t$ or faster, increasing near the
outflow boundary. In Fig. 23 the $m*$ curve is skewed slightly
to the left with respect to m and the jet maximum. This
could be the result of the tilt structure in the wave lagging
spatially behind the expected value from the local stability
conditions. This would give a smaller growth rate on the
upwind side of the jet maximum and a larger growth rate on
the downwind side. This effect is indicated by the asymmetry
of the $m*$ curve with respect to the m curve in the unstable
region of the mean wind. However, this is not the only effect
involved because the most striking feature of Fig. 23 is
the fact that the maximum value of $m*$ is significantly
larger than the maximum value of m. We have already shown
that the most important disturbance energy production term
(see Fig. 18) in the energy computations with the numerical
solutions is proportional to

73

$$<(-u'v'\partial\bar{u}/\partial y)> \;.$$

This term is the only source term for the parallel flow model, and it depends on the phase tilt in the disturbance field. Figure 24 compares the phase tilt of the numerical model solution, θ^*, and that of the most unstable wavelength of the parallel flow model, θ_0, at $x = 0$, $x = 3750$ km, and $x = 13125$ km. It is evident that at the jet maximum the tilt from the numerical model is significantly larger than for the tilt from the parallel flow model. This is also evident but to a lesser degree at $x = 3750$ km. These results are consistent with the larger growth rates for the variable jet flow. This stronger tilt is also indicated by the comparison of the c_r^* and c_r curves in the region near and slightly upstream of the jet maximum for latitudes $y=0$ and $y = -750$ km (see Figs. 21 and 22). We note that at $y = -750$ km, c_r^* is relatively larger than c_r near the jet maximum. This difference is significantly reduced and shifted slightly downstream at $y=0$. We also note that near the inflow region ($x = 13125$ km), the phase tilt of the numerical solution lags slightly behind the parallel flow solution (see Fig. 24c). Apparently the downstream variation of $\bar{u}$ augments the phase tilt which gives a larger growth rate.

In comparing the parallel flow theory and the complete numerical model, a source of error could be introduced

74
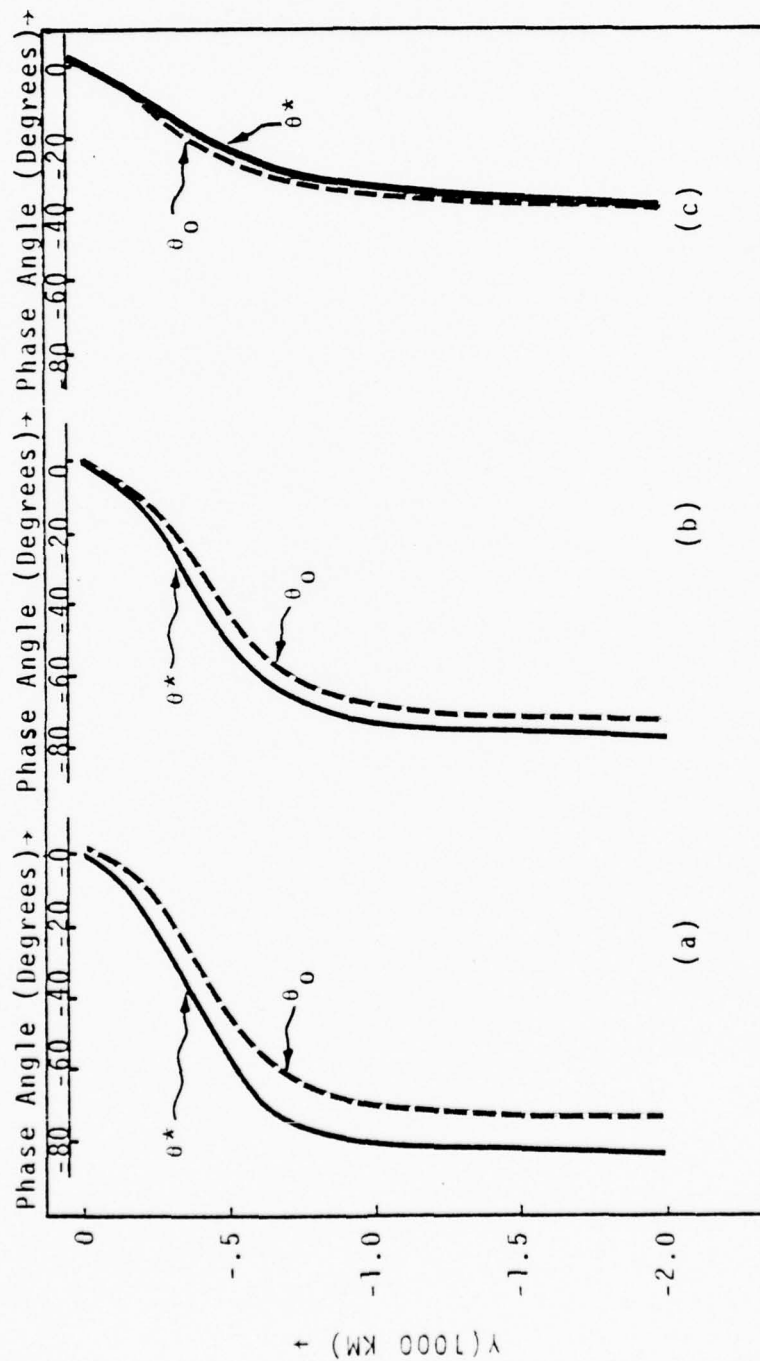
Fig. 24. Experiment I. Comparison of phase tilt of the complete numerical model, θ^*, and of the most unstable wavelength of the parallel flow model, θ_0, for longitudes (a) $x = 0$, (b) $x = 3750$ km, and (c) $x = 13125$ km.

75

through the zonal resolution. This is because in the former
the zonal variation is specified by a spectral representa-
tion, while in the latter it is resolved by finite differences.
Since the wavelength appearing in the complete numerical model
varies between 10 and 13.5 Δx, such resolution normally gives
a good approximation to the exact solution (Haltiner, 1971).
Thus, this error should not be very significant. In order to
confirm this we carried out an experiment in which a parallel
mean flow is specified by the full two-dimensional model
finite differences of the complete numerical model. The
growth rate and phase speed calculated from the experiment
agree very well with those obtained by the semi-spectral
parallel flow model, the difference being only 1-2%. Thus
we may conclude that the differences between the numerical
solution and the local solution of the parallel flow theory
are genuine and are not due to the differences in the model
resolution.

C.   EFFECTS OF LINEAR FRICTION

Figure 23 shows that the local growth rate, determined
by the parallel flow model, changes sign at x = -12,750 km
and that it approaches the linear friction decay rate near
the outflow region. We also note that the maximum aplitude
of both the analytical and numerical model wave packet
envelopes occurs at the lontitude where $n(x)$ vanishes.
Based on these results, $\langle \psi' \rangle_{max}$ is expected not only to

decrease in magnitude but to occur further upstream if the linear frictional rate is increased. Likewise, the opposite effect would be expected if this friction were decreased. This hypothesis is tested by rerunning Experiment I using a larger friction of $D_f = .25 \times 10^{-5}$ sec^{-1} which is equivalent to e-folding decay time of 4.63 days. We found that $\langle \psi' \rangle_{max}$ occurred approximately 1700 km further upstream and with an amplitude of an order of magnitude smaller (.4 vice 5.9) than for the original experiment.

VII. EXPERIMENT II

In Experiment II a constant advective speed of
$U_0 = -5$ m sec^{-1} is added to the mean flow, otherwise the
parameters are the same as those used in Experiment I. We
hope this modification will shed some light on the adjustment
process of a faster moving wave chain. As in Experiment I,
the analytical model also uses locally determined parallel
flow growth rate (n) and the phase speed (c) based on the
wavelength measured from the complete numerical solution.
The local phase speed c is now related to the Doppler-
shifted phase speed $\hat{c}$ by $\hat{c} = c + U_0$. The maximum ψ' response
in this experiment is obtained with a forcing period of 2.5
days. Since the Doppler-shifted frequency may be written
as $\hat{\omega} = k(c* - U_0) = \omega - kU_0$, this shorter period actually
gives approximately the same Doppler-shifted frequency as
that of Experiment I (where the period is 3.25 days with
$U_0 = 0$). Figure 25 shows the ψ' field for day 70.

Based on the results of the simple analytical model
[Eq. (6.8)], we expect that the constant advective velocity
U_0 will significantly reduce the local spatial growth rate

$$m = - \frac{n}{\hat{c}+U_0} \qquad (7.1)$$

Figure 26 shows the spatial growth rates from the parallel
flow model (m) and from the complete numerical model (m*).
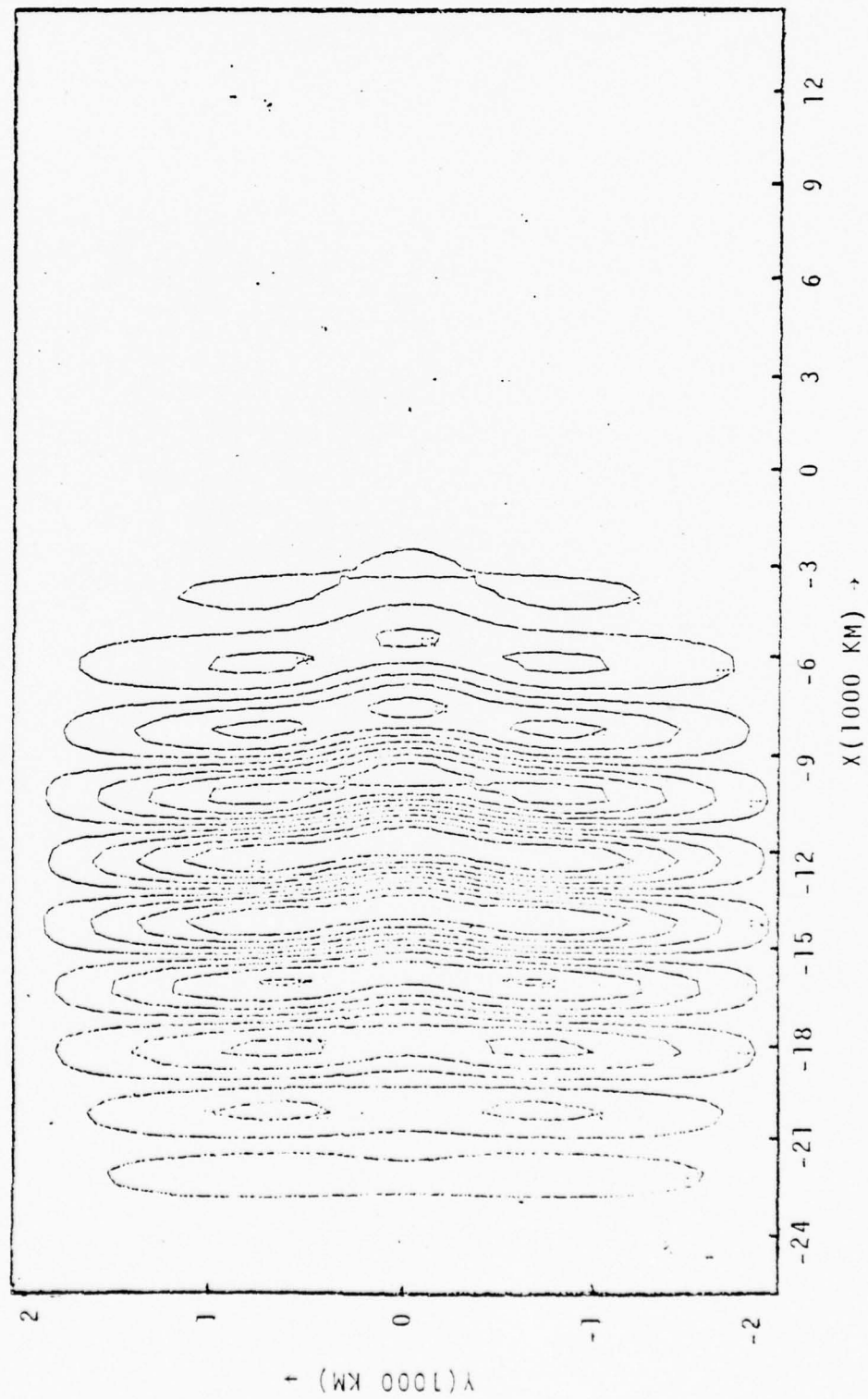
Fig. 25. Experiment II. The ψ' field at t = 70 days.

X(1000 KM) →

Y(1000 KM) →
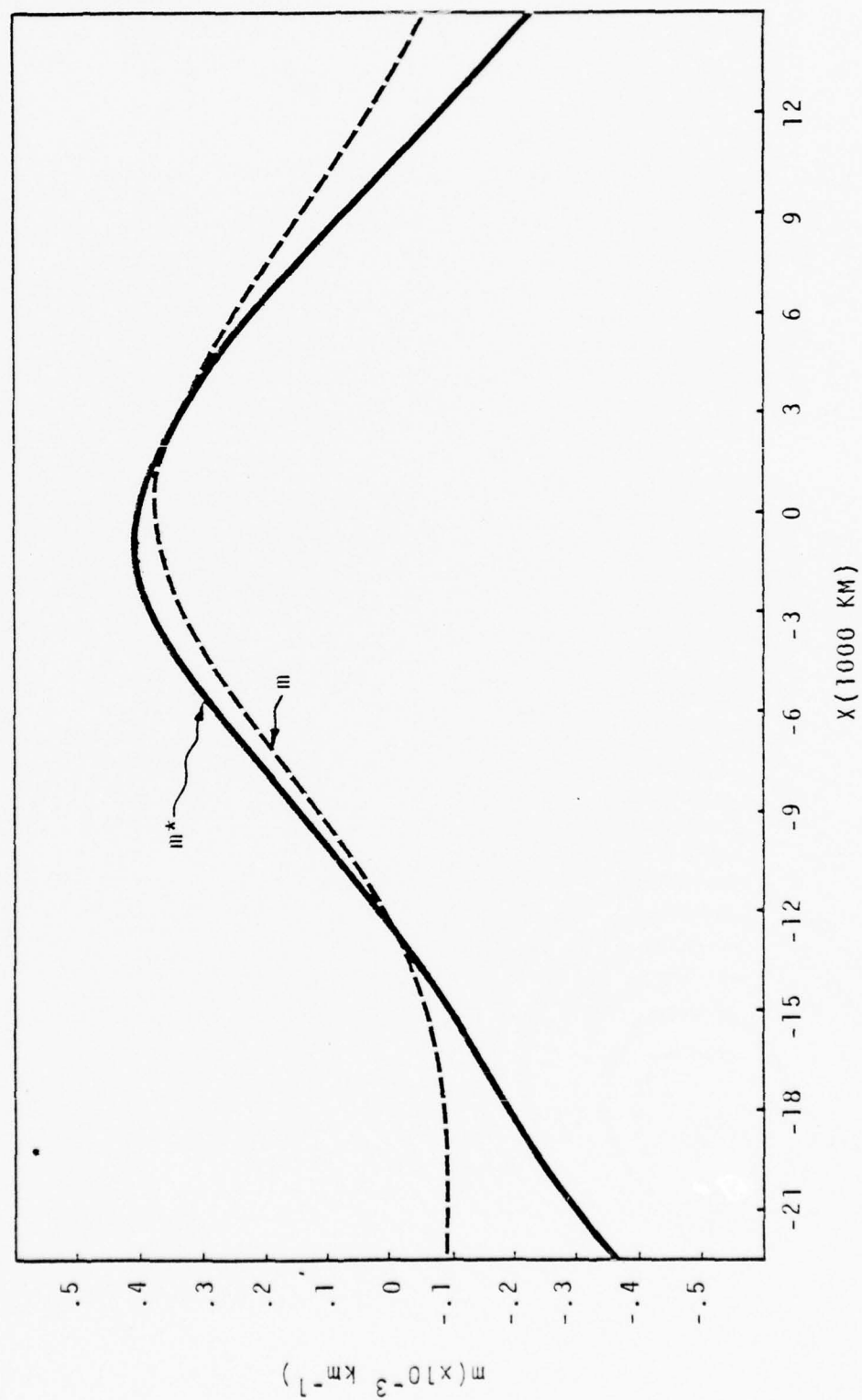
Fig. 26. Experiment II. Spatial growth rates, m(x) from the parallel flow model, and m*(x) from the complete numerical model.

Comparing this figure with Fig. 23, the reduction in both m
and m* from those of Experiment I is clear. This reduction
is evidently due to the advective velocity which causes the
disturbances of Experiment II to move approximately
-5 m sec^{-1} faster than in Experiment I. Thus, the waves
have less time to grow or damp in response to the local
stability per unit distance traveled. The smaller spatial
growth rate obviously affects the amplitude and spatial
gradients of ψ'. Figure 27 shows the wave packet envelope
$<\psi'(x)>$ of the complete numerical solution for Experiment II.
Figure 28 shows this envelope along with the analytical model
envelope $F(x)$ using either x_o = -375 km or x_o = 3750 km as
the initial point (no discernible difference is noted between
the use of these initial points). Both envelopes are, as
expected, significantly smaller than those of Experiment I.
In addition, there is less variation in the wavelength
(3750 km $\leq$ x $\leq$ 4875 km) compared to Experiment I. This is
also a result of the faster phase speed which causes the waves
to have less time to adjust to the local $\bar{u}(x,y)$.

Although the faster phase speed of the waves in
Experiment II reduces the magnitude of growth and decay rates
and therefore brings the spatial growth rate curves of the
numerical model (m*) closer to that of the parallel flow
model (m), we notice a stronger asymmetry in the m* curve
with respect to x=0 in Fig. 26 compared to Experiment I
(see Fig. 23). In addition to the maximum m* occurring

81
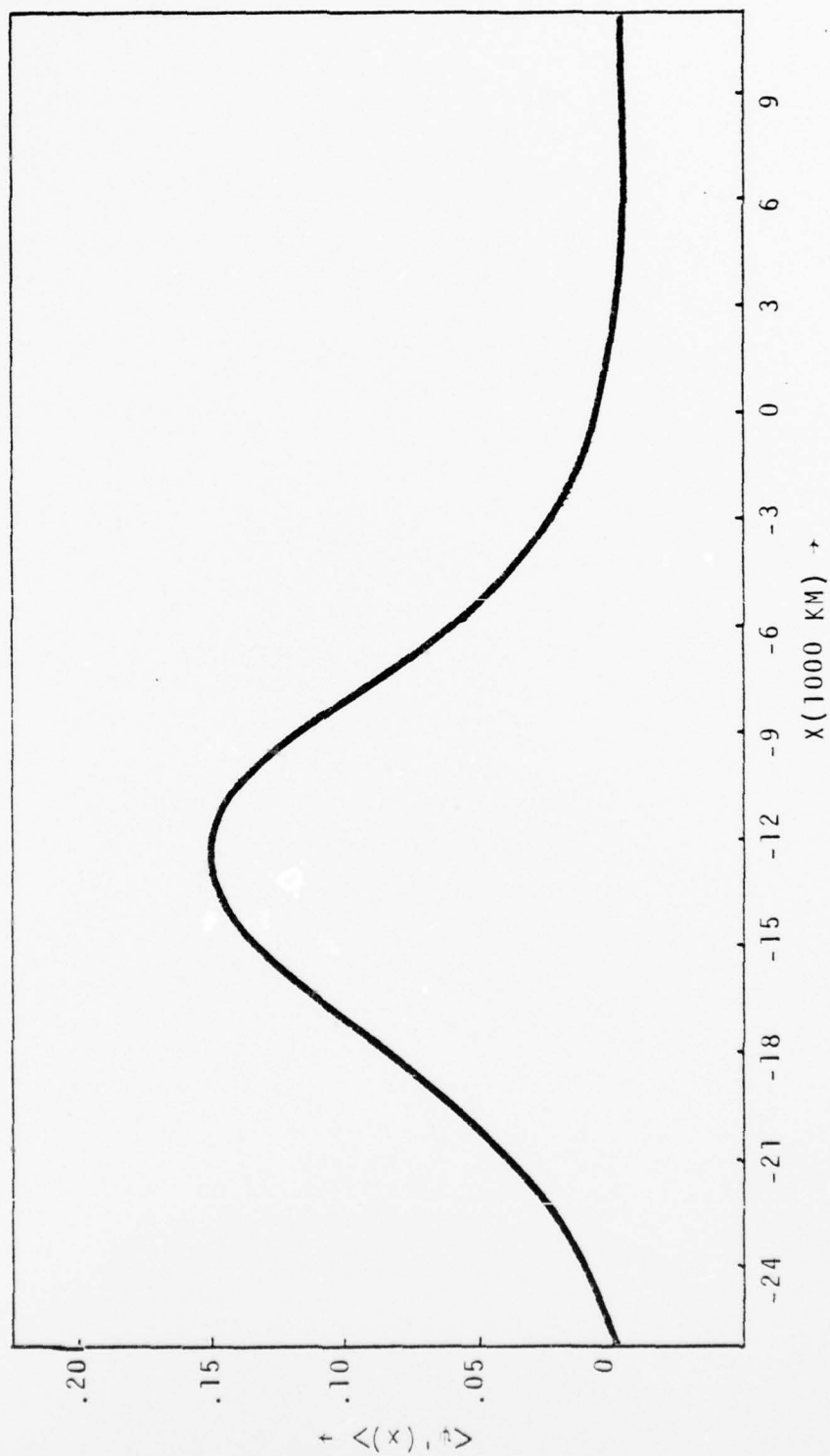
Fig. 27. Experiment II. The wave packet envelope $\langle \psi'(x) \rangle$ from the complete numerical model.
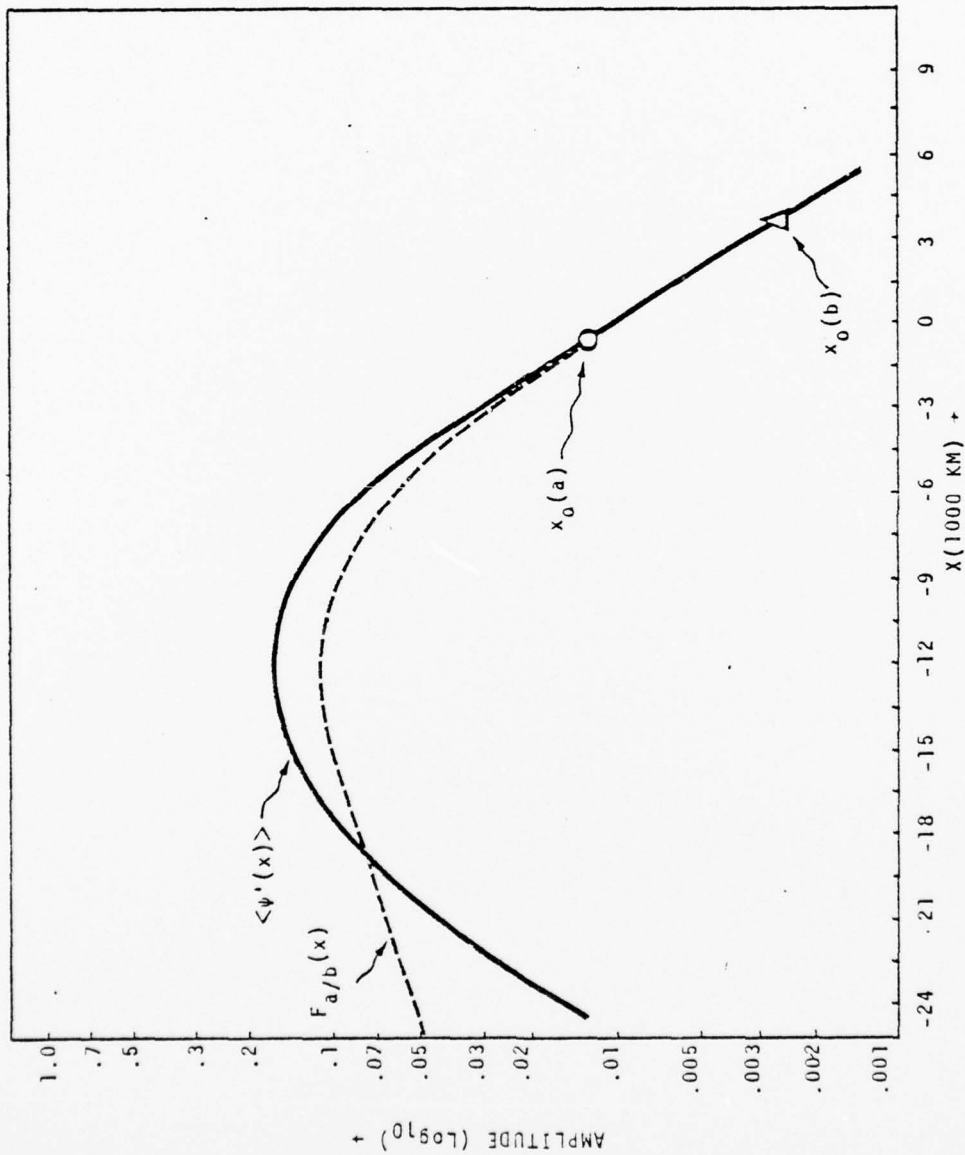
Fig. 28. Experiment II. The wave packet envelopes. $F_a(x)$ is from the analytical model for initial point (a) $x_0{}^a = -375$ km, $F_b(x)$ is from the analytical model for initial point (b) $x_0 = 3750$ km, and $\langle \psi'(x) \rangle$ is from the complete numerical model.

slightly further downstream of the maximum of $m(x=0)$ than in
Experiment I, the cross-over points of the m^* and m curves
exhibit more asymmetry in Experiment II than I. The first
cross-over point occurs approximately at longitude $x = 8500$ km
and $x = 4000$ km for Experiments I and II, respectively, while
the second cross-over point occurs at approximately
$x = -12000$ km where the spatial growth rates vanish. As in
Experiment I, we interpret this asymmetry as being due to the
tilt structure of the waves lagging behind the expected value
from the local stability condition. The fact that this lag
effect is enhanced by the faster phase speed of the waves in
Experiment II can also be seen in Fig. 29 where the north-
south phase tilt $\theta^*(x,y)$ of the wave disturbances for both
experiments are compared at several longitudes. The unstable
tilt in Experiment II is weaker upstream and stronger
downstream of approximately $x = -2000$ km reflecting the
stronger lag effect of the faster moving waves.

Figure 30 compares the phase tilt of the numerical model
solution, θ^*, and that of the most unstable wavelength of
the parallel flow model, θ_0, for two longitudes ($x=0$ and
$x = 3750$ km). Comparing this figure with Fig. 24 of
Experiment I, it is obvious that the apparent augmentation
of the wave tilt due to the zonal variation of $\bar{u}(x,y)$ is now
significantly reduced. This behavior may at least be
partially explained by the lag effect caused by the advective
current U_0, which generally reduces the growth rate in the
vicinity of the jet maximum.

84

Phase Angle θ (Degrees) →
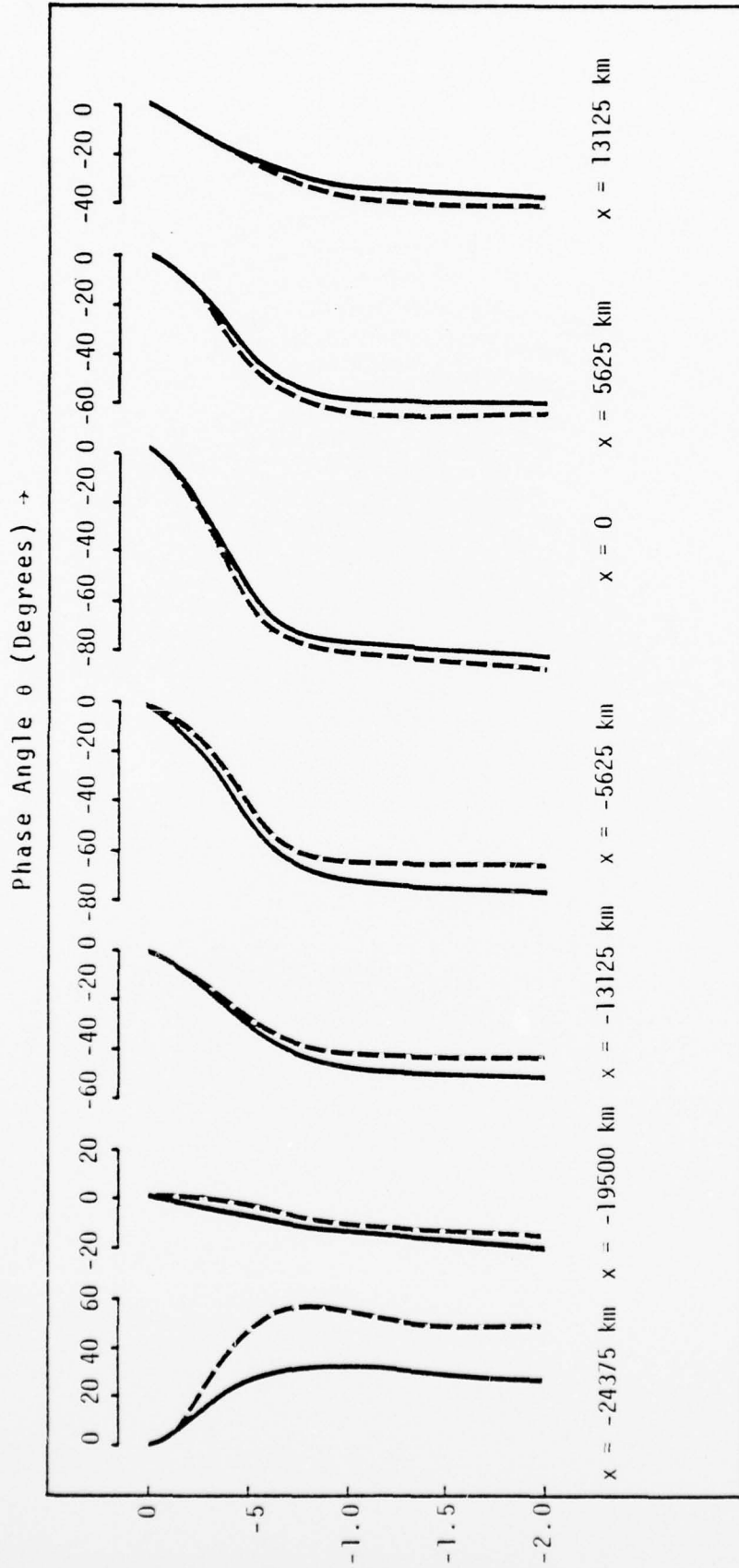
Fig. 29. Comparison of phase tilt of the complete numerical model, $\tilde{\theta}^*$, between Experiment I (dashed) and Experiment II (solid) for longitudes (a) x = 13125 km, (b) x = 5625 km, (c) x = 0, (d) x = -5625 km, (e) x = -13125 km, (f) x = -19500 km, and (g) x = -24375 km.
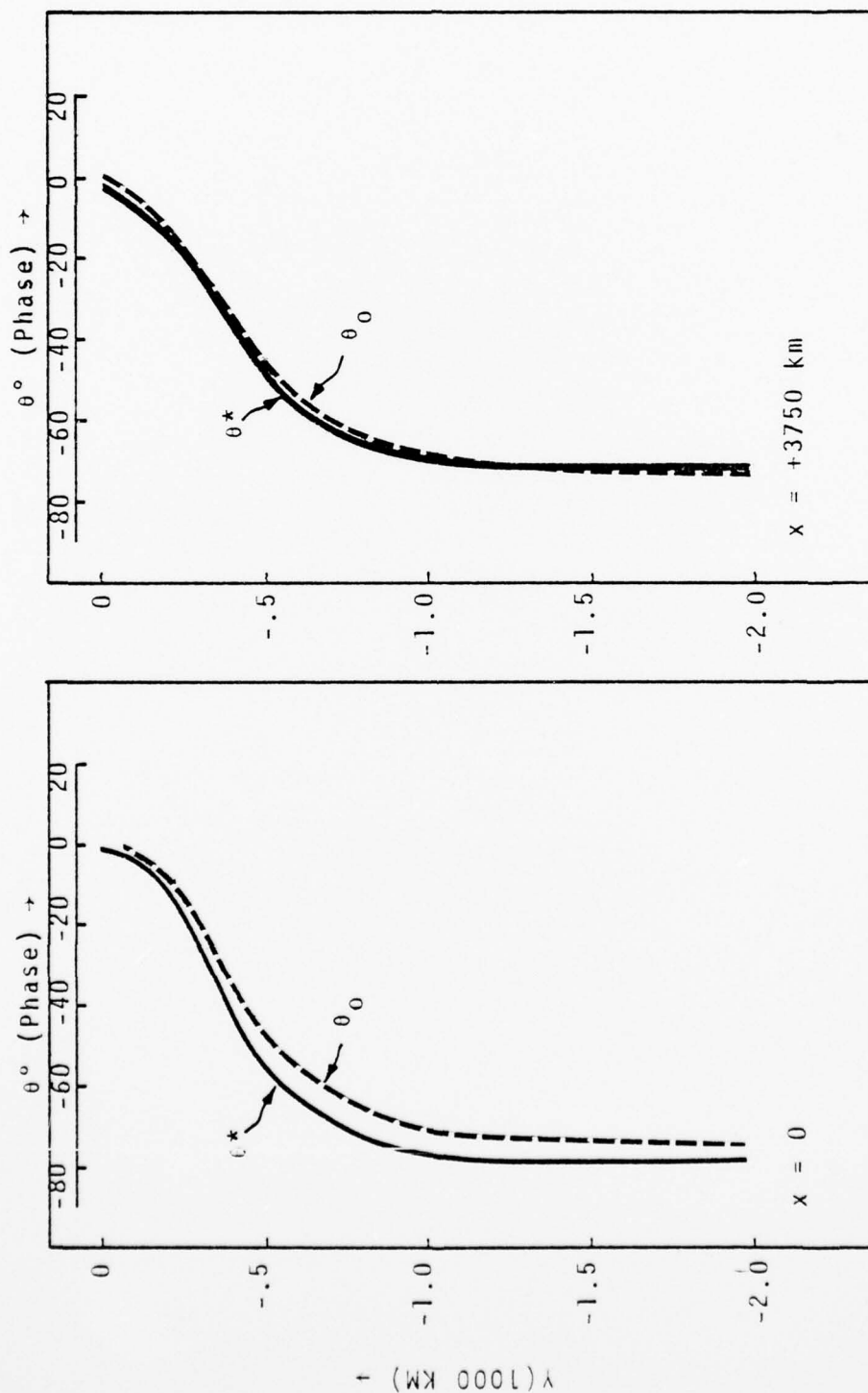
Fig. 30. Experiment II. Comparison of phase tilt of the complete
numerical model, θ^*, and of the most unstable wavelength
of the parallel flow model, θ_0, for longitudes: (a) $x = 0$,
and (b) $x = 3750$ km.

The lower portion of Fig. 31 shows the wavelength measured from the numerical solution at $y = -750$ km. In the upper portion of the diagram are the phase velocities at $y = -750$ km, $c*$ from the complete numerical model and c from the parallel flow model based on the corresponding numerical solution wavelength. The two phase speeds agree very closely upstream of the jet maximum while $c*$ is smaller than c downstream of this longitude. Similarly, Fig. 32 contains the wavelength and phase speeds for latitude $y=0$. At this latitude, the two phase speeds have similar behavior throughout the length of domain with $c*$ being approximately 1 m sec^{-1} slower than c. Figure 33 shows the wavelength curves [$L(x)$] for latitudes $y=0$ and $y = -750$ km. At both latitudes the maximum wavelength occurs near the jet maximum, but the wavelength (and therefore phase velocity) at $y = -750$ km is larger upstream and smaller downstream of approximately $x = -5000$ km. As in Experiment I, these differences in $c*(x)$ and $L(x)$ between the two latitudes are consistent with the observed tilt behavior of the waves.

Other than the foregoing mentioned differences, the basic behavior of the waves in Experiment II is similar to that of Experiment I. This includes the tilt of the waves and its reversal from that of growth to that of damping downstream of $<\psi'>_{max}$, the occurrence of $<\psi'>_{max}$ a considerable distance downstream of the jet maximum, the general shape of the wave packet envelope, and the longitudinal variation of the energy balance (Fig. 34).
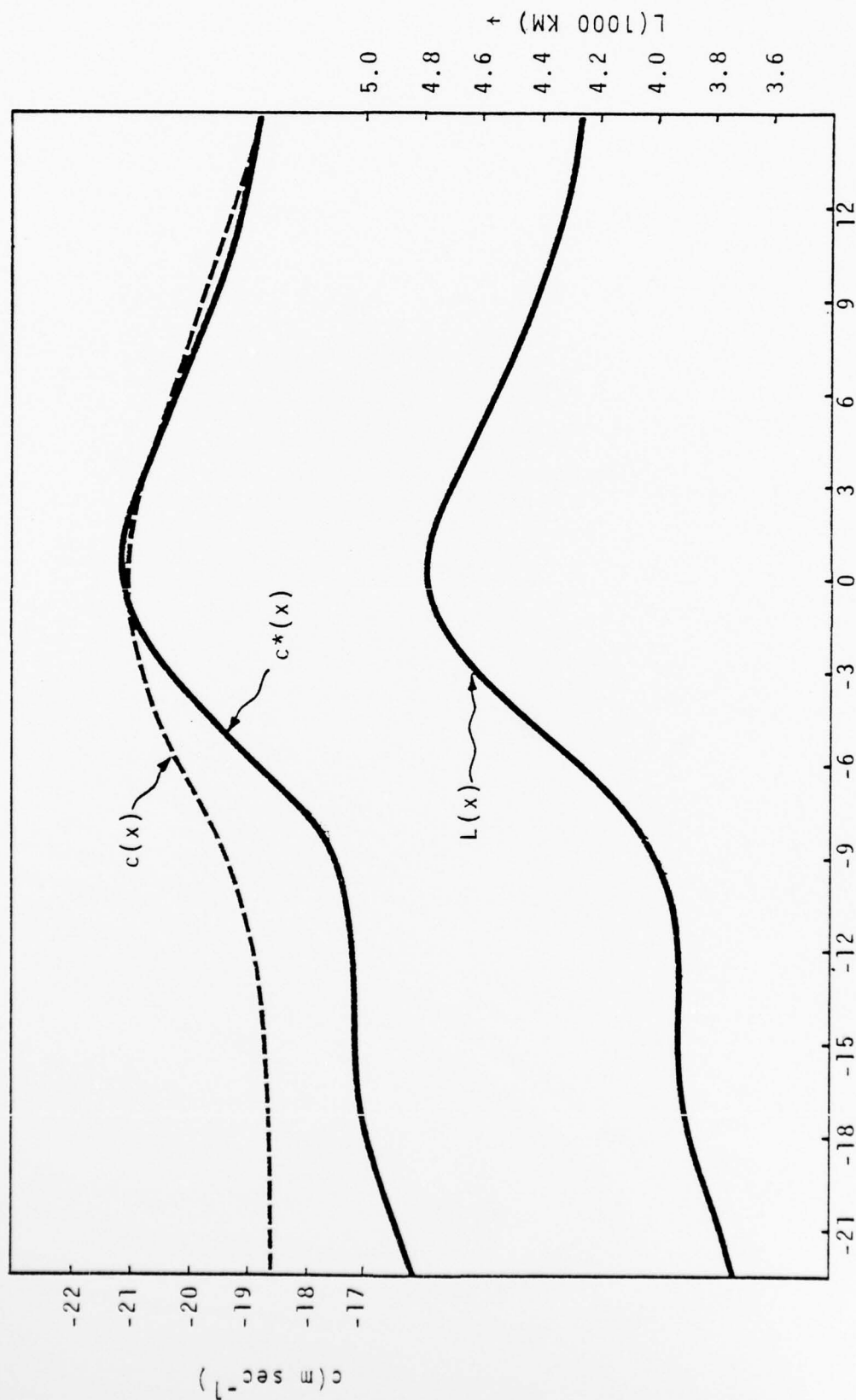
Fig. 31. Experiment II. Latitude y = -750 km. (a) Phase velocities, c(x) from the parallel flow model, and c*(x) from the complete numerical model. (b) Wavelength L(x).
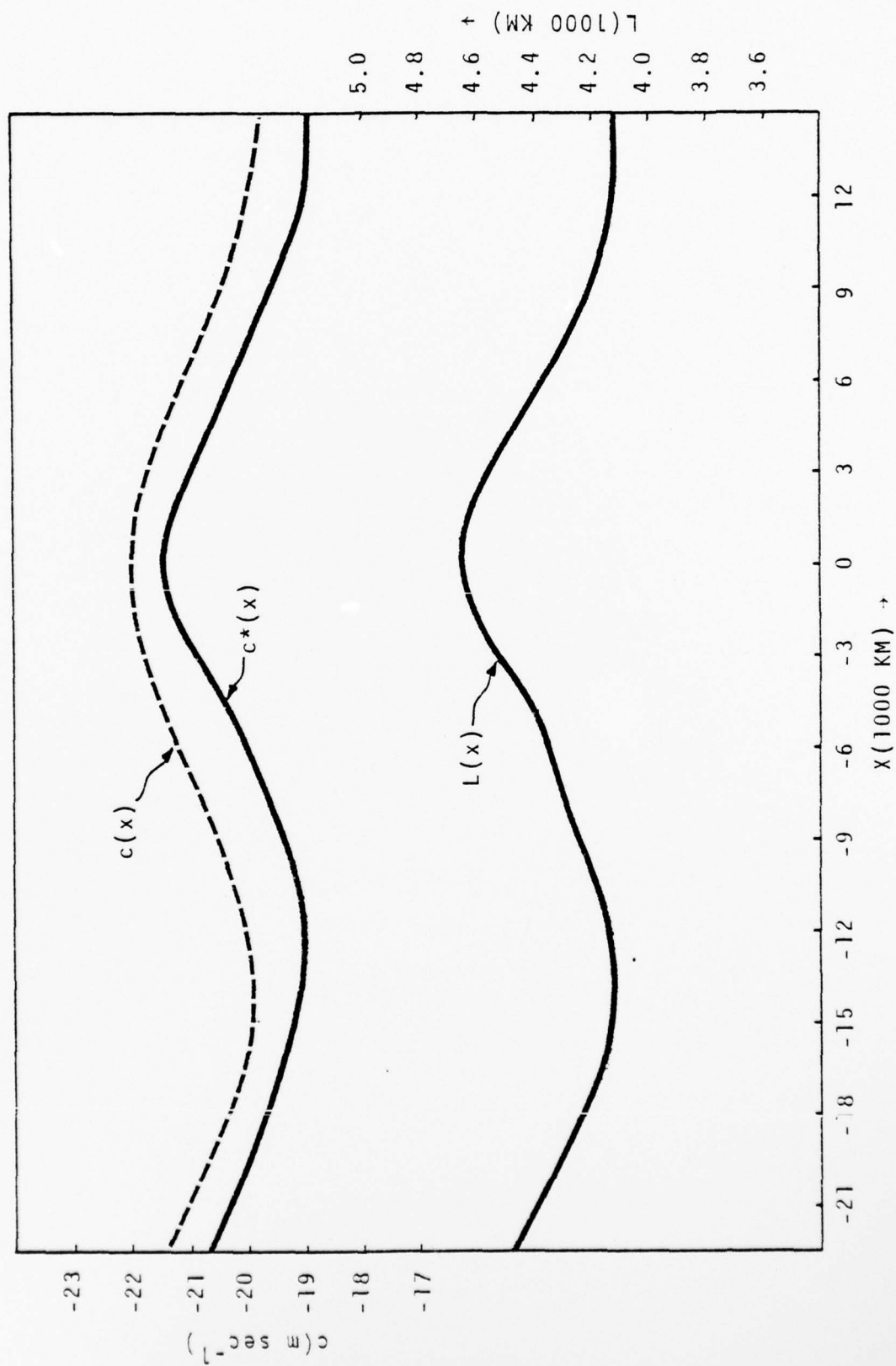
Fig. 32. Experiment II. Latitude y = 0. (a) Phase velocities c(x) from the parallel flow model, and c*(x) from the complete numerical model. (b) Wavelength L(x).
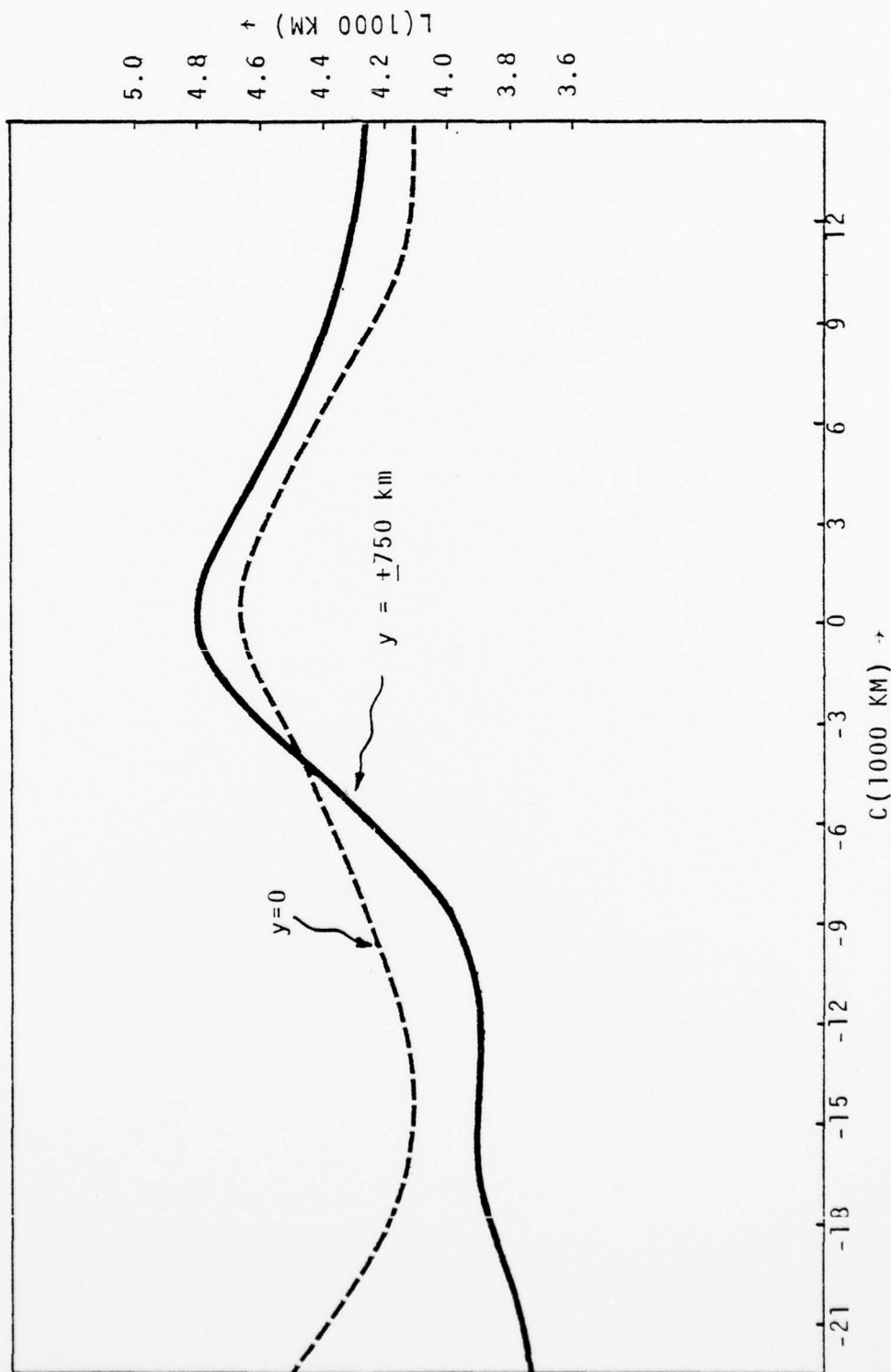
Fig. 33. Experiment II. Wavelength L(x) for latitudes y=0 and y = -750 km.
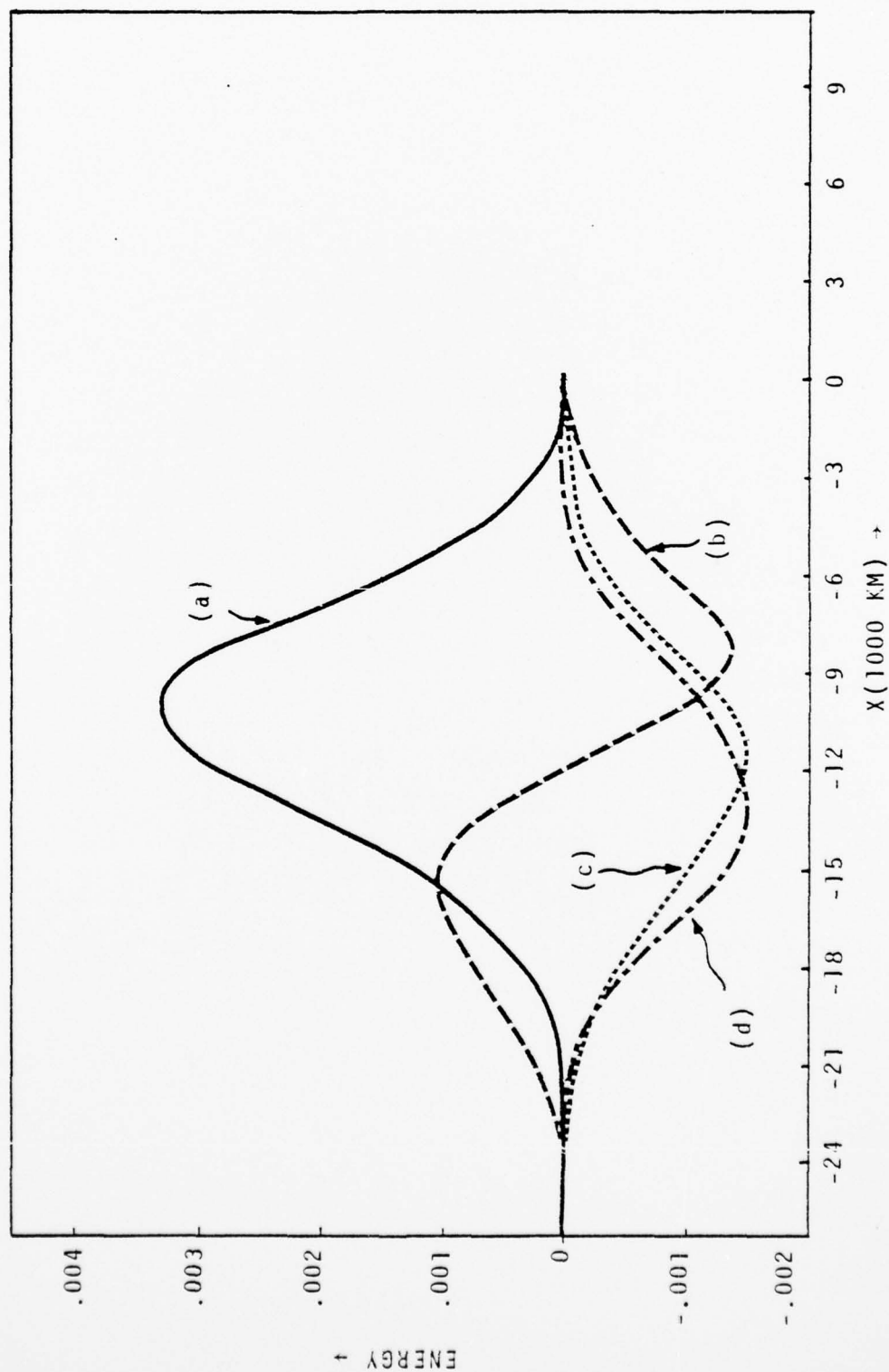
Fig. 34. Experiment II. Disturbance energy balance: (a) Reynold's stress term. $\langle(u'v'\partial\bar{u}/\partial y)\rangle$; (b) energy transport term $\langle(-u\partial k'/\partial x)\rangle$; (c) dissipation term, $\langle(-2D_f k')\rangle$; and (d) pressure work term, $\langle(-\frac{1}{\bar{\rho}}\frac{\partial}{\partial x}(u'p'))\rangle$.

91

VIII. SUMMARY AND CONCLUSIONS

In this work we studied the behavior of waves moving into and out of a barotropically unstable mean wind field which varies both in x and y. This mean wind field roughly simulates the 200 mb easterly jet south of the Tibetan high during the Northern Hemisphere summer. A rectangular domain is used with a time periodic forcing on the inflow (east) boundary and a Sommerfeld radiation condition on the outflow (west) boundary. This allows the simulation of the propagation of small amplitude waves through the easterly jet region. The vorticity equation on a beta plane is solved with the use of finite differences, and, when the boundary conditions are properly adjusted, the barotropic waves move smoothly across the region and out the western boundary. After a certain time period of numerical integration, the solution becomes periodic everywhere with the forcing frequency which is specified on the eastern boundary. As the waves move through the jet regime, they grow or decay spatially in response to the local stability of the mean flow, even though at each point the variation is purely harmonic. The numerical results are compared with a simple mechanistic analytical model which is developed using the local growth rate and phase velocity computed from the parallel flow theory.

Two experiments are carried out in this investigation. The parameters used in these experiments are the same, except that in Experiment II a constant advective velocity of $U_o = - 5$ m sec^{-1} is added to the mean flow in order to gain a better understanding of the adjustment process of a faster moving wave train.

The basic behavior of the waves in both experiments is similar. This includes the following:

1)   The maximum amplitude of the waves occurs a considerable distance downstream from the most unstable part of the jet near where the local growth rate of the parallel flow theory vanishes.

2)   The tilt structure of the waves and its reversal from that of growth to that of damping occurs downstream of the maximum of the wave packet envelope in response to the local stability of the mean flow.

3)   The wavelength (and therefore phase velocity) increases slowly from the inflow boundary to a maximum value near the jet maximum and then decreases slowly downstream reaching a minimum value near the outflow region.

4)   The Reynold's stress term $<(u'v'\partial \bar{u}/\partial y)>$ is the dominant source for disturbance kinetic energy and the advective term $<(-\bar{u}\partial k'/\partial x)>$ plays a significant role in transporting a considerable part of this energy downstream from the source region.

5)   Large spatial damping occurs in the outflow region due to the presence of the continuous spectrum modes.

In Experiment I where the mean wind vanishes toward large y, the maximum spatial growth rate in the numerical model is significantly larger than the spatial growth rate of the parallel flow model. Apparently the downstream variation of the mean wind augments the phase tilt of the waves thus causing an increased growth rate as compared with waves in a parallel flow. In Experiment II where the waves move westward faster due to the presence of a constant $- 5$ m sec^{-1} advective zonal wind, the spatial growth rate computed by the numerical model is brought closer to that given by the parallel flow theory, but the asymmetry of the numerical growth rate curve with respect to the jet maximum is enhanced. The reduction of spatial growth and decay rates is mostly due to the faster phase speed which causes the waves to have less time to grow or damp per unit distance traveled. The enhanced asymmetry is apparently due to a lag effect wherein the adjustment of the waves is delayed spatially. The latter effect is also reflected in the north-south phase structure of the waves and in the smaller variation of the wavelength as the waves propagate downstream. The augmentation of the phase tilt by the downstream variation is also significantly reduced which may at least be partially explained by the lag effect.

Recently Pedlosky (1976) used a simple analytical model to study the effect of the downstream variation of a baro-clinic current. The mean flow in his model changes abruptly

from a weakly unstable regime with a constant growth rate
to a stable regime downstream. His model includes nonlinear
effects but it does not produce strong dynamic damping due
to the continuous spectrum modes. This is perhaps because
he did not include the lateral shear of the mean flow. Thus,
Pedlosky found that his disturbances remain substantially
undiminished when they propagate from a locally unstable
region to a locally stable region.

The behavior of the wave disturbances in our study
resemble certain aspects of the waves observed by
Krishnamurti (1971a, b) along the South Asia easterly jet
during the Northern Hemisphere summer, and the waves that
were simulated by Colton (1973) in a nonlinear model. The
wave disturbances entering upstream of the easterly jet
regime grow and increase their speed and wavelength as they
approach the jet maximum. They then achieve their maximum
amplitude a considerable distance downstream of the jet
maximum and subsequently decay as they leave the strong jet
regime.

The simple mechanistic analytical model developed in
this study can crudely approximate the adjustment of the
moving disturbance to the local stability of a variable mean
flow within the dynamically unstable region. It is possible
that this simple approach could be used to study the linear
instability of other variable mean flows to wave disturbances.

Although this study employs linear equations, it is possible to estimate qualitatively the nonlinear effect of the waves on the mean flow. Since the Reynold's stress term is the dominant term in the energetics, most of the mean kinetic energy is removed by the waves on the downwind side of the jet maximum between where the wave amplitude is maximum and where the phase tilt of the waves is strongest. Clearly these synoptic scale waves will affect the amplitude and phase of the quasi-stationary planetary waves which combine to form the easterly jet over South Asia. These effects can be studied by including nonlinear effects in the present model. It may also be interesting to extend the present model to a 3-dimensional model to study the effect of vertical shear and baroclinicity.

APPENDIX

Subroutine POISDD

Subroutine POISDD is a direct method solver of the finite difference approximation to Poisson's equation (Sweet, 1971):

$$\nabla^2 u(x,y) = - f(x,y) \tag{1}$$

$$\text{for} \quad a < x < b$$

$$c < y < d$$

and with Dirichlet boundary conditions

$$u(x,c) = g_1(x)$$

$$u(x,d) = g_2(x) \qquad a \leq x \leq b \tag{2}$$

$$u(a,y) = g_3(y) \qquad c \leq y \leq b$$

$$u(b,y) = g_4(y)$$

We define a grid on the rectangle $\{(x,y): a \leq x \leq b, c \leq y \leq d\}$ by selecting two positive integers M and N, such that

$$\Delta X = \frac{b-a}{M} \quad \text{and} \quad \Delta Y = \frac{d-c}{N} \tag{3}$$

and where N must be a power of two, and the points

$$x_i = a + (i-1)\Delta x \qquad i=1, 2, \ldots, M+1 \tag{4}$$

$$y_j = c + (j-1)\Delta Y \qquad j=1, 2, \ldots, N+1,$$

where i and j refer to the x and y grid points, respectively.

The Poisson equation that is solved by POISDD is given by Eq. (2.10):

$$\nabla^2 \frac{\partial \psi'}{\partial t} = - J(\bar{\psi}, \nabla^2 \psi') - J(\psi', \nabla^2 \bar{\psi}) - \beta \frac{\partial \psi'}{\partial x} - D_f \nabla^2 \psi' \tag{5}$$

97

with boundary conditions Eqs. (2.11), (2.14) and (2.16). The
finite difference form of these equations are given by Eqs.
(4.10), (4.14) and (4.17). Here $T_{i,j}^{t}$ is the finite differ-
ence representation for the tendency, $\partial \psi'/\partial t$, and is the
dependent variable in our Poisson equation. For our
Numerical Model, M=106 and N=32; t is the current time,
where $t = \ell \Delta t$ $\ell = 1,2....$ and Δt in the time step.

Our system of equations meets the requirements of
subroutine POISDD, except for the outflow boundary condi-
tion, Eq. (2.16).

$$\frac{\partial}{\partial t}\left(\frac{\partial \psi'}{\partial t}\right) = c_{r_o}\frac{\partial}{\partial x}\left(\frac{\partial \psi'}{\partial t}\right) \ . \tag{6}$$

This equation is the Sommerfeld radiation condition (Pearson,
1974). Clearly, this is not the usual form of Dirichlet
boundary condition. Therefore, in order to use POISDD in
our numerical model, this subroutine had to be modified
incorporating the radiation outflow condition. This was
done by writing Eq. (6) in finite difference form:

$$\frac{T_{1,j}^{t} - T_{1,j}^{t-\Delta t}}{\Delta t} = c_{r_o}\frac{T_{2,j}^{t} - T_{1,j}^{t}}{\Delta x} \ , \tag{7}$$

where the finite difference symbols have their usual meaning
in numerical weather prediction. Subscript i=1 refers to
the outflow boundary, and subscript i=2 refers to the
column of grid points next to this boundary. We observe
that this scheme is backward in time with upwind space

differencing. Equation (7) is conveniently rewritten such
that

$$T_{1,j}^{t} = \frac{T_{1,j}^{t-\Delta t}}{1 + c_{r_o} \Delta t / \Delta x} + \frac{T_{2,j}^{t}}{1 + \Delta x / (c_{r_o} \Delta t)} \tag{8}$$

Since all the interior points of the domain must satisfy the
non-homogeneous Poisson equation, we, then, use this constraint
to couple the radiation boundary condition [Eq. (8)] with the
interior points, as follows:

$$\tag{9}$$

$$\frac{T_{3,j}^{t} - 2T_{2,j}^{t} + T_{1,j}^{t}}{\Delta x^2} + \frac{T_{2,j+1}^{t} - 2T_{2,j}^{t} + T_{2,j-1}^{t}}{\Delta y^2} = -f_{2,j}.$$

The term $f_{i,j}$ is the finite difference approximation to the
right side or non-homogeneous part of Eq. (5) or Eq. (2.10).

We multiply Eq. (9) by $-(\Delta y)^2$, and we obtain

$$- \frac{T_{3,j}^{t}}{s} + \frac{2T_{2,j}^{t}}{s} - \frac{T_{1,j}^{t}}{s} - T_{2,j+1}^{t} + 2T_{2,j}^{t} - T_{2,j-1}^{t}$$

$$= f_{2,j} \Delta y^2 \tag{10}$$

where $s \equiv \Delta x^2 / \Delta y^2$.

We now combine Eq. (8) and Eq. (10), and we get

$$- T_{2,j+1}^{t} + \left[2 + \frac{2}{s} - \frac{1}{s\left(1 + \frac{\Delta x}{c_{r_o} \Delta t}\right)} \right] T_{2,j}^{t} - \frac{T_{3,j}^{t}}{s} +$$

$$\tag{11}$$

$$- T_{2,j+1}^{t} = f_{2,j} \Delta y^2 + \frac{T_{1,j}^{t-\Delta t}}{s[1 + c_{r_o} \Delta t / \Delta x]}$$

By incorporating Eq. (11) in subroutine POISDD, we
have, thus, coupled the Sommerfeld radiation boundary condi-
tion to the interior domain. Also, by Eq. (8), we now have
a complete set of Dirichlet boundary conditions. The finite
difference Eqs. (4.10), (4.14) and (4.17), thus, form a
linear system of equations of dimension (M-1) x (N-1) for
the unknowns $T_{i,j}^{t}$: $2\leq i\leq M$, $2\leq j\leq N$. This system is solved in
POISDD by the Buneman variant of the CORF (cyclic odd-even
reduction and factorization) algorithm. Buzbee et al. (1970)
gives a complete mathematical description of the algorithm.
Sweet (1971) gives a brief description of the subroutine.

A function of two variables, $B_{i,j}$, is used in the
numerical model code to represent a two-dimensional array
which provides, on input to POISDD, values of the function
$f_{i,j}$ as well as the specified boundary conditions. On output
from POISDD, it provides the values of the approximation
$T_{i,j}^{t}$. For our numerical model, we approximate the outflow
boundary condition on input to POISDD as follows:

$$B_{1,j}^{*} = \frac{T_{1,j}^{t-\Delta t}}{1+c_{r_o}\Delta t/\Delta x} \quad . \tag{12}$$

On output from POISDD, we correct Eq. (12) by

$$T_{1,j}^{t} = B_{1,j}^{*} + \frac{T_{2,j}^{t}}{1+\Delta x/(c_{r_o}\Delta t)} \quad . \tag{13}$$

BIBLIOGRAPHY

Arakawa, A., 1966: Computational Design for Long-Term Numerical Integrations of the Equations of Atmospheric Motion. Journal of Computational Physics, Vol. 1, 119-143.

Buzbee, B. L., G. H. Golub, and C. W. Nielson, 1970: On Direct Methods for Solving Poisson's Equations. SIAM Journal on Numerical Analysis, Vol. 7, 627-656.

Case, K. M., 1960: Stability of Plane Couette Flow. The Physics of Fluids, Vol. 3, 143-148.

Colton, D. E., 1973: Barotropic Scale Interactions in the Tropical Upper Troposphere During the Northern Summer. Journal of Atmospheric Sciences, Vol. 30, 1287-1302.

Holton, J. R., and D. E. Colton, 1972: A Diagnostic Study of the Vorticity Balance in the Tropics during the Northern Summer. Journal of Atmospheric Sciences, Vol. 29, 1124-1128.

Kanamitsu, J., T. N. Krishnamurti, and C. Depradine, 1972: On Scale Interactions in the Tropics During Northern Summer. Journal of Atmospheric Sciences, Vol. 29, 698-706.

Krishnamurti, T. N., 1971a: Observational Study of the Upper Tropospheric Motion Field during the Northern Hemisphere Summer. Journal of Applied Meteorology, Vol. 10, 1066-1096.

Krishnamurti, T. N., 1971b: Tropical East-West Circulations During the Northern Summer. Journal of Atmospheric Sciences, Vol. 28, 1342-1347.

Kuo, H. L., 1949: Dynamic Instability of Two-Dimensional Non-Divergent Flow in a Barotropic Atmosphere, Journal of Meteorology, Vol. 6, 105-122.

Kuo, H. L., 1951: Dynamical Aspects of the General Circulation and the Stability of Zonal Flow. Tellus, Vol. 3, 268-284.

Kuo, H. L., 1973: Dynamics of Quasi-Geostrophic Flows and Instability Theory. Advances in Applied Mechanics, Vol. 13, 247-330.

Lipps, F. B., 1962: The Barotropic Stability of the Mean Winds in the Atmosphere. Journal of Fluid Mechanics, Vol. 12, 397-407.

Lipps, F. B., 1965: The Stability of an Asymmetric Zonal Current in the Atmosphere. Journal of Fluid Mechanics, Vol. 21, 225-239.

Lipps, F. B., 1970: Barotropic Stability and Tropical Disturbances. Monthly Weather Review, Vol. 98, 122-131.

Lorenz, E. N., 1972: Barotropic Instability of Rossby Wave Motion. Journal of Atmospheric Sciences, Vol. 29, 258-264.

Nitta, T., and M. Yanai, 1969: A Note on the Barotropic Instability of the Tropical Easterly Current. Journal of the Meteorological Society of Japan, Vol. 47, 127-130.

Pearson, R. A., 1974: Consistent Boundary Conditions for Numerical Models of Systems that Admit Dispersive Waves. Journal of Atmospheric Sciences, Vol. 31, 1481-1489.

Pedlosky, J., 1964: An Initial Value Problem in the Theory of Baroclinic Instability. Tellus, Vol. 16, 12-17.

Pedlosky, J., 1976: Finite-Amplitude Baroclinic Disturbances in Downstream Varying Currents. Journal of Physical Oceanography, Vol. 6, 335-344.

Rayleigh, Lord, 1880: On the Stability, or Instability, of Certain Fluid Motions. Scientific Papers, Vol. 1, 474-487.

Rayleigh, Lord, 1913: On the Stability of the Laminar Motion of an Inviscid Fluid. Scientific Papers, Vol. 6, 197-204.

Richtmyer, R. D., 1967: Difference Methods for Initial Value Problems, Interscience Publishers, Inc., New York. 238 pp.

Sweet, R., 1971: Subroutine POISDD, NCAR Computing Facility, Boulder, 5 pp.

Williams, R. T., T. K. Schminke, and R. L. Newman, 1971: Effect of Surface Friction on the Structure of Barotropically Unstable Tropical Disturbances. <u>Monthly Weather Review</u>, Vol. 99, 778-785.

Yamasaki, M., and M. Wada, 1972: Barotropic Instability of an Easterly Zonal Current. <u>Journal of the Meteorological Society of Japan</u>, Vol. 50, 110-120.

Yanai, M., and T. Nitta., 1968: Finite Difference Approximations for the Barotropic Instability Problem. <u>Journal of the Meteorological Society of Japan</u>, Vol. 46, 389-403.

DISTRIBUTION LIST

		No. Copies
1.	Defense Documentation Center Cameron Station Alexandria, VA 22314	2
2.	Library, Code 0142 Naval Postgraduate School Monterey, CA 93940	2
3.	Professor C-P. Chang, Code 63Cj Department of Meteorology Naval Postgraduate School Monterey, CA 93940	6
4.	Professor R. T. Williams, Code 63Wu Department of Meteorology Naval Postgraduate School Monterey, CA 93940	6
5.	CDR J. B. Tupaz Naval Environmental Prediction Research Facility Monterey, CA 93940	6
6.	Professor G. J. Haltiner, Code 63Ha Chairman, Department of Meteorology Naval Postgraduate School Monterey, CA 93940	1
7.	Professor C. Comstock, Code 53Zk Department of Mathematics Naval Postgraduate School Monterey, CA 93940	1
8.	Professor R. L. Elsberry, Code 63Es Department of Meteorology Naval Postgraduate School Monterey, CA 93940	1
9.	Professor F. D. Faulkner, Code 53Fa Department of Mathematics Naval Postgraduate School Monterey, CA 93940	1
10.	Professor T. Houlihan, Code 69Hm Department of Mechanical Engineering Naval Postgraduate School Monterey, CA 93940	1

11. Professor T. Cooper, Code 69Cg   1
     Department of Mechanical Engineering
     Naval Postgraduate School
     Monterey, CA 93940

12. Professor R. L. Haney, Code 63Hy   1
     Department of Meteorology
     Naval Postgraduate School
     Monterey, CA 93940

13. Dr. Robert R. Fossum   1
     Dean of Science and Engineering
     Naval Postgraduate School
     Monterey, CA 93940

14. Commanding Officer   1
     Naval Environmental Prediction
        Research Facility
     Monterey, CA 93940

15. Dr. A. Weinstein   1
     Naval Environmental Prediction
        Research Facility
     Monterey, CA 93940

16. Dr. T. Rosmond   1
     Naval Environmental Prediction
        Research Facility
     Monterey, CA 93940

17. Commanding Officer   1
     Fleet Numerical Weather Central
     Monterey, CA 93940

18. Naval Oceanographic Office   1
     Library, Code 3330
     Washington, DC 20373

19. Meteorology Library, Code 63   1
     Naval Postgraduate School
     Monterey, CA 93940

20. Director, Naval Research Laboratory   1
     ATTN: Technical Services Information Center
     Washington, DC 20390

21. Department of Oceanography, Code 68   1
     Naval Postgraduate School
     Monterey, CA 93940

22. Office of Naval Research   1
    Department of the Navy
    Washington, DC 20360

23. Director   1
    Naval Oceanography and Meteorology
    National Space Technology Laboratories
    Bay St. Louis, MS 39520

24. Dr. A. Arakawa   1
    Department of Meteorology
    University of California
    Los Angeles, CA 90024

25. Dr. F. P. Bretherton   1
    National Center for Atmospheric Research
    P. O. Box 3000
    Boulder, CO 80303

26. Professor J. G. Charney   1
    54-1424
    Massachusetts Institute of Technology
    Cambridge, MA 02139

27. Dr. J. Holton   1
    Department of Atmospheric Sciences
    University of Washington
    Seattle, WA 98105

28. Dr. B. J. Hoskins   1
    Department of Geophysics
    University of Reading
    Reading, United Kingdom

29. Professor T. N. Krishnamurti   1
    Department of Meteorology
    Florida State University
    Tallahassee, FL 32306

30. Dr. E. N. Lorenz   1
    Department of Meteorology
    Massachusetts Institute of Technology
    Cambridge, MA 02139

31. Dr. J. D. Mahlman   1
    Geophysical Fluid Dynamics Laboratory
    Princeton University
    Princeton, NJ 08540

32. Professor T. Murakami   1
     Department of Meteorology
     University of Hawaii
     Honolulu, HI 96822

33. Professor N. A. Phillips   1
     National Meteorological Center/NOAA
     World Weather Building
     Washington, DC 20233

34. Professor J. Pedlosky   1
     Department of Geophysical Sciences
     University of Chicago
     Chicago, IL 60637

35. Professor A. L. Schoenstadt   1
     Code 53Zh
     Naval Postgraduate School
     Monterey, CA 93940

36. Dr. J. Wallace   1
     Department of Atmospheric Sciences
     University of Washington
     Seattle, WA 98195

37. Professor Peter Webster   1
     Department of Atmospheric Sciences
     University of Washington
     Seattle, WA 98195

38. Dr. J. Young   1
     Department of Meteorology
     University of Wisconsin
     Madison, WI 53706